The Astrophysical Journal Supplement Series, 256:45 (34pp), 2021 October https://doi.org/10.3847/1538-4365/ac141c

Breaking the Degeneracy in Magnetic Cataclysmic Variable X-Ray Spectral Modeling Using X-Ray Light Curves

Diogo Belloni[1,2], Claudia V. Rodrigues[1], Matthias R. Schreiber[2,3], Manuel Castro[1], Joaquim E. R. Costa[1], Takayuki Hayashi[4,5], Isabel J. Lima[1], Gerardo J. M. Luna[6,7,8], Murilo Martins[9], Alexandre S. Oliveira[9], Steven G. Parsons[10], Karleyne M. G. Silva[11,12], Paulo E. Stecchini[1,13], Teresa J. Stuchi[14], and Monica Zorotovic[15]
[1] Instituto Nacional de Pesquisas Espaciais, Av. dos Astronautas, 1758, 12227-010, São José dos Campos, SP, Brazil; diogobellonizorzi@gmail.com
[2] Departamento de Física, Universidad Técnica Federico Santa María, Av. España 1680, Valparaíso, Chile
[3] Millenium Nucleus for Planet Formation (NPF), Valparaíso, Chile
[4] NASA Goddard Space Flight Center, Code 662, Greenbelt, MD 20771, USA
[5] University of Maryland, Baltimore County, 1000 Hilltop Circle, Baltimore, MD 21250, USA
[6] CONICET-Universidad de Buenos Aires, Instituto de Astronomía y Física del Espacio (IAFE), Av. Inte. Güiraldes 2620, C1428ZAA, Buenos Aires, Argentina
[7] Universidad de Buenos Aires, Facultad de Ciencias Exactas y Naturales, Buenos Aires, Argentina
[8] Universidad Nacional de Hurlingham, Av. Gdor. Vergara 2222, Villa Tesei, Buenos Aires, Argentina
[9] IP&D, Universidade do Vale do Paraíba, 12244-000, São José dos Campos, SP, Brazil
[10] Department of Physics and Astronomy, University of Sheffield, Sheffield S3 7RH, UK
[11] Gemini Observatory, Casilla 603, La Serena, Chile
[12] European Southern Observatory, Alonso de Cordova 3107, Vitacura, Casilla 19001, Santiago, Chile
[13] IAG, Universidade de São Paulo, Rua do Matão, 1226 São Paulo, SP 05508–900, Brazil
[14] Universidade Federal do Rio de Janeiro, Cidade Universitária, 21941-972, Rio de Janeiro, RJ, Brazil
[15] Instituto de Fśica y Astronomía, Universidad de Valparaíso, Av. Gran Bretaña 1111, 2360102, Valparaíso, Chile
Received 2021 June 5; revised 2021 July 3; accepted 2021 July 12; published 2021 October 11

Abstract

We present an analysis of mock X-ray spectra and light curves of magnetic cataclysmic variables using an upgraded version of the 3D CYCLOPS code. This 3D representation of the accretion flow allows us to properly model total and partial occultation of the postshock region by the white dwarf as well as the modulation of the X-ray light curves due to the phase-dependent extinction of the preshock region. We carried out detailed postshock region modeling in a four-dimensional parameter space by varying the white dwarf mass and magnetic field strength as well as the magnetosphere radius and the specific accretion rate. To calculate the postshock region temperature and density profiles, we assumed equipartition between ions and electrons; took into account the white dwarf gravitational potential, the finite size of the magnetosphere, and a dipole-like magnetic field geometry; and considered cooling by both bremsstrahlung and cyclotron radiative processes. By investigating the impact of the parameters on the resulting X-ray continuum spectra, we show that there is an inevitable degeneracy in the four-dimensional parameter space investigated here, which compromises X-ray continuum spectral fitting strategies and can lead to incorrect parameter estimates. However, the inclusion of X-ray light curves in different energy ranges can break this degeneracy, and it therefore remains, in principle, possible to use X-ray data to derive fundamental parameters of magnetic cataclysmic variables, which represents an essential step toward understanding their formation and evolution.

Unified Astronomy Thesaurus concepts: Cataclysmic variable stars (203); Magnetic variable stars (996)

1. Introduction

Magnetic cataclysmic variables (CVs) are interacting binaries, in which a strongly magnetized white dwarf (WD) accretes matter from a low-mass star (e.g., Warner 1995; Hellier 2001). In magnetic CVs, WD magnetic fields are strong enough to play a role in the dynamics of the accretion flow, and they are generally separated into two main classes, namely intermediate polars (IPs) and polars (see, e.g., Cropper 1990; Patterson 1994; Wickramasinghe & Ferrario 2000; Ferrario et al. 2015, 2020; Mukai 2017, for comprehensive reviews on magnetic CVs).

These two types of CVs differ by the impact the WD magnetic field has on the accretion process. In polars, the WD spin is usually synchronized with the orbital revolution, due to the torque exerted by the donor magnetic field on the WD (e.g., Hameury et al. 1987), and its magnetic field is sufficiently strong such that the magnetic pressure exceeds the gas ram pressure outside the circularization radius, which prevents the formation of an accretion disk. In IPs, on the other hand, given their on average weaker fields, the WD spin is not synchronized with the orbit and a truncated accretion disk is allowed to form because the magnetic pressure exceeds the gas ram pressure at a radius greater than the WD radius but smaller than the circularization radius. Schreiber et al. (2021) proposed a rotation- and crystallization-driven dynamo to be responsible for the generation of WD magnetic fields in CVs. According to this scenario, which successfully explains the observed relative numbers of magnetic WDs in close binaries, the occurrence of strong magnetic fields is intrinsically related to close binary evolution (see also Belloni et al. 2021).

In both polars and IPs, matter is accreted onto the WD in a field-channeled accretion flow, starting at the threading region, which is the region where the magnetic field captures the mass flow from the secondary star, and extending to the WD surface. Such an accretion flow is supersonic when it reaches the region close to the WD surface where a shock is formed. The matter in the postshock region (PSR), which is the region between the shock and the WD surface, is compressed and heated to temperatures up to a few tens of keV and is usually the dominant emission component in magnetic CVs.

Polars are characterized by the strong circular and linear polarization of the optical and near-infrared thermal cyclotron emission. IPs, on the other hand, usually do not exhibit measurable polarization, and the PSR emission at optical wavelengths is diluted by the radiation emitted by the accretion disk. Additionally, due to the high temperature in the PSR, most magnetic CVs are strong X-rays emitters and have been discovered by high-energy surveys.

The X-ray emission in polars and IPs is mostly produced by bremsstrahlung in the PSR. However, there might be contributions from the WD surface and from the preshock region in soft X-rays. For energies greater than ∼10 keV, Compton scattering can also contribute to the observed flux (e.g., Mukai et al. 2015). In addition, line emission provides significant emission at soft X-rays in these systems. At energies smaller than ∼1 keV, X-ray emission from the irradiated/heated WD photosphere has been observed in many systems (e.g., Ramsay & Cropper 2004; Bernardini et al. 2017) and from the photoionized preshock region in EX Hya (Luna et al. 2010).

Among all magnetic CV parameters, four deserve special attention: the WD mass, the WD magnetic field strength, the specific accretion rate, and the threading region radius (the magnetosphere boundary), as they are the main parameters characterizing the emission from the PSR, especially bremsstrahlung (e.g., Wu et al. 1994; Cropper et al. 1998; Wu 2000; Hayashi & Ishida 2014a; Suleimanov et al. 2019). This is because the PSR temperature and density profiles are mainly determined by these four parameters.

Even though the determination of these parameters is generally not straightforward, X-ray emission provides a tool to estimate them in a relatively simple way (e.g., Cropper et al. 1998, 1999; Ramsay 2000; Suleimanov et al. 2005, 2016, 2019; Yuasa et al. 2010; Hayashi & Ishida 2014b). Inspired by the early works of Aizu (1973) and Hōshi (1973), modeling of the X-ray emission from the PSR has been improved by several groups with the aim to derive strong constraints on crucial parameters of magnetic CVs. These models take into account the influence of cyclotron emission (e.g., Wu et al. 1994), the WD gravity (e.g., Cropper et al. 1999), dipole geometry of the WD magnetic field (e.g., Canalle et al. 2005), and the difference between the electron and ion temperatures (e.g., Imamura et al. 1987; Saxton et al. 2007).

In particular, Hayashi & Ishida (2014a) investigated the influence of the specific accretion rate and the WD mass on predicted PSR and X-ray spectrum properties by considering a dipole-like geometry. However, these authors did not take into account the effects of cyclotron emission in their analysis. That said, it is still not clear how their results would change in the presence of strong cyclotron emission, which is the case for polars and some IPs (e.g., V405 Aur, PG Gem, and V2400 Oph). In order to address this issue, we thoroughly analyze here PSR properties by varying four parameters, namely the WD mass, the WD magnetic field, the magnetosphere/threading region radius, and the specific accretion rate. To do so, we upgraded the 3D CYCLOPS code (Costa & Rodrigues 2009; Silva et al. 2013) such that the PSR is consistently built based on the model parameters. An example of fitting with this new version of the code has been recently performed by Oliveira et al. (2019), who investigated the polar V348 Pav in optical wavelengths. In addition, we analyze the properties of the X-ray spectra resulting from the PSR modeling and discuss how model parameters affect them.

Despite the fact that X-ray emission modeling became a quite convenient technique to estimate magnetic CV parameters, there is one major difficulty with this approach, namely the degeneracy problem. Within a fitting scheme, many combinations of the parameters naturally lead to virtually identical X-ray spectra, despite the PSRs being substantially different. This implies that fitting X-ray continuum spectra alone does not necessarily provide unambiguous estimates for magnetic CV parameters, even in simplified schemes.

In previous works, several assumptions had to be made to break the degeneracy in the complex parameter space of magnetic CVs. Yuasa et al. (2010) used an improved version of the approach of Suleimanov et al. (2005), who assumed cyclotron emission to be negligible and the magnetosphere to be infinite. A similar approach was used more recently by Hayashi & Ishida (2014a). In both cases, the additional assumptions reduce the parameter space, leaving only the WD mass and the specific accretion rate to be fitted.

Even though Yuasa et al. (2010) broke the degeneracy by assuming a constant specific accretion rate of 1 g s^{-1} cm^{-2}, in a more general situation of unknown specific accretion rate, both Yuasa et al. (2010) and Hayashi & Ishida (2014a) would still have problems with the degeneracy of the WD mass and the specific accretion rate. For instance, Hayashi & Ishida (2014b) applied their model to investigate the IPs EX Hya and V1223 Sgr and found a strong degeneracy in the plane of these two parameters. These authors managed to estimate both parameters for EX Hya with their method but needed additional constraints, related to the PSR height, in order to properly estimate the properties of V1223 Sgr. This is not a desirable solution to the degeneracy problem, though, because detailed information, which provides such additional "external" constraints, is not usually available for most magnetic CVs.

The last example we discuss is the approach by Suleimanov et al. (2016, 2019). In addition to assuming negligible cyclotron emission, in their short-column method, they fixed the accretion rate and the fraction of the WD surface occupied by the PSR and calculated the specific accretion rate for a given WD mass and radius. On the other hand, their tall-column method consists of fixing the PSR height, so that the specific accretion rate in the fitting scheme is simply adjusted to match the desired height for a given combination of magnetosphere radius and WD mass. In their model, the WD mass and the magnetosphere radius are the free parameters, which turned out to be degenerate. Therefore, should only X-ray spectra be used in their fitting scheme, the degeneracy would still remain, even in a 2D parameter space.

In order to break this degeneracy, these authors added information about the break frequency in the power spectra of X-ray light curves, which corresponds to the Keplerian frequency at the magnetospheric boundary. By doing so, these authors managed to infer the magnetosphere radius together with the WD mass. Despite the fact that this method seems to work, it is usually not possible to extract the break frequency from observations (e.g., Shaw et al. 2020). More importantly, it does not solve the degeneracy problem in a four-dimensional fitting scheme, as investigated here. Thus, a new method is required to break the degeneracy without oversimplifying the problem.

A popular tool to fit X-ray spectra is XSPEC (Arnaud 1996; Dorman & Arnaud 2001). The basic XSPEC recipe consists of a combination of additive and multiplicative models. In the

context of magnetic CVs, the PSR emission should be represented by an additive model while the absorption is a multiplicative model. Examples of additive models are BREMSS, which represents the thermal bremsstrahlung emission of a hot gas at a given temperature; MEKAL, which adds line emission to the continuum bremsstrahlung of a hot gas at a given temperature; APEC, which provides an emission spectrum from collisionally ionized diffuse gas calculated from the AtomDB atomic database; and MKCFLOW, which is a cooling flow model, in which a multitemperature hot gas emits following the MEKAL recipe for each temperature. In addition, the IPOLAR model, which can be loaded as a table model, represents the X-ray emission (3–200 keV) from PSRs obtained from a grid following Suleimanov et al. (2016).

The PSR emission can be modified by the photoelectric absorption coming from two astrophysical origins: (i) the interstellar gas between the magnetic CV and the Earth and (ii) the material in the binary. The interstellar absorption is well represented by the PHABS multiplicative model of XSPEC. The modulation of the flux with respect to the WD rotation seen in many systems indicates the presence of absorbing material in the magnetic accretion column above the PSR (i.e., in the preshock region), which affects the PSR emission differently with the rotation phase. To account for the effect of this variable absorption in the spectrum, the partial covering fraction absorption model (PCFABS) of XSPEC is usually adopted. It basically assumes that only a fraction of the additive model is absorbed. That approach allows a quick and easy fitting of X-ray spectra of magnetic CVs. However, it does not necessarily represent a consistent view of the system. As we show later in this paper, a 3D representation of the entire magnetic accretion structure, PSR and preshock region, is required for a correct modeling of the observed X-ray emission of magnetic CVs.

In this paper, we address the degeneracy of the X-ray continuum spectral modeling of magnetic CVs using four parameters: WD mass, WD magnetic field, specific accretion rate, and magnetosphere radius. In addition to investigating in detail this degeneracy problem, we also discuss additional observational constraints that could be incorporated in magnetic CV fitting strategies thereby allowing to break the degeneracy. More specifically, we show how X-ray light curves allow models with similar X-ray spectra to be disentangled. We will present applications of this new approach proposed in this work to observations in forthcoming papers.

2. CYCLOPS Code

The CYCLOPS code developed by Costa & Rodrigues (2009) and improved by Silva et al. (2013) is a tool that enables modeling of cyclotron and bremsstrahlung emissions, in optical and X-rays, from PSRs in magnetic CVs.

In the CYCLOPS code, a 3D grid is used to represent the entire magnetic CV accretion structure, which is defined by the lines of a dipolar magnetic field, from the threading region to the WD surface. For a given rotational phase, the accretion structure is represented by cells in a 3D Cartesian grid having one axis parallel to the line of sight. Despite the fact that the linear dimension of a cell in the plane of sky can assume any value, we enforce the cell dimension in the line of sight to have at least 0.1 of the minimum geometrical depth considering all rotation phases. This allows us to properly sample the PSR density and temperature profiles. Even though CYCLOPS can account for PSRs in either only one hemisphere or both hemispheres simultaneously, we consider in this paper only one PSR per system.

2.1. Radiative Transfer in the Postshock Region

The radiative coefficients are calculated for each cell of the PSR according to its physical properties. The magnetic field magnitude and direction follow a dipolar magnetic field parameterized by its axis direction and magnitude at the magnetic pole. In the optical regime, the cyclotron emissivities of the four Stokes parameters are calculated according to the WD magnetic field and plasma density and temperature. CYCLOPS adopts the radiative transport solution of Pacholczyk & Swihart (1975) and Meggitt & Wickramasinghe (1982). The free–free absorption is also considered in the transport. In X-rays, the bremsstrahlung emissivity is computed by assuming a fully ionized magnetized hydrogen plasma, following Gronenschild & Mewe (1978) and Mewe et al. (1986).

The radiative transfer in the PSR is computed, from the bottom to the top of the region, along the line of sight. So, the PSR emission is represented by a 2D array of fluxes, each flux being the result of the radiative transfer in one line of sight. Therefore, the outcome is an image in each rotation phase for each Stokes parameter, which is integrated to obtain fluxes and polarization as a function of the rotation phase. An X-ray spectrum is calculated by combining the fluxes in all rotation phases. Routines from the PINTofALE package (Kashyap & Drake 2000) are used to convolve the model with the X-ray instrumental files ,allowing us to compare the models with high-energy observations.

2.2. Interstellar and Preshock Region Extinction

CYCLOPS takes into account two sources of extinction, namely the interstellar medium and the preshock region. In X-rays, Compton scattering by electrons and photoelectric absorption are considered. The Compton scattering cross section is calculated using the Klein–Nishina formula (e.g., Rybicki & Lightman 1986). The photoelectric cross section is calculated using the BAMABS routine from the PINTofALE package, an implementation for cross-sections presented by Balucinska-Church & McCammon (1992). This calculation has an upper energy limit of 10 keV, above which no photoelectric absorption is considered. Only photoelectric absorption is taken into account for the interstellar extinction, as this material is considered neutral. However, because we assume that the preshock material is partially ionized, both Compton scattering and photoelectric absorption are included in its extinction. In optical wavelengths, Thomson scattering in the preshock column scatters the PSR emission out of the line of sight. The reddening of the interstellar medium is calculated using the gas-to-dust ratio of Zhu et al. (2017), $R = 3.1$, and the extinction law from Cardelli et al. (1989).

Each line of sight that composes the emission of the PSR crosses a given number of cells of the preshock region. This allows us to calculate the preshock length in each line of sight and consequently its optical depth. For simplicity, and in the absence of a proper model for the preshock properties, the density is assumed constant and equals the density in the shock front multiplied by a factor that can assume values from 0 to 0.25. This maximum limit comes from the Rankine–Hugoniot conditions in the shock front (Equations (A13) and (A14)). We

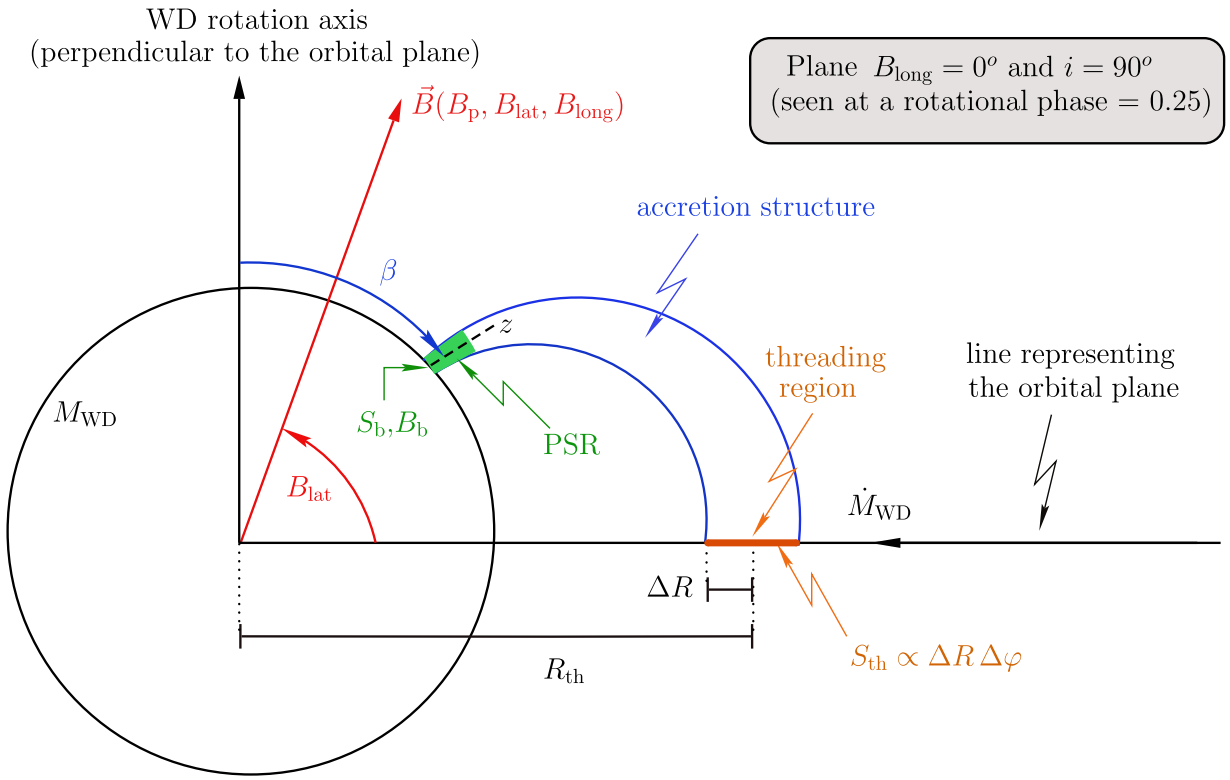

Figure 1. Geometrical aspects in the CYCLOPS code. The WD is assumed to be an opaque sphere with mass $M_{\rm WD}$, which accretes matter at a rate $\dot{M}_{\rm WD}$. The WD rotation axis (vertical axis) is assumed to be parallel to the donor rotation axis and both are orthogonal to the orbital plane (horizontal axis). The magnetic field is assumed to be a centered dipolar field with a given intensity at the pole ($B_{\rm p}$) and the magnetic axis is defined by a latitude ($B_{\rm lat}$, from the orbital plane) and a longitude ($B_{\rm long}$, from the line connecting the WD and the donor, and having a counterclockwise direction with respect to the WD rotation axis). Notice that the system can have any inclination i, which is defined by the angle between the WD rotation axis and the observer. However, in the figure, we show the case in which $i = 90°$ and $B_{\rm long} = 0°$, for simplicity, for a system seen at a rotation phase of 0.25. After the magnetic axis is set in the code, the colatitude of the PSR (β) has to be set, which is the angle between the WD rotation axis and the PSR center. By providing $B_{\rm p}$, $B_{\rm lat}$, $M_{\rm WD}$, and $\dot{M}_{\rm WD}$, the threading region position ($R_{\rm th}$) in the orbital plane is directly set, which is the position at which the magnetic field captures the material from the donor. In order to define the size of the PSR, the threading region area ($S_{\rm th}$) needs to be defined. This is done by means of a radial extension (ΔR) and an angular extension ($\Delta\varphi$). Having constructed the threading region, the entire accretion column is built, from the threading region to the WD surface. In this way, the accretion area on the WD surface, i.e., at the PSR bottom, ($S_{\rm b}$) is directly provided, and the magnetic field strength at the PSR bottom ($B_{\rm b}$) also comes from the adopted geometry. See Costa & Rodrigues (2009) for more details.

arbitrarily assume that the preshock region is partially ionized, with a fraction of 0.5 of the mass ionized.

2.3. Model Parameters

In order to have a model in the CYCLOPS code, some geometrical properties need to be specified. They are the inclination of the magnetic CV orbital plane with respect to the observer (i), the angular position of the PSR center with respect to the WD rotation axis (β), the radial (ΔR) and the angular ($\Delta\varphi$) sizes of the threading region, and the dipolar magnetic field parameters, i.e., its intensity at the pole ($B_{\rm p}$), its latitude ($B_{\rm lat}$) with respect to the orbital plane, and its longitude ($B_{\rm long}$) with respect to the line connecting the WD and the donor star.

In addition to the abovementioned parameters, two other physical parameters have to be set, namely the WD mass ($M_{\rm WD}$) and the accretion rate ($\dot{M}_{\rm WD}$). Moreover, the distance to the investigated source can be included as a fixed parameter, in case it is known (e.g., from Gaia accurate parallaxes). Finally, an important quantity, which is not a parameter in the code, is the specific accretion rate at the PSR bottom ($\dot{m}_{\rm b}$) defined as $\dot{M}_{\rm WD}/S_{\rm b}$, where $S_{\rm b}$ is the accretion area on the WD surface. The geometry adopted in the CYCLOPS code, as well as its parameters, is illustrated in Figure 1 (see also Figure 1 in Costa & Rodrigues 2009).

2.4. Postshock Region Modeling

In previous versions of the CYCLOPS code, the adopted PSR electronic density and temperature profiles were represented by simple fixed analytic expressions (Silva et al. 2013, their Equations (1) and (2)), which did not depend on the physical parameters of the system and, in addition, did not consistently relate to one other. We upgraded here the modeling of the PSR structure, which is now obtained from the solution of the stationary one-dimensional hydrothermodynamic differential equations describing the accreting plasma. In what follows we briefly discuss the major changes, and a detailed description of our PSR modeling, as well as comparisons with previous works, is provided in Appendices A and B.

In our modeling, we consider the WD gravitational potential (e.g., Cropper et al. 1999) and assume equipartition between ions and electrons (e.g., Wu et al. 1994; Van Box Som et al. 2018). Additionally, we adopt a dipole-like magnetic field geometry (i.e., cubic cross-section variation; e.g., Hayashi & Ishida 2014a; Suleimanov et al. 2016), allow the WD magnetic field to decay as the distance from the WD surface increases (e.g., Canalle et al. 2005; Saxton et al. 2007), and take into account the fact that the threading region is not at infinite (e.g., Suleimanov et al. 2016). Moreover, we assume that brems-strahlung and cyclotron radiative processes are the dominant mechanisms responsible for the cooling of the gas, from the

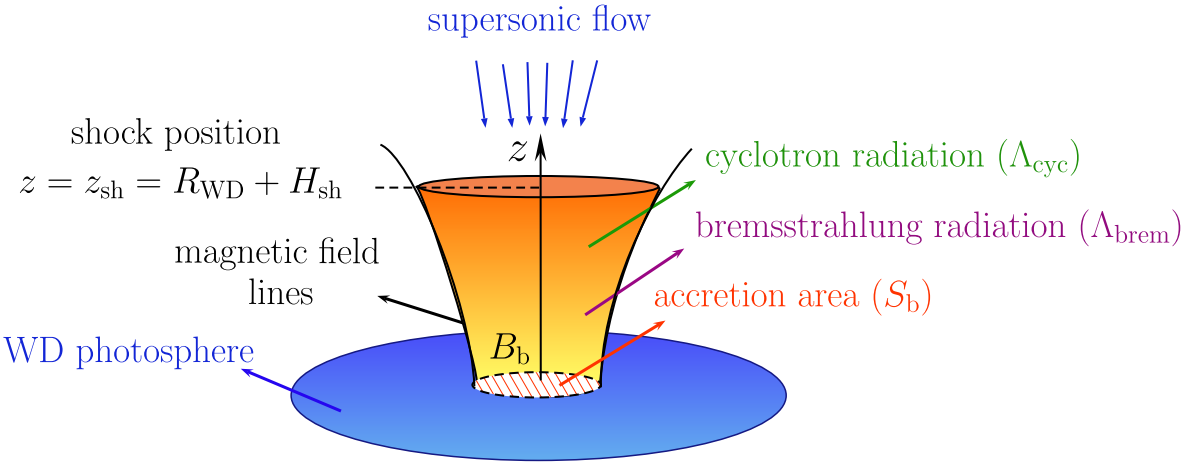

Figure 2. Geometry of the PSR assumed here. Both cyclotron cooling ($\Lambda_{\rm cyc}$) and bremsstrahlung cooling ($\Lambda_{\rm brem}$) are considered in our modeling. The region is defined by the accretion area ($S_{\rm b}$) and the magnetic field strength ($B_{\rm b}$), both at the PSR bottom. The spatial coordinate z is perpendicular to the WD surface and its starting point is the WD center. In this way, the shock position is $z_{\rm sh} = R_{\rm WD} + H_{\rm sh}$, where $H_{\rm sh}$ is the shock height with respect to the WD surface. Both cross section $S(z)$ and magnetic field $B(z)$ vary through the PSR in the z-direction.

shock to the WD surface (Canalle et al. 2005; Van Box Som et al. 2018).

We illustrate the geometrical and physical aspects of our PSR model in Figure 2. The spatial coordinate z defining the PSR is perpendicular to the WD surface and has its origin in the WD center, which implies that the shock position is $z_{\rm sh} = R_{\rm WD} + H_{\rm sh}$, where $H_{\rm sh}$ is the shock height with respect to the WD surface. The PSR cross-section increases and the magnetic field strength decreases as z increases, which causes variations in the cooling efficiency.

2.5. General Remarks on the CYCLOPS Code

Before proceeding further, a few comments are worth making. First, the current version of the CYCLOPS code substantially differs from previous versions. In the first version of the code (Costa & Rodrigues 2009), only cyclotron emission could be modeled, which means that only optical light curves could be used as constraints in any fitting strategy. In the second version of the code (Silva et al. 2013), bremsstrahlung emission was included, which allowed us to also model X-ray spectra. However, in both versions, the PSR temperature and density profiles were not consistently obtained from the physical parameters of the model because simple analytical expressions had been used to calculate them (Silva et al. 2013, their Equations (1) and (2)). In the version we present here, in addition to including X-ray light curves, the PSR properties are consistently obtained from the physical parameters of the system, through the solution of the hydrothermodynamic equations describing the accreting plasma, as described in detail in Appendix A.

Second, the CYCLOPS code defines the whole accretion structure from the threading region to the bottom of the PSR region at the WD surface. That said, the accretion area at the bottom of the PSR ($S_{\rm b}$) comes directly from the adopted magnetic field geometry and the threading region area $S_{\rm th} \propto \Delta R \Delta\varphi$.

Third, in Figure 1, we illustrate the particular case in which $B_{\rm long} = 0°$. In such a situation, the central line of the accretion structure is in the plane formed by the WD axis and the line connecting the WD center and the threading region center. Consequently, the PSR footprint on the WD surface forms into an arc "parallel" to the WD latitude circles. However, if $B_{\rm long} > 0°$, then the central line of the accretion structure is bent to this plane, and the PSR arc is no longer "parallel" to WD latitude circles.

Fourth, we shall emphasize that unlike other codes (e.g., Fischer & Beuermann 2001; Canalle et al. 2005; Saxton et al. 2007; Yuasa et al. 2010; Hayashi & Ishida 2014a; Suleimanov et al. 2019), CYCLOPS is a 3D code, which allows us to properly model optical polarization and light curves as well as X-ray spectra and light curves using the same tool. In addition, because the WD is treated as a 3D body in the code, CYCLOPS is able to also model the so-called self-eclipse of the PSR by the WD. In other words, the code takes into account the partial or total occultation of the PSR by the WD, which might occur depending on the geometry of the system, producing a variation in the observed flux as a function of the WD rotation phase.

Fifth, the preshock accretion structure is also represented as a 3D structure in CYCLOPS, which works as a partial covering absorber. Its absorption of the PSR emission is included in the radiative transport and allows us to consistently calculate the variation of the X-ray emission along the WD rotation and its effect on X-ray light curves and spectra. All of this makes CYCLOPS a powerful tool to understand magnetic accretion in CVs. In particular, the consistent geometrical approach of the PSR and preshock region allows us to model light curves in an unprecedented way.

Sixth, the properties of the PSR are calculated considering a 1D approach, similarly to what is done in most previous studies. In particular, the magnetic field values are those of the central line of the PSR. On the other hand, the radiative transfer is performed in a 3D approach. As a compromise, we assume that the density and temperature radial profiles are the same along the entire PSR and given by the 1D PSR modeling.

Seventh, CYCLOPS X-ray spectra are in very good agreement with those generated by the XSPEC code, which is a widely used X-ray package to fit X-ray spectra. A detailed comparison between both codes, for several cases of uniform PSR distributions, is provided in Appendix C.

Finally, despite the fact that the CYCLOPS code can handle data in virtually any frequency range, including optical polarized emission, we focus in this paper on X-ray data.

Table 1
Parameters of the Standard Model Discussed in this Paper

i (°)	$B_{\rm long}$ (°)	β (°)	$M_{\rm WD}$ ($M_\odot$)	$B_{\rm p}$ (MG)	$\dot{m}_{\rm b}$ (g s^{-1} cm^{-2})	$R_{\rm th}$ ($R_{\rm WD}$)
90	0	5	0.8	1	1	130

Note. The nondefined parameters (i.e., $B_{\rm lat}$, $\dot{M}_{\rm WD}$, $\Delta\varphi$, and ΔR) are set such that $R_{\rm th} = 130\,R_{\rm WD}$ and $\dot{m}_{\rm b} = 1$ g s^{-1} cm^{-2}. In addition, we assume that the source is at a distance of 100 pc. See Section 2 for details about these parameters.

However, a discussion on how one could break the degeneracy using optical light and polarization curves is planned to be held elsewhere.

3. PSR Structure

From now on, we will address properties of PSRs as well as magnetic CV X-ray spectra and light curves. A detailed description of our modeling, including the physical/geometrical assumptions, the hydrothermodynamic differential equations, and the numerical method to solve them, as well as comparisons with other works, can be found in Appendices A and B. For simplicity, we define a standard model, which will be widely used hereafter, as follows. The standard model has the geometry illustrated in Figure 1, i.e., $B_{\rm long} = 0°$ and $i = 90°$. In addition, we set $\beta = 5°$, $M_{\rm WD} = 0.8\,M_\odot$, and $B_{\rm p} = 1$ MG. We further set $B_{\rm lat}$ such that $R_{\rm th} = 130\,R_{\rm WD}$. Moreover, we assume that the standard model corresponds to a source at a distance of 100 pc. Finally, we set $\dot{M}_{\rm WD}$, $\Delta\varphi$, and ΔR, such that $\dot{m}_{\rm b} = 1$ g s^{-1} cm^2. The properties of the standard model are summarized in Table 1.

3.1. Dependence on Main Parameters

In order to illustrate how the PSR profiles are affected by the CYCLOPS input parameters, we show in Figures 3 and 4 temperature profiles built with different values of $B_{\rm p}$, $M_{\rm WD}$, $\dot{m}_{\rm b}$, and $R_{\rm th}$. For simplicity, the remaining parameters are set as in the standard model (Table 1). We fixed $B_{\rm p}$ in each figure, i.e., 1 MG in Figure 3 and 30 MG in Figure 4, and $M_{\rm WD}$ in each row, i.e., $0.6\,M_\odot$ (top rows) and $1.0\,M_\odot$ (bottom rows). With respect to $\dot{m}_{\rm b}$, we set three values in each figure, namely 0.1 g s^{-1} cm^{-2} (left panels), 1 g s^{-1} cm^{-2} (middle panels), and 10 g s^{-1} cm^{-2} (right panels). Finally, the values used for $R_{\rm th}$ are indicated by the color bars. The four parameters analyzed here ($B_{\rm p}$, $M_{\rm WD}$, $\dot{m}_{\rm b}$, and $R_{\rm th}$) play a key role in shaping the profiles as well as in determining the shock heights and temperatures.

Starting with the threading region radius, we notice that from the Rankine–Hugoniot jump conditions (Equation (A15)), it follows that the greater $R_{\rm th}$, the greater the flow velocity at the shock position and, in turn, the greater $T_{\rm sh}$. This is nicely illustrated in Figures 3 and 4, where $T_{\rm sh}$ correlates with $R_{\rm th}$. Additionally, keeping all other parameters fixed, the values of $T_{\rm sh}$ are very sensitive to variations in $R_{\rm th}$, when it is in the range $1\,R_{\rm WD} \lesssim R_{\rm th} \lesssim 10\,R_{\rm WD}$. In particular, $T_{\rm sh}$ can vary by a factor of $\sim$4 when changing $R_{\rm th}$ from low to high values. Moreover, as $T_{\rm sh}$ increases with $R_{\rm th}$, so does $H_{\rm sh}$, as the higher-energy plasma needs a longer time to cool down, irrespective of the cooling efficiency. Finally, the shape of the profiles only negligibly changes with $R_{\rm th}$.

Regarding the WD magnetic field strength, comparing the panels for 1 MG with those for 30 MG, we notice that $H_{\rm sh}$ is smaller and $T_{\rm sh}$ is greater in the cases of stronger $B_{\rm p}$. This is because the cooling efficiency is enhanced by cyclotron radiation and thus the stronger $B_{\rm p}$ is, the more efficient the cooling. This implies that for sufficiently strong $B_{\rm p}$, values of $H_{\rm sh}$ might be extremely low. As $H_{\rm sh}$ becomes smaller for stronger $B_{\rm p}$, the gas hits the shock at larger velocities, which implies that $T_{\rm sh}$ increases. Despite the abovementioned correlation and anticorrelation, we notice that $T_{\rm sh}$ does not change drastically, unlike $H_{\rm sh}$, which is strongly affected by $B_{\rm p}$ (see Figure 6 in Section 3.2). Finally, unlike the above-discussed case of $R_{\rm th}$, the profile shape is hugely affected by $B_{\rm p}$, provided that all other parameters are kept the same. In fact, as $B_{\rm p}$ increases, the average temperature in the PSR decreases. This is because of cyclotron cooling, which is greater for stronger $B_{\rm p}$ and makes the profiles flatter, leading to a strong reduction of the temperature close to the shock. In particular, the greater $B_{\rm p}$ is, the more efficient the cyclotron cooling, and the greater is the difference between $T_{\rm sh}$ and the average temperature in the PSR. This causes the profiles to more closely resemble those of single-temperature plasmas as $B_{\rm p}$ increases.

With respect to the WD mass, we can clearly see the correlation between $M_{\rm WD}$ and $T_{\rm sh}$. As $T_{\rm sh}$ correlates with the flow velocity at the shock position, which in turn correlates with $M_{\rm WD}$, the greater $M_{\rm WD}$ is, the greater the flow velocity at the shock position, and, in turn, the greater the $T_{\rm sh}$. For more details, see Appendix B. In addition, we can see that $M_{\rm WD}$ also correlates with $H_{\rm sh}$, because a longer time is needed to cool down the hotter gas down, similarly to the case of $R_{\rm th}$. The WD mass, as in the case of $R_{\rm th}$, has no (or very little, if at all) impact on the shape of the T distribution.

Concerning the specific accretion rate, we found that it correlates with $T_{\rm sh}$ so that the greater $\dot{m}_{\rm b}$ is, the greater $T_{\rm sh}$. This is because both shock density and pressure are directly proportional to the specific accretion rate, which makes cooling more efficient. The dependence of $H_{\rm sh}$ on $\dot{m}_{\rm b}$ is a bit more complicated and will be discussed in Section 3.2. Finally, we notice that the shape of the T distribution is somewhat affected by $\dot{m}_{\rm b}$, becoming flatter as $\dot{m}_{\rm b}$ decreases.

After discussing how the four above-mentioned parameters separately affect the PSR structure, we turn to a discussion of their influence when compared together. For sufficiently large values of $\dot{m}_{\rm b}$, it is shown in Figures 3 and 4 that $B_{\rm p}$ has little impact on the profiles. However, as $\dot{m}_{\rm b}$ becomes smaller and smaller, even a relatively weak $B_{\rm p}$ might change substantially the T profiles. Indeed, comparing the three top panels in Figure 4, which correspond to $M_{\rm WD} = 0.6\,M_\odot$, the profiles are different for different values of $\dot{m}_{\rm b}$. In particular, the T distributions for $\dot{m}_{\rm b} = 1$ g s^{-1} cm^{-2} are less affected by $B_{\rm p}$ than the profiles for $\dot{m}_{\rm b} = 0.1$ g s^{-1} cm^{-2}. However, when comparing the three bottom panels, which correspond to $M_{\rm WD} = 1.0\,M_\odot$, we notice that the profiles for $\dot{m}_{\rm b} = 1$ g s^{-1} cm^{-2} are more affected by $B_{\rm p}$ than the corresponding profiles associated with $M_{\rm WD} = 0.6\,M_\odot$. This means that combinations of $M_{\rm WD}$, $B_{\rm p}$, and $\dot{m}_{\rm b}$ might potentially lead to qualitatively very different PSR temperature structures. The reason for this behavior is connected with the balance between bremsstrahlung and cyclotron radiative processes and will be discussed in more detail in the next section.

3.2. Cyclotron Cooling versus Bremsstrahlung Cooling

As briefly discussed before, the balance between bremsstrahlung and cyclotron radiative processes plays an

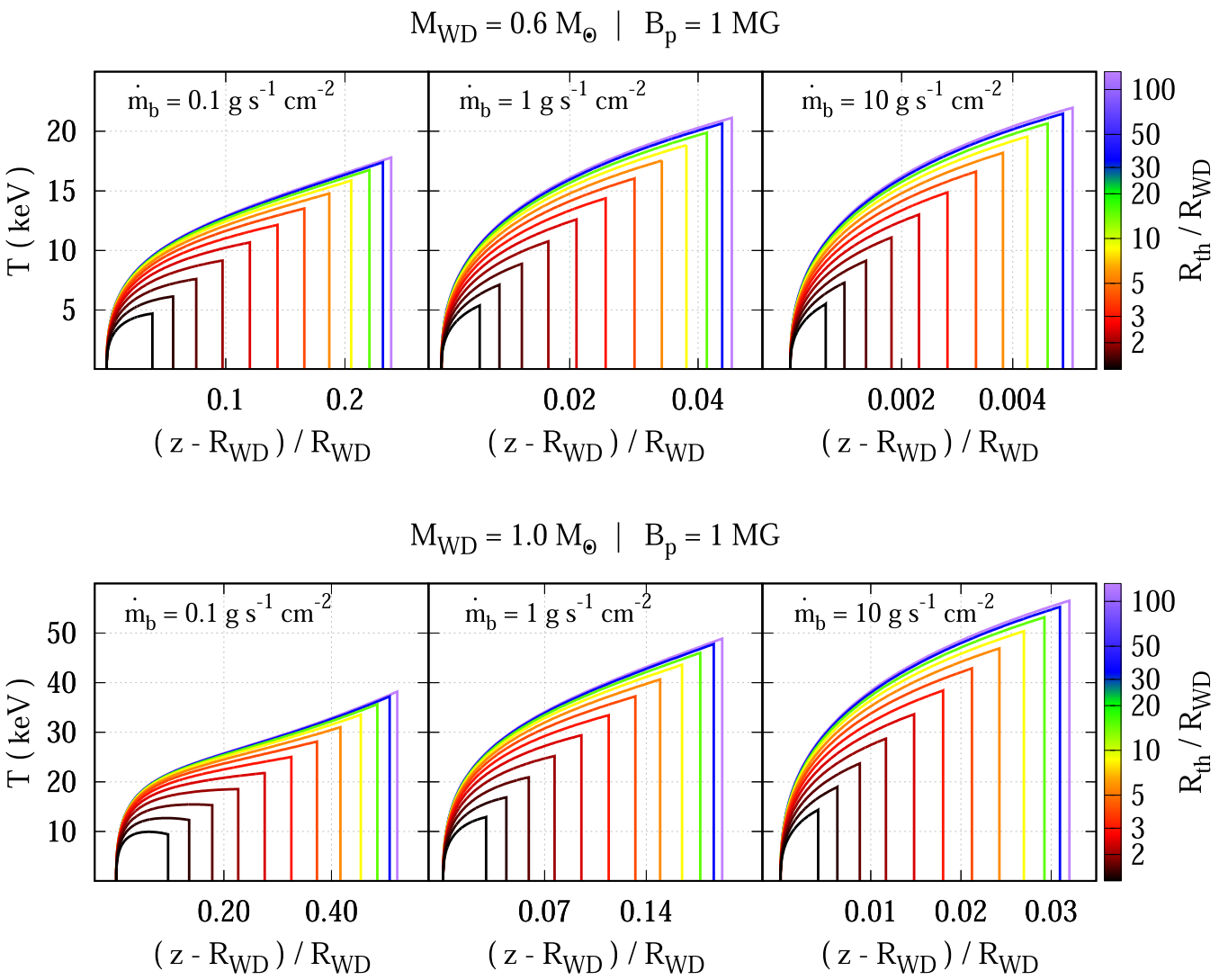

Figure 3. Temperature profiles in PSRs defined by particular choices of the model parameters. We fixed the WD magnetic field strength $B_p = 1$ MG in all panels and compare the solutions for two values of the WD mass (M_{WD}), namely 0.6 $M_\odot$ (top row) and 1.0 $M_\odot$ (bottom row). We further assume that the specific accretion rate $\dot{m}_b$ is 0.1, 1, and 10 g s^{-1} cm^{-2} in the left, middle, and right panels, respectively. Finally, in each panel, the profiles are color coded according to different values of the threading region radius (R_{th}). In all profiles, for simplicity, we set the other CYCLOPS parameters as in the standard model (Table 1). The M_{WD}, $\dot{m}_b$, and R_{th} play a sufficiently important role in shaping the T distributions and determining the shock heights (H_{sh}) and temperatures (T_{sh}). In particular, the greater M_{WD} and/or the greater $\dot{m}_b$, and/or the greater R_{th}, the greater T_{sh}. Similarly, the greater M_{WD} and/or the greater R_{th}, the greater H_{sh}. On the other hand, $\dot{m}_b$ can correlate or anticorrelate with H_{sh}, depending on B_p, as discussed in detail in Section 3.2. The correlations above are a direct consequence of the interplay between the cooling efficiency and physical conditions at the shock position.

important role in shaping the PSR structure. Before exploring this balance a bit further, it is convenient to discuss which parameters mainly contribute to both processes. From Equation (A18), we can see that the density in the PSR is the main parameter responsible for the cooling by bremsstrahlung. In particular, the greater the density, the stronger the bremsstrahlung emission, and because the density depends on the amount of gas in the PSR, it is not difficult to correlate it with the specific accretion rate (Equation (A15)). Thus, it naturally follows that the greater the $\dot{m}_b$, the stronger the bremsstrahlung emission and consequently the more efficient the cooling by bremsstrahlung. On the other hand, from Equations (A19) and (A20), it is clear that the greater B_p is, the stronger the cyclotron emission, and the more efficient is the cooling due to the cyclotron radiation.

These correlations can be seen in Figure 5, where we show profiles regarding the ratio between cyclotron and bremsstrahlung cooling (i.e., $\Lambda_{cyc}/\Lambda_{brem}$), for different values of B_p, $\dot{m}_b$, and M_{WD}. In all cases, all other parameters are set as in the standard model (Table 1). The variation in R_{th} causes negligible differences in $\Lambda_{cyc}/\Lambda_{brem}$, so it is not discussed.

For models with high accretion rates (i.e., $\dot{m}_b \gtrsim 10$ g s^{-1} cm^{-2}) and low WD masses (i.e., $M_{WD} \lesssim 0.8\ M_\odot$), bremsstrahlung dominates in the entire PSR, even for relatively high magnetic fields (~60 MG). However, models with high accretion rates and high WD masses (i.e., $M_{WD} \gtrsim 0.8\ M_\odot$), cyclotron contributes up to the half of PSR close to the shock and bremsstrahlung in at least the other half of the PSR (close to the WD surface).

Regarding models with low accretion rates (i.e., $\dot{m}_b \lesssim 0.1$ g s^{-1} cm^{-2}), bremsstrahlung dominates in the entire PSR only for relatively weak magnetic fields ($\lesssim$1 MG). Otherwise, cyclotron is more important for more than 50% of the PSR from the shock, and bremsstrahlung is important only close to the WD surface, where density is much higher. The above-mentioned feature takes place regardless of the WD mass.

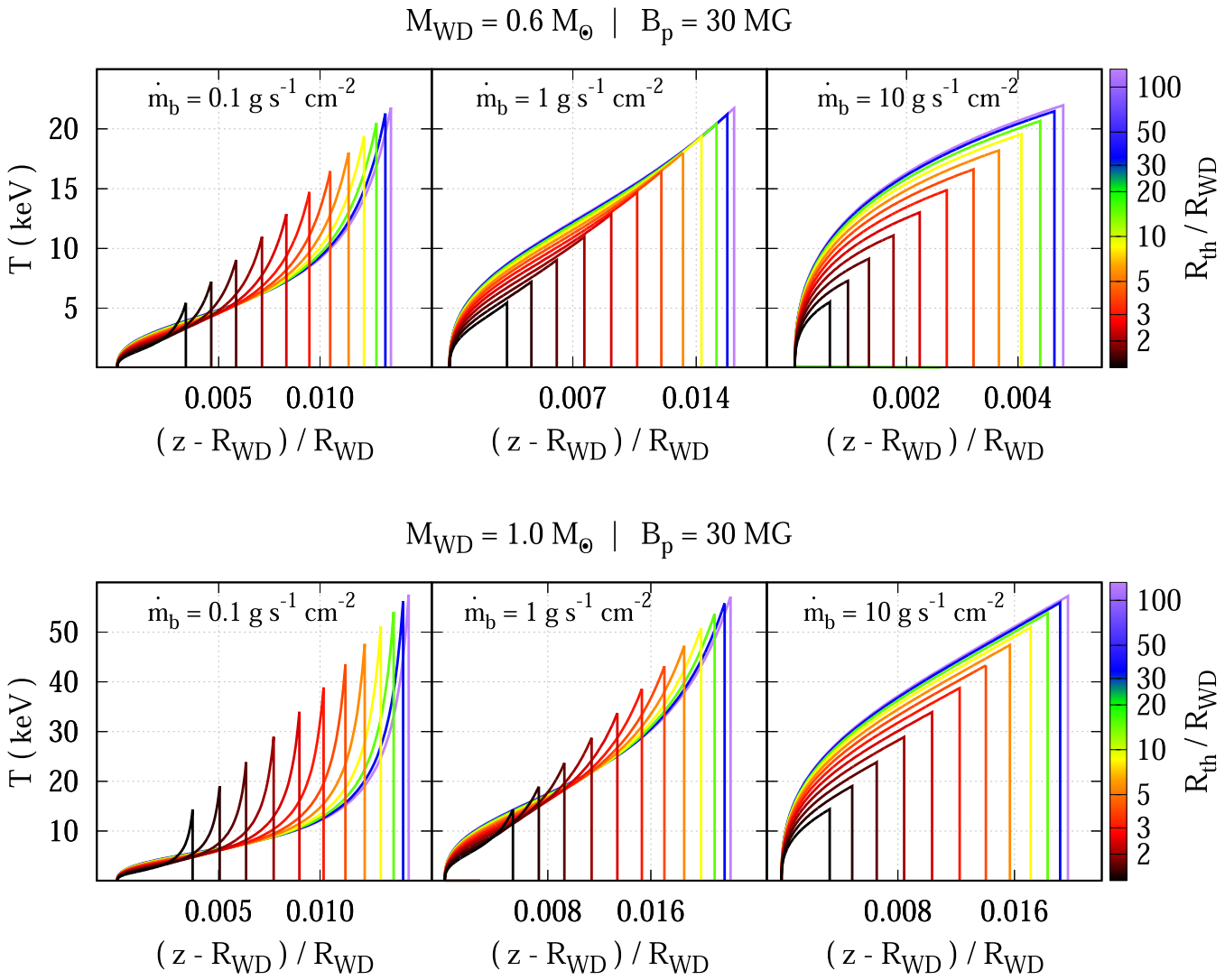

Figure 4. Temperature profiles in PSRs defined by the same choices of model parameters as in Figure 3, with exception of the WD magnetic field strength (B_p), which is 30 MG here, while, in Figure 3, it is 1 MG. The impact of increasing B_p is seen in the shock height (H_{sh}), which is smaller, and in the shock temperature (T_{sh}), which is greater. The decrease in H_{sh} takes place because, for stronger B_p, the total cooling becomes more efficient, due to enhanced cyclotron radiation. This results in more energetic gas at the shock position, which leads to an increase in T_{sh}.

Moreover, should $\dot{m}_b$ be even smaller, then magnetic fields weaker than ∼1 MG would be already enough to affect the PSR structure.

Concerning models with moderate accretion rates (i.e., $\dot{m}_b \sim 1$ g s^{-1} cm^{-2}), cyclotron becomes important only for moderate to high magnetic fields ($\gtrsim$10 MG). In particular, a value of $B_p = 30$ MG is already enough for cyclotron to play a role in at least half of the PSR irrespective of the WD mass. For values of B_p between ∼10 and ∼30 MG, cyclotron is important only for high-mass WDs.

Regardless of the magnetic field strength, bremsstrahlung always dominates the cooling process in PSR bottom, close to the WD surface, i.e., at least ∼20% of the PSR. In addition, the smaller the B_p, the greater the fraction of the PSR, from the bottom, dominated by bremsstrahlung emission.

By inspecting the panels in Figure 5, we can see that for all combinations of B_p and $\dot{m}_b$, the greater M_{WD}, the greater $\Lambda_{cyc}/\Lambda_{brem}$. This is because, by considering all other parameters fixed, the greater M_{WD}, the more energetic the flow and in turn the longer the cooling timescale, which leads to higher shock heights and PSRs with lower densities. This makes the relative importance of cyclotron cooling greater as M_{WD} increases.

Proceeding further with the competition between cyclotron and bremsstrahlung radiative processes, we show in Figure 6 how the shock height ($H_{sh;}$ top row) and the cooling ratio (ϵ_{sh}; Equation (A19), bottom row) depend on model parameters, for three different values of M_{WD}, namely, 0.4, 0.8, and 1.2 $M_\odot$, and several combinations of B_p (from 0 to 90 MG) and $\dot{m}_b$ (from $\sim 10^{-4}$ to $\sim 10^{3}$ g s^{-1} cm^{-2}), keeping the remaining parameters as in the standard model (Table 1).

In the case of negligible cyclotron cooling, the shock height always increases with decreasing specific accretion rate. This is because the smaller the specific accretion rate, the smaller the density in the PSR and in turn the weaker the bremsstrahlung emission. This leads to a decrease in the plasma cooling rate and consequently an increase in the bremsstrahlung cooling timescale as the specific accretion rate decreases, yielding taller PSRs. However, in the presence of nonnegligible cyclotron cooling, the shock height does not always increase as the specific accretion rate decreases.

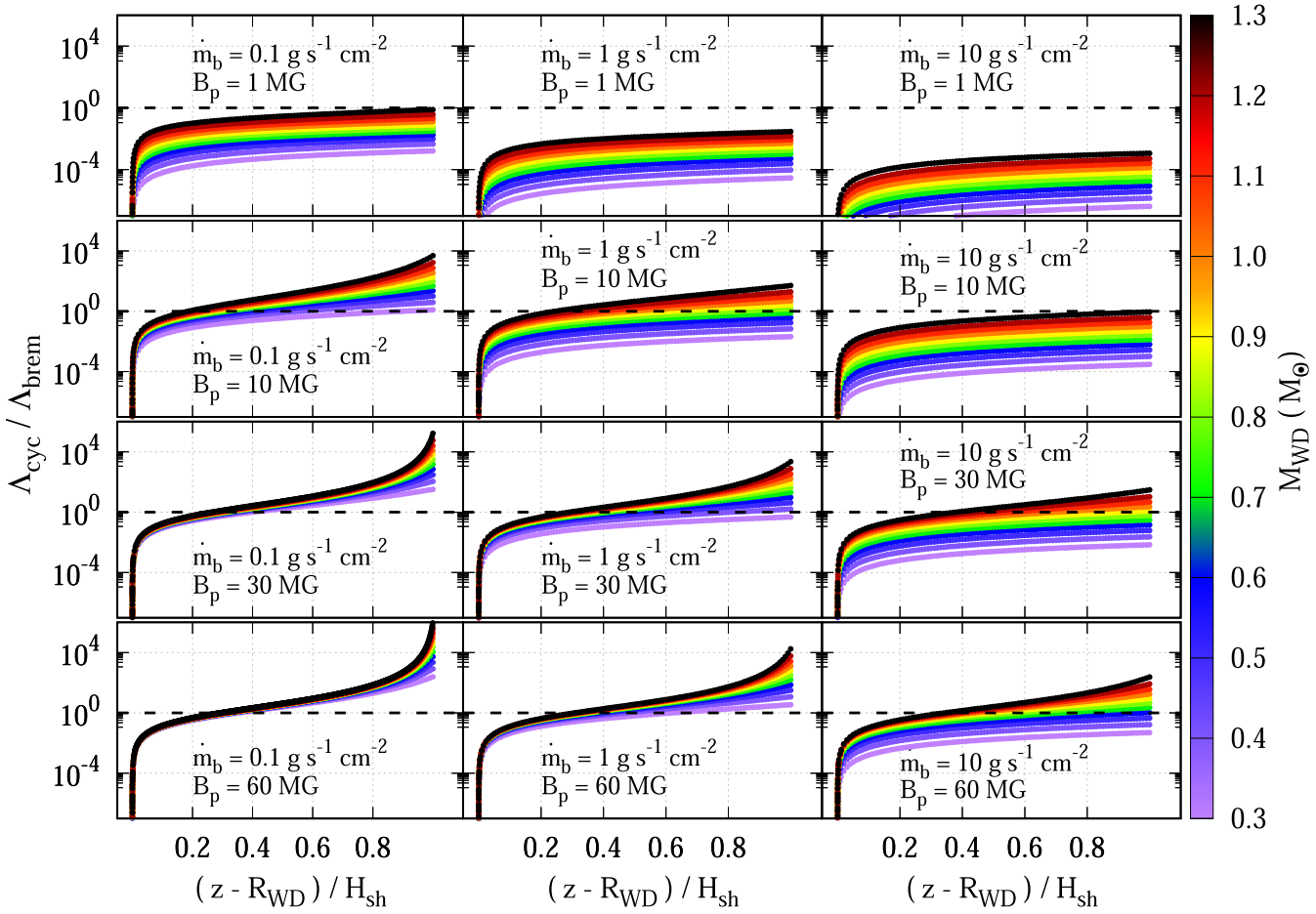

Figure 5. Cyclotron cooling over bremsstrahlung cooling ($\Lambda_{cyc}/\Lambda_{brem}$) in the z-direction from the WD surface until the shock height (H_{sh}), for different combinations of B_p, $\dot{m}_b$ and M_{WD}. In all cases, we set the nonspecified parameters as in the standard model (Table 1). We set three values for $\dot{m}_b$, namely 0.1 (left column), 1 (middle column), and 10 (right column), in units of g s^{-1} cm^{-2}; four values for B_p, namely 1 (first row), 10 (second row), 30 (third row), and 60 (fourth row), in units of MG. In each panel, the color bar corresponds to M_{WD}, which has values, in $M_\odot$, from 0.3 to 1.3, in steps of 0.1. Additionally, the horizontal dashed line corresponds to $\Lambda_{cyc}/\Lambda_{brem} = 1$, which indicates the region where both radiative processes contribute equally to the cooling. Notice that the three parameters play a key role in the balance. In particular, the greater the B_p and/or the greater the M_{WD} and/or the smaller the $\dot{m}_b$, the more efficient the cooling due to cyclotron radiation.

In fact, there is a maximum shock height, which is defined by the balance between the bremsstrahlung and cyclotron cooling. For a given combination of M_{WD} and B_p, there is a critical specific accretion rate $\dot{m}_b^{crit}$ such that cyclotron/bremsstrahlung cooling is more important when $\dot{m}_b$ is smaller/greater than $\dot{m}_b^{crit}$. This can be seen in the top row of Figure 6, where an anticorrelation takes place between H_{sh} and $\dot{m}_b$ when $\dot{m}_b > \dot{m}_b^{crit}$, and a correlation otherwise.

The values of $\dot{m}_b^{crit}$ are given by the balance between bremsstrahlung and cyclotron processes, when the cooling ratio $\epsilon_{sh} \sim 1$, i.e., the ratio between the bremsstrahlung and cyclotron cooling timescales (τ_{brem}/τ_{cyc}) is $\sim$1. In the bottom row of Figure 6, we show how ϵ_{sh} depends on M_{WD}, B_p, and $\dot{m}_b$. The greater M_{WD}, or B_p, the greater ϵ_{sh}. This is because the greater those parameters are, the stronger the cyclotron radiation and in turn the cyclotron cooling. For $\dot{m}_b$, on the other hand, there is an anticorrelation with ϵ_{sh}, which is a consequence of the increase in bremsstrahlung radiation (and in turn a decrease in ϵ_{sh}) when $\dot{m}_b$ increases.

With respect to the critical specific accretion rate, we can see that the maximum H_{sh} for a given pair of M_{WD} and B_p takes place at the same $\dot{m}_b$ associated with $\epsilon_{sh} \sim 1$. Such a critical $\dot{m}_b$ separates the parameter space into two regimes, namely bremsstrahlung-dominated or cyclotron-dominated cooling. In other words, for a given triple (M_{WD}, B_p, $\dot{m}_b$), there is always an $\dot{m}_b^{crit}$, such that the flow is bremsstrahlung dominated when $\dot{m}_b > \dot{m}_b^{crit}$ and cyclotron dominated otherwise.

We show in Figure 7 the critical specific accretion rate at the location of the shock front ($\dot{m}_{sh}^{crit}$) as a function of M_{WD} and the WD magnetic field intensity at the shock location (B_{sh}). By fixing the cross section at the shock $S_{sh} = 10^{17}$ cm^2, according to Equation (A19), for a given pair (M_{WD}, B_{sh}), there is a unique value of $\dot{m}_{sh}$ such that $\epsilon_{sh} = 1$. The lines depicted in Figure 7 correspond to values of $\dot{m}_{sh}$ such that $\epsilon_{sh} = 1$, i.e., they are values of $\dot{m}_{sh}$ below which cyclotron emission cannot be ignored. In the figure, for a given value of $\dot{m}_{sh}$, all models defined by (M_{WD}, B_{sh}) above such a line have nonnegligible cyclotron emission. On the other hand, bremsstrahlung emission always dominates in the bottom region below the same line.

Notice that even though we can ignore cyclotron cooling for several cases of weak magnetic fields, for sufficiently low values of $\dot{m}_{sh}$ ($\lesssim 10^{-3}$ g s^{-1} cm^{-2}), even magnetic fields as weak as $\lesssim$0.1–1 MG are enough to play a role in the cooling process. In particular, for IPs with rather low accretion rates (e.g., those located below the orbital period gap), the assumption of ignoring cooling due to cyclotron, as done in several works, does not seem appropriate. On the other hand,

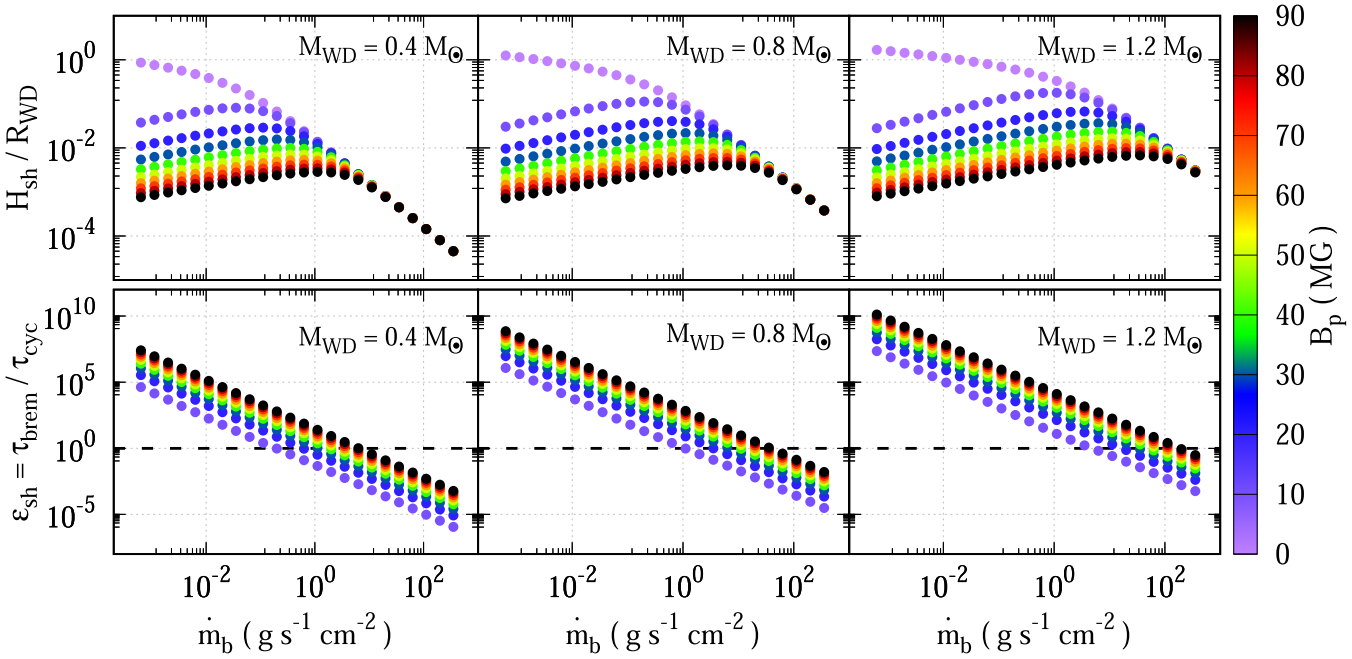

Figure 6. Shock height (H_{sh}) in units of the WD radius (R_{WD}), in the top row, and cooling ratio (ϵ_{sh}), i.e., the ratio between the bremsstrahlung and cyclotron cooling timescales (τ_{brem}/τ_{cyc}), in the bottom row, for different combinations of model parameters: M_{WD}, B_p, and $\dot{m}_b$. In all cases, for simplicity, we set the remaining parameters as in the standard model (Table 1). We took several values for $\dot{m}_b$ and B_p, and three values for M_{WD}, namely 0.4 (left panel), 0.8 (middle panel), and 1.2 (right panel), in units of $M_\odot$. In each panel, the x-axis corresponds to $\dot{m}_b$ and the color bar to B_p. Because B_p has to be nonnull for a consistent definition of ϵ_{sh}, the case $B_p = 0$ is only shown in the top row. Notice that when cyclotron cooling is negligible, the shock height always decreases with increasing specific accretion rates. However, for nonnegligible cyclotron cooling, there is always a maximum shock height for a given combination of M_{WD} and B_p, which is caused by the balance between the two physical processes responsible for the cooling, i.e., bremsstrahlung and cyclotron, and this takes place when $\epsilon_{sh} \sim 1$. In particular, for a given M_{WD} (or B_p), the greater the B_p (or M_{WD}), the greater the critical specific accretion rate such that the balance between bremsstrahlung and cyclotron takes place.

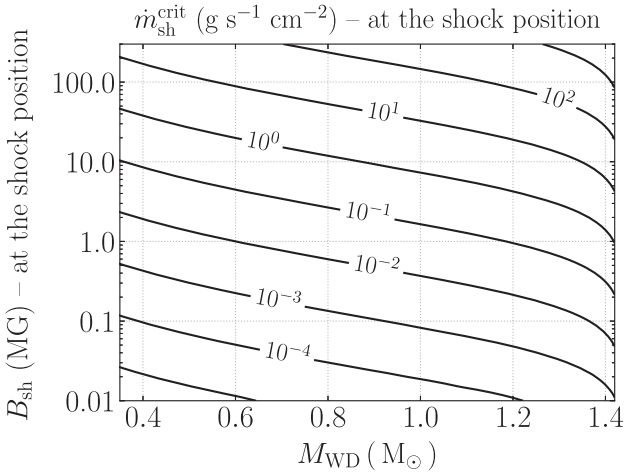

Figure 7. Critical specific accretion rate at the shock position ($\dot{m}_{sh}^{crit}$) such that for $\dot{m}_{sh} < \dot{m}_{sh}^{crit}$ cyclotron cooling cannot be ignored, as a function of the WD mass (M_{WD}) and the magnetic field strength at the shock position (B_{sh}), assuming $S_{sh} = 10^{17}$ cm^2. For a given $\dot{m}_{sh}$, there is a unique line in the plane defined by M_{WD} and B_{sh} so that all values in this line lead to the balance between bremsstrahlung and cyclotron, i.e., $\epsilon_{sh} = 1$. In this way, for a given $\dot{m}_{sh}$, all combinations of M_{WD} and B_{sh} above the line defined by such a specific accretion rate have nonnegligible cyclotron emission. For values of M_{WD} and B_{sh} below such a line, cyclotron cooling can be ignored.

for specific accretion rates as great as $\dot{m}_{sh} \gtrsim 100$ g s^{-1} cm^{-2}, even a very strong magnetic field is not enough to make cyclotron a relevant process.

We finish this section by saying a few words about the impact of the accretion area at shock position on the above-mentioned results. Even though we fixed $S_{sh} = 10^{17}$ cm^2 in Figure 7, we would like to emphasize that changing S_{sh} will affect only slightly those curves. Indeed, values greater (smaller) than that will slightly move the curves down (up) in the plane (M_{WD}, B_{sh}). This is because the dependence on S_{sh} in Equation (A19) is much weaker than the dependence on other parameters, which makes the influence of S_{sh} very small.

4. X-Ray Spectra and the Degeneracy Problem

After discussing how the model parameters affect both the balance between bremsstrahlung and cyclotron cooling and the temperature profiles in our PSRs, we can turn to the analysis of their influence on X-ray spectra as well as the unavoidable degeneracy in the parameter space.

To understand the dependencies and degeneracies of the predicted X-ray spectra, one needs to take into account an important correlation between the PSR temperature and the hardness of the X-ray spectra. The term hard X-rays corresponds to those photons carrying the highest energies ($\sim$10–100 keV), while those carrying the lowest energies ($\lesssim$10 keV) are referred to as the soft part of the X-rays. The greater the contribution toward higher energies, the harder the spectrum.

Throughout this paper, we have discussed hydrothermodynamical aspects of the accretion flow toward the WD surface. In such a picture, the potential energy of the infalling gas is converted into kinetic energy until it reaches the shock, where density and temperature are enhanced. Then, the greater the gas velocity at the shock, the higher the temperature, and the more energetic the bremsstrahlung emission in the PSR. Thus, the greater the temperature in the PSR, the harder the X-ray spectrum, or alternately, the greater the importance of the component associated with the highest energies. Keeping this

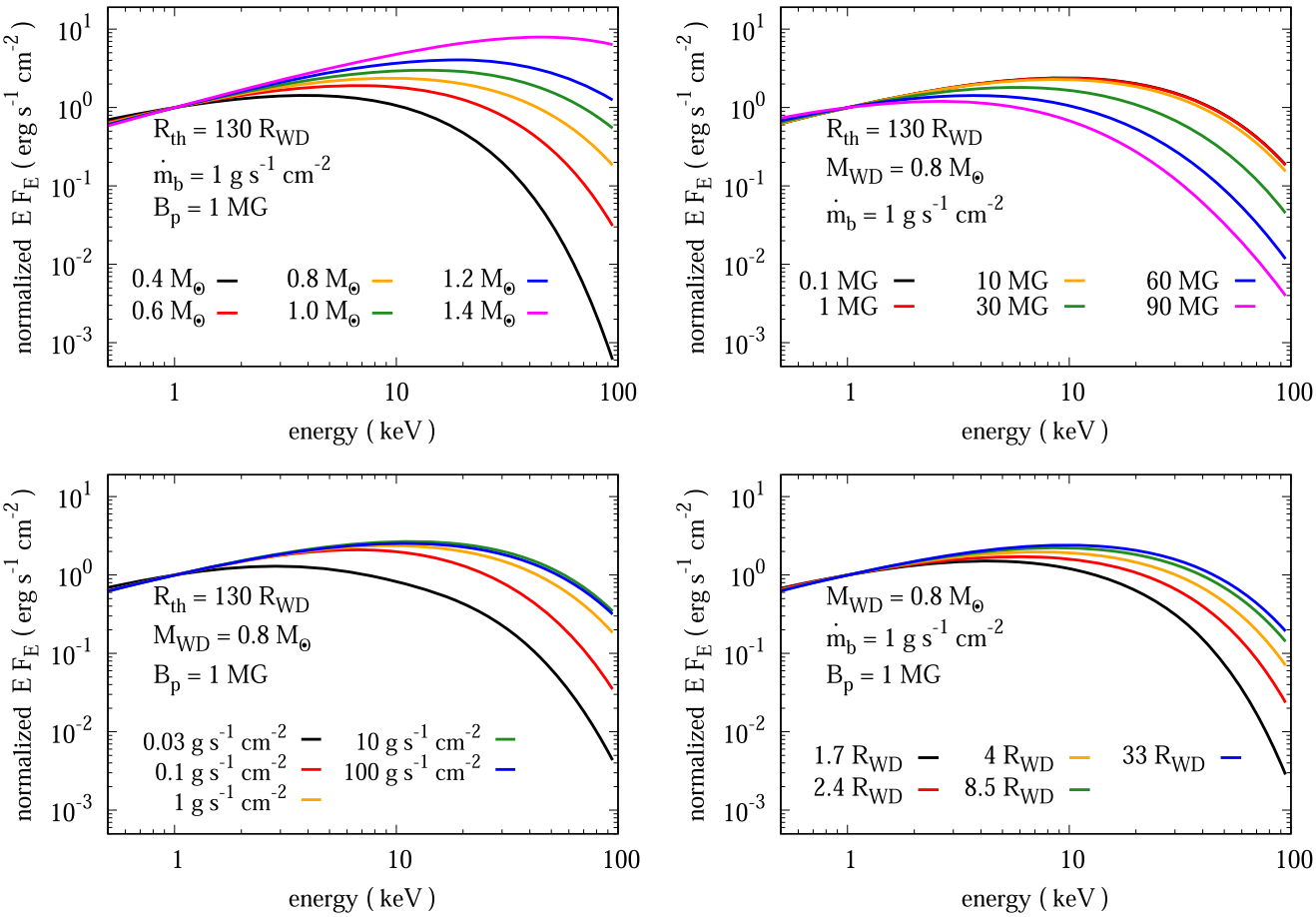

Figure 8. Mock X-ray spectra for several different combinations of $M_{\rm WD}$, $B_{\rm p}$, $\dot{m}_{\rm b}$, and $R_{\rm th}$. In all cases, for simplicity, we set the remaining parameters as in the standard model (Table 1) and normalized all spectra to their values at 1 keV. In all panels, we fixed all parameters but one, namely $M_{\rm WD}$ (top-left panel), $B_{\rm p}$ (top-right panel), $\dot{m}_{\rm b}$ (bottom-left panel), and $R_{\rm th}$ (bottom-right panel). These parameters, when fixed, are indicated in each panel and, when variable, in the keys. Notice that all four parameters play a key role in shaping the X-ray spectrum, especially $M_{\rm WD}$, after ∼10 keV. In particular, the greater the $M_{\rm WD}$ and/or the smaller the $B_{\rm p}$ and/or the greater the $\dot{m}_{\rm b}$ and/or the greater the $R_{\rm th}$, the harder the spectrum. See text for more details.

and Figures 3 and 4 in mind, in what follows we analyze how the X-ray spectrum hardness is affected by the main parameters describing the accretion structure in magnetic CVs.

4.1. X-Ray Spectra

An X-ray spectrum in the CYCLOPS code is entirely due to bremsstrahlung emission (see Section 2 for more details). That said, readers should bear in mind that other potentially important processes able to affect the hard part of the spectrum are not taken into account in the current version of the CYCLOPS code, such as Compton reflection from the WD surface, which is expected to contribute to the emission at energies higher than ∼10 keV. Despite that, X-ray spectra generated with the CYCLOPS code are in very good agreement with those generated by the widely used XSPEC code (see Appendix C for a detailed comparison between both codes).

We show mock X-ray spectra from the CYCLOPS code in Figure 8. For a proper comparison, all spectra have been normalized to their fluxes at 1 keV, which allows us to address the contribution of particular parameters to shape the spectra. This implies that the *y*-axis in this figure is somewhat artificial, which does not spoil the analyses, provided that our main goal here is to compare the spectrum shapes. In addition, no absorption was included, either internal or due to the interstellar medium, as this effect will be addressed separately in other parts of the paper. In order to generate the mock spectra, in all cases, we allowed four parameters to vary, namely $M_{\rm WD}$ (top-left panel), $B_{\rm p}$ (top-right panel), $\dot{m}_{\rm b}$ (bottom-left panel), and $R_{\rm th}$ (bottom-right panel), and fixed the remaining parameters as in the standard model (Table 1).

Starting with the influence of the WD mass, which is shown in the top-left panel of Figure 8, it is clear that the CYCLOPS code consistently predicts harder spectra for larger $M_{\rm WD}$. This is because the greater $M_{\rm WD}$ is, the higher the temperature in the PSR, and in turn the more enhanced the production of energetic photons. From the figure, it is also clear that all WD masses produce similar spectra until ≈1 keV. At energies greater than that, the lower the $M_{\rm WD}$, the faster the flux falls off toward higher energies. Even though there are differences between ≈1 and ≈10 keV, they become much more evident at the highest energies.

Regarding the influence of the WD magnetic field strength, which is depicted in the top-right panel of Figure 8, we see that for weaker $B_{\rm p}$, the spectra are harder. The higher the WD magnetic field is, the higher the extra cooling (relative to bremsstrahlung), causing smaller average temperatures in the PSRs for stronger $B_{\rm p}$, especially in the region from where the bremsstrahlung radiation comes, i.e., close to the WD surface (see also Figure 5). As in the case of the WD mass, spectra due to all values of $B_{\rm p}$ are rather similar until ≈1 keV, become

different after that until ≈10 keV, and become substantially different at higher energies. We notice that, given the particular choice of other parameters, spectra for $B_p \lesssim 10$ MG are indistinguishable.

With respect to the influence of the specific accretion rate, which is shown in the bottom-left panel of Figure 8, we notice that the larger the $\dot{m}_b$, the harder the spectrum. This is due to the clear correlation between the PSR temperature and the $\dot{m}_b$. A lower $\dot{m}_b$ leads to a smaller amount of matter and in turn a lower density, which causes a reduction in the cooling rate and in turn makes the PSR taller. As a result, the kinetic energy released at the shock is reduced, causing a reduction in the maximum temperature. As in the case of M_{WD} and B_p, the differences among spectra become larger toward higher energies. In addition, from the choice of other parameters, differences in the spectra for $\dot{m}_b \gtrsim 10$ g s^{-1} cm^{-2} are imperceptible.

Regarding the threading region radius, its impact on X-ray spectra is shown in the bottom-right panel of Figure 8. From the figure, we see that the greater the R_{th}, the harder the spectrum. This is due to the reduction of the available potential energy as R_{th} becomes smaller, which makes the corresponding kinetic energy smaller. This implies a reduction of the PSR temperature as shown in Figures 3 and 4. Unlike the other cases discussed above, the differences in the spectra start at energies a bit higher (≈3 keV). Even though differences become larger as the energy increases, like in other cases, we notice that spectra are more distinguishable at very high energies (≳30 keV). Moreover, given the choices of other parameters, the spectra for $R_{th} \gtrsim 8.5$ R_{WD} are virtually identical.

It is important to highlight at this point that the above-mentioned correlations have also been found in other works. For instance, Hayashi & Ishida (2014a) found that spectra are softer for lower specific accretion rates. In addition, Suleimanov et al. (2016) found that systems with smaller magnetosphere radius produce softer spectra. We can then conclude that X-ray spectra built with the CYCLOPS code present features that are in good agreement with previous works.

In the previously shown dependencies, absorption was not taken into account because our goal was to illustrate how each parameter affects the X-ray spectra. In what follows we will consider interstellar absorption (see Section 2) and its impact on X-ray spectra, which is illustrated in Figure 9, where we show spectra for different hydrogen column densities N_H. A clear correlation we can see from the figure is that the effect of absorption increases for lower energies. In addition, the greater the N_H, the stronger the absorption influence on the hard part of the spectrum. Indeed, for low values of N_H ($\lesssim 10^{20}$ cm^{-2}), absorption is negligible throughout the entire energy range of current X-ray instruments. On the other hand, for moderate values of N_H, i.e., $10^{20}\,\mathrm{cm}^{-2} \lesssim N_H \lesssim 10^{22}\,\mathrm{cm}^{-2}$, absorption plays a key role in shaping the continuum at energies $\lesssim$2–3 keV and is negligible at higher energies. Finally, for high values of N_H ($\gtrsim 10^{22}$ cm^{-2}), a larger proportion of the spectrum is subjected to absorption, and the greater the N_H, the greater the portion of the spectrum affected by absorption.

So far we have focused on normalized spectra because our goal was to investigate how model parameters affect their shape. However, the observed flux depends on the distance to the source, as illustrated in Figure 10, where we considered five distances, namely 100, 150, 300, 500, and 1000 pc. Because the flux depends on the inverse of the squared distance, the correlation seen in the figure is not surprising, i.e., the larger the

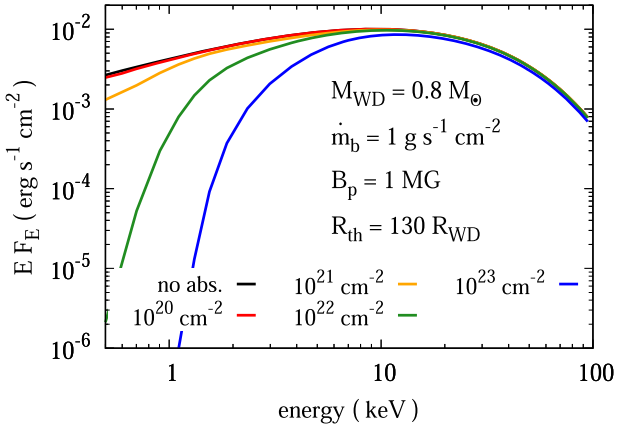

Figure 9. Mock X-ray spectra taking into account absorption for four different values of the hydrogen column density N_H, namely 10^{20}, 10^{21}, 10^{22}, and 10^{23}, in units of cm^{-2}, and a case with no absorption at all, which are indicated in the key. All parameters are fixed and set as in the standard model (Table 1). Notice that absorption is irrelevant for low values of N_H, i.e., $\lesssim 10^{20}$ cm^{-2}. For moderate values, i.e., $10^{20}\,\mathrm{cm}^{-2} \lesssim N_H \lesssim 10^{22}$ cm^{-2}, absorption might drastically change the spectrum below ≈2−3 keV. However, for sufficiently large values of N_H, i.e., $\gtrsim 10^{22}$ cm^{-2}, absorption plays a significant role in shaping the spectrum beyond ≈2−3 keV.

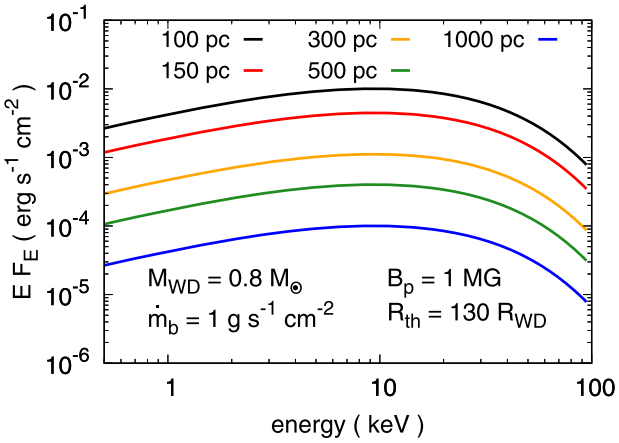

Figure 10. Mock X-ray spectra for the standard model (Table 1), taking into account different distances, namely 100, 150, 300, 500, and 1000 pc, which are indicated in the key. Clearly, as expected, the larger the distance, the lower the X-ray spectrum flux. Moreover, such a distance-dependent flux is consistent with the widely used XSPEC code (see Appendix C).

distance, the lower the spectrum flux. Most importantly, the distance-dependent X-ray flux in the CYCLOPS code has been properly calibrated using the XSPEC code (see Appendix C).

Even though we have not discussed the influence of other CYCLOPS geometrical parameters, such as the PSR colatitude, the WD magnetic field longitude, and orbital inclination, we stress that their impact on shaping X-ray spectra is negligible. Indeed, bremsstrahlung emission does not depend on the WD magnetic field direction, unlike cyclotron emission, important in optical bands. What is important for X-ray emission is the magnetic field orientation with respect to the rotation axis, i.e., the WD magnetic field latitude B_{lat} (e.g., Ferrario et al. 1989), which is embedded in R_{th} in the analysis we have been performing.

Concerning the orbital inclination, it also has no (or very weak, if at all) impact on the X-ray spectra. This is because, in the CYCLOPS code, bremsstrahlung is solely responsible for the X-ray emission, and the PSR is optically thin for

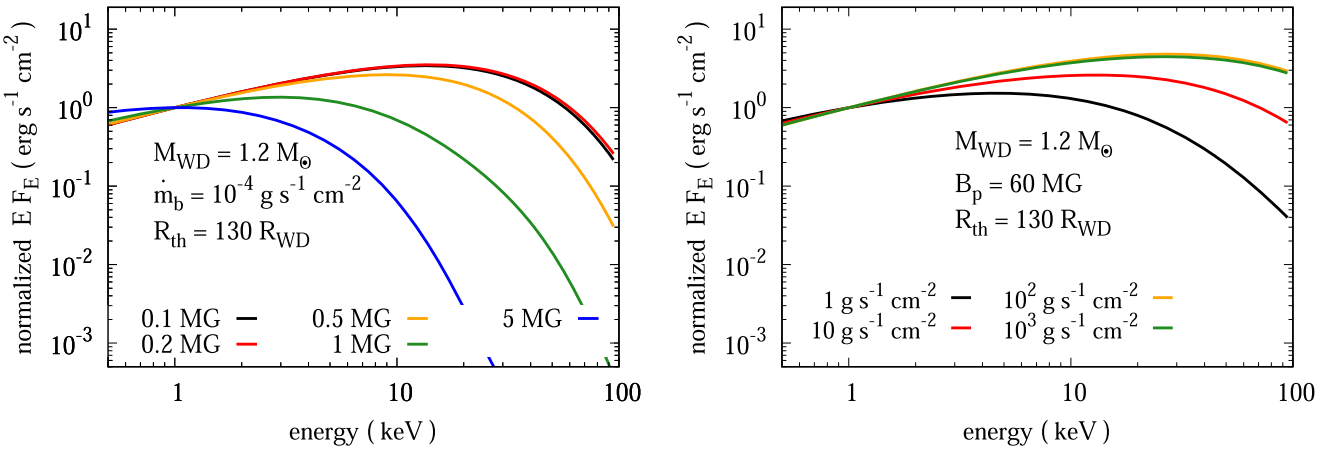

Figure 11. Mock X-ray spectra comparing the influence of B_p (left panel) and fixing $M_{WD} = 1.2\ M_\odot$ and $\dot{m}_b = 10^{-4}$ g s^{-1} cm^{-2}, and comparing the influence of $\dot{m}_b$ (right panel) and fixing $M_{WD} = 1.2\ M_\odot$ and $B_p = 60$ MG. In both panels, the remaining parameters are set as in the standard model (Table 1) and all spectra are normalized to their values at 1 keV. Notice that the thresholds leading to degeneracy in both panels are different than those in Figure 8, due to the balance between cyclotron and bremsstrahlung radiative processes, which causes a movement of the thresholds through the parameter space.

bremsstrahlung emission so that the direction by which it is seen does not matter. In this case, the emission is proportional to the bremsstrahlung emissivity integrated over the PSR volume. For high inclinations, the PSR is self-eclipsed in some spin phases causing a decrease in the average flux along the WD rotation. If the self-eclipse is partial, the spectrum shape can slightly change along the WD spin. As the temperature is not uniform in the PSR, the occulted portion can have different temperatures relative to the visible portion in a phase in which the PSR is partially behind the WD. And the resulting spectrum can differ from the spectrum produced when the entire PSR is visible. We would like to emphasize, though, that in the presence of other effects not included here (e.g., Compton humps, Hayashi et al. 2018), the inclination might be an important parameter to be considered, because such effects might strongly depend on the direction by which the PSR is seen.

4.2. The Degeneracy Problem

So far, we have discussed the influence of key parameters in shaping the X-ray spectrum individually. We will discuss in what follows how correlations among parameters affect the X-ray spectra, especially in creating degeneracies. This is rather important for the purposes of fitting schemes as one parameter might compensate another one, which implies that rather similar spectra might be built, even for very different combinations of the parameters.

While discussing Figure 8, we mentioned some thresholds for the parameters above (or below) for which the spectra look very similar. We would like to stress that such thresholds strongly depend on the combination of parameters. For example, we found that for $\dot{m}_b = 1$ g s^{-1} cm^{-2}, $M_{WD} = 0.8\ M_\odot$, and $R_{th} = 130\ R_{WD}$, there is a degeneracy among spectra for $B_p \lesssim 10$ MG, which is the threshold for this combination of parameters. However, as discussed in Section 3.2, due to the balance between cyclotron and bremsstrahlung radiative processes, there is a critical $\dot{m}_b$ below which cyclotron cooling dominates over bremsstrahlung cooling. That said, it is not surprising that this degeneracy might become restricted to smaller and smaller B_p, as $\dot{m}_b$ decreases. Indeed, for sufficiently low specific accretion rates, effects due to the WD magnetic field cannot be ignored anymore, as argued in Section 3.2. This means that the corresponding spectra are also different, even for relatively weak B_p.

This is illustrated in the left panel of Figure 11, where we show spectra for different values of weak B_p, for $\dot{m}_b = 10^{-4}$ g s^{-1} cm^{-2}, $M_{WD} = 1.2\ M_\odot$, $R_{th} = 130\ R_{WD}$, and the remaining parameters as in the standard model (Table 1). All spectra have been normalized to their fluxes at 1 keV. Notice that for such a low $\dot{m}_b$, the spectra start becoming degenerate at $B_p \sim 0.2$ MG, which is the threshold for this combination of parameters. Thus, there is practically no distinction among spectra when B_p is weaker than that.

Another example we discussed is for the combination $M_{WD} = 0.8\ M_\odot$, $B_p = 1$ MG, and $R_{th} = 130\ R_{WD}$, which drives a degeneracy among spectra when $\dot{m}_b \gtrsim 10$ g s^{-1} cm^{-2}, which is the threshold for this combination of parameters (see Figure 8, bottom-left panel). As in the above-discussed case, for sufficiently strong WD magnetic fields and massive WDs, such a similar behavior can be broken when $10\ \mathrm{g\,s^{-1}\,cm^{-2}} \lesssim \dot{m}_b \lesssim 100$ g s^{-1} cm^{-2}, but still remains for $\dot{m}_b \gtrsim 100$ g s^{-1} cm^{-2}. This is shown in the right panel of Figure 11, where we depict spectra for different values of high $\dot{m}_b$, for $B_p = 60$ MG, $M_{WD} = 1.2\ M_\odot$, $R_{th} = 130\ R_{WD}$, and the remaining parameters as in the standard model (Table 1). Notice that for such a different combination of M_{WD} and B_p, the onset of degeneracy moves from $\dot{m}_b \sim 10$ g s^{-1} cm^{-2} to $\dot{m}_b \sim 100$ g s^{-1} cm^{-2}.

So far, we have provided several examples in which, while fixing all parameters but one, we showed that there is a critical value for this variable parameter above/below which the differences in the resulting X-ray spectra are imperceptible. We can therefore deduce that such thresholds always exist, regardless of the combination of fixed parameters considered and the variable parameter analyzed. In addition, due to the balance between cyclotron and bremsstrahlung radiative processes, such thresholds move through the parameter space.

The approach we have considered requires a set of four parameters to be fitted, namely the WD mass, the WD magnetic field, the specific accretion rate, and the threading region radius, which are the most important parameters shaping the PSR temperature and density profiles, and, in turn, the X-ray spectra. Thus, we deal with a four-dimensional fitting problem, which can potentially get even more complicated by the addition of more geometrical parameters, such as those related

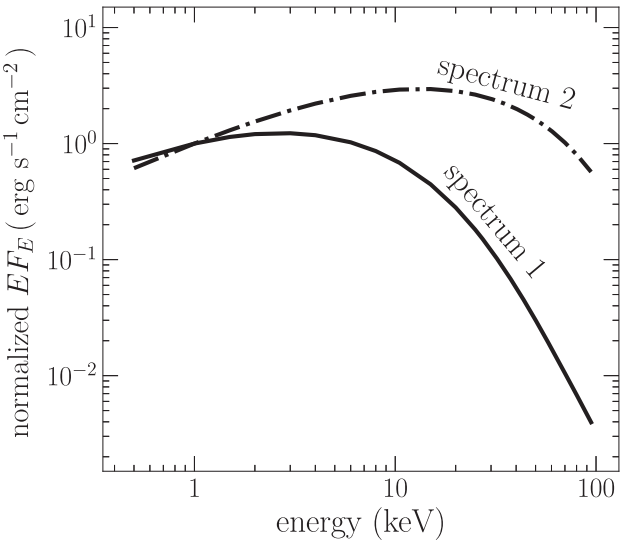

Figure 12. X-ray spectra associated with the two sets of models described in Table 2, normalized to their values at 1 keV. The spectra are very different, spectrum 2 being much harder than spectrum 1. Even though the models in each set are significantly different, they all lead to the same X-ray spectrum, likely because the average temperatures weighted by the squared density are rather similar in each set of models.

to the footprint of the PSR on the WD surface. That said, it is actually not surprising that many combinations of these four parameters could lead to X-ray spectra in accordance with an observed one. This happens because the parameters might compensate one another, leading to a rather similar X-ray spectrum.

For instance, in Section 4.1, we showed how the spectrum hardness correlates with the parameters. In particular, we showed that the greater the WD mass, the harder the spectrum. We also showed that the greater the threading region radius, the harder the spectrum. In this way, it seems rather probable that a high-mass WD combined with a small threading region radius could lead to a spectrum similar to that of a low-mass WD combined with a large threading region radius. In a similar fashion, many different combinations of model parameters can naturally lead to spectra that equally well fit an observed one.

In what follows, we will provide more generic examples in which several combinations of the four parameters investigated here lead to virtually identical X-ray spectra. This is an important issue for fitting schemes in magnetic CV emission modeling and becomes inevitable when only the X-ray spectrum is taken into account. Therefore, the degeneracy problem is a physical problem that needs to be consistently addressed in any fitting scheme. Aside from showing more generic examples characterizing the degeneracy problem, we will also discuss ways of solving this problem. Our approach should also potentially provide tools to investigate additional properties, such as the geometrical parameters as well as internal absorption.

4.3. Two Examples of Degenerated Spectra

In order to illustrate how the degeneracy problem affects X-ray fitting strategies, we consider here two sets of four different models, each set providing the same normalized X-ray continuum spectrum. These two spectra are shown in Figure 12 and the properties of the models that produce them are listed in Table 2. We show in Figure 13 the temperature profiles of all these eight models.

By inspecting Figure 12, we can clearly see that spectrum 2 is much harder than spectrum 1. In this way, we should expect much higher temperatures in the PSRs of the models associated with spectrum 2, which is in fact the case. The average temperatures weighted by the squared density in the PSR of the models producing spectrum 1 and spectrum 2 are ∼7–8 and ∼27–30 keV, respectively. In particular, these temperatures are quite similar in each set of models.

Regarding models 1a, 1b, 1c, and 1d, it is quite clear from the left panel of Figure 13 that their profiles are rather different. An interesting distinction among these models is the shock temperature, which can be different by a factor of 4. Another evident difference is the PSR height, which can vary by a factor of 10. The very short PSR in model 1d, in particular, is due to the very strong magnetic field strength, which makes the cyclotron cooling substantially enhanced, in comparison with the other models in this set (see Figure 6).

With respect to the second set of models, the situation is a bit different. Even though from the right panel of Figure 13 models 2b, 2c, and 2d look similar, they are different. By inspecting Table 2, despite the fact that these models have similar shock temperatures, they have considerably different shock heights, specific accretion rates, WD masses, and threading region radii. On the other hand, the threading region in model 2a is much closer to the WD, and it has a much smaller specific accretion rate and a much weaker magnetic field, in comparison with models 2b, 2c, and 2d, producing a much taller PSR. Despite that, its shock temperature is comparable to those in the other models, which is likely due to its much higher WD mass.

The geometrical properties of all models listed in Table 2 are shown in Figure 14, in which phase 0.1 was chosen. Despite all these models have the same orbital inclination (45°), the same magnetic field latitude (90°), and longitude (0°), they are geometrically very different. For instance, the PSR colatitude and the PSR cross section of all models are substantially different. The models in the set spectrum 2 are particularly interesting. The PSR approaches the magnetic pole, as one moves from model 2a to model 2d. This in turn causes the threading region to move farther away from the WD, from model 2a to model 2d. Interestingly, the PSR cross sections of models 2c and 2d are so small that we cannot even see those PSRs in the figure.

A hard spectrum like spectrum 2 can be achieved in several ways. For instance, spectra associated with high-mass WDs can be very hard, as well as spectra connected with either weak fields or high specific accretion rates. All models in the set spectrum 2 have relatively high WD masses ($\gtrsim$0.9 $M_\odot$), relatively high specific accretion rates ($\gtrsim$10 g s^{-1} cm^{-2}), and very diverse magnetic field strengths as well as threading region radii.

Model 2a in this set is particularly interesting as it has the highest WD mass, the lowest field strength, the lowest specific accretion rate, and the smallest threading region radius. These characteristics imply that this model has the tallest and sparsest PSR in this set. Should this model be more representative of a hypothetical CV exhibiting spectrum 2, such a CV would be a very peculiar IP, because it would harbor an unusually high-mass WD.

On the other hand, model 2c seems quite close to the properties of most polars, provided its WD mass is consistent

Table 2
Parameters of the Models Discussed in Section 4.3

Model	M_{WD} ($M_\odot$)	B_p (MG)	$\dot{M}_{WD}$ (10^{-10} $M_\odot$ yr^{-1})	S_b (10^{16} cm^2)	$\dot{m}_b$ (g s^{-1} cm^{-2})	β (^{o})	R_{th} (R_{WD})	H_{sh} (R_{WD})	T_{sh} (keV)	ρ_{sh} (10^{-9} g cm^{-3})	$\langle T \rangle$ (keV)
Spectrum 1											
1a	1.35	29	0.50	1.58	0.20	48	1.80	0.0146	83	0.92	7.7
1b	1.18	21	0.39	1.66	0.15	45	1.99	0.0217	45	0.93	7.7
1c	1.06	63	15.85	8.74	1.14	50	1.72	0.0057	29	9.25	7.4
1d	0.74	141	15.84	4.05	2.47	27	4.82	0.0019	25	21.46	7.1
Spectrum 2											
2a	1.29	1	15.85	1.30	7.69	54	1.52	0.0424	43	45.68	28.9
2b	1.03	68	63.10	0.68	58.93	28	4.48	0.0036	49	365.66	28.5
2c	0.94	26	0.63	0.11	35.54	14	18.35	0.0057	48	221.45	29.6
2d	0.87	44	3.98	0.03	95.38	2	1136.27	0.0019	43	633.39	27.4

Note. The parameters are the WD mass (M_{WD}), the WD magnetic field strength at the pole (B_p), the accretion rate ($\dot{M}_{WD}$), the accretion area at the PSR bottom (S_b), the specific accretion rate at the PSR bottom ($\dot{m}_b$), the PSR colatitude (β), the threading-region radius (R_{th}), the shock height (H_{sh}), the shock temperature (T_{sh}), the shock density (ρ_{sh}), and the average temperature weighted by the squared density ($\langle T \rangle$). For the other CYCLOPS parameters, we assumed an orbital inclination of 45°, a distance of 100 pc, a magnetic field latitude of 90°, and a magnetic field longitude of 0°. Finally, we assume that the interstellar extinction is negligible.

with what is found among CVs, its WD hosts a moderately strong magnetic field, and it has a low accretion rate and a relatively large threading region radius. Apart from these few notes, one cannot conclude which of these models better describes a CV exhibiting an X-ray continuum spectrum like spectrum 2. To disentangle the models, one would inevitably need to know more properties of such a system and/or to have additional constraints. In other words, an X-ray continuum spectrum alone does not tell us much about the properties of a given magnetic CV.

An example of misleading assumptions in schemes to estimate magnetic CV properties is the modeling of EX Hya performed by Luna et al. (2015) and Suleimanov et al. (2016, 2019). Given the lack of further constraints, in the previous work, the authors assumed the same values for the magnetosphere radius derived in Revnivtsev et al. (2011) and Semena et al. (2014), which is ≈2.7 R_{WD}. In the first attempt using their break frequency method, Suleimanov et al. (2016) assumed that this system had a short PSR, given the high specific accretion rates they assumed, and found the WD mass and magnetosphere radius of this system should be ≈0.73 $M_\odot$ and ≈2.6 R_{WD}, respectively, agreeing in turn with the results achieved by Revnivtsev et al. (2011) and Semena et al. (2014).

However, Luna et al. (2018) investigated EX Hya with X-ray data from several satellites and found that it has a tall PSR, with a height comparable to its WD radius. In addition, these authors showed that its magnetosphere is most likely much larger than that predicted by the break frequency method, but smaller than its corotation radius. By knowing that, Suleimanov et al. (2019) then assumed that EX Hya has a relatively tall PSR (0.25 R_{WD}), still smaller than the height estimated from X-ray observations ($\sim R_{WD}$). In this case, they found a better agreement with the WD mass derived from eclipses, but still significantly smaller. Their inferred magnetosphere radius is still small (≈3 R_{WD}), though.

Another problem in the analysis of Suleimanov et al., for this particular system, is that the break frequency method used by these authors does not seem to work for EX Hya. The Doppler tomograms performed by Mhlahlo et al. (2007) reveal that this system has a large accretion curtain (see also Norton et al. 2008), extending to a distance close to the WD Roche lobe radius, while that estimated with the break frequency is at most a few R_{WD}.

The example above clearly illustrates how assumptions made in X-ray continuum spectra fitting might become dangerous. Such assumptions are otherwise needed because of the intrinsic degeneracy problem coupled with the lack of observational constraints because an X-ray continuum spectrum alone does not provide the information required to properly constrain the parameter space in this sort of fitting scheme.

5. Methods of Breaking the Degeneracy in the Parameter Space

So far, we have discussed the degeneracy problem, i.e., the degeneracy arising from the number of parameters to be fitted, in a very general fashion. It is similarly important to provide possible solutions that can potentially help to break the degeneracy in the parameter space. The only way to solve the degeneracy problem is by introducing additional constraints to the fitting scheme so that the models could be distinguished. We discuss in this section approaches using X-ray data that can break the degeneracy by focusing on the two sets of four different models introduced in Section 4.3.

5.1. Breaking the Degeneracy with Emission Lines

A way of increasing the constraints for particular systems is the inclusion of emission lines in the X-ray spectra because they provide extra constraints for the parameters of the PSR. For instance, Hayashi & Ishida (2014a) showed that the ratio of the hydrogen-like to the helium-like iron $K\alpha$ lines changes with respect to the specific accretion rate. This and other line complexes might help to break the degeneracy as the line emission spectrum strongly depends on the PSR temperature and density distributions (e.g., Fujimoto & Ishida 1997; Ezuka & Ishida 1999; Ishida & Ezuk 1999).

In addition, one could extract useful information about the shock height from the iron fluorescent line and the Compton hump. Examples of objects in which this sort of estimate was possible include EX Hya (Luna et al. 2018) and V1223 Sgr (Hayashi et al. 2011). Knowing the PSR height can, to some degree, help in breaking the degeneracy. This information, for

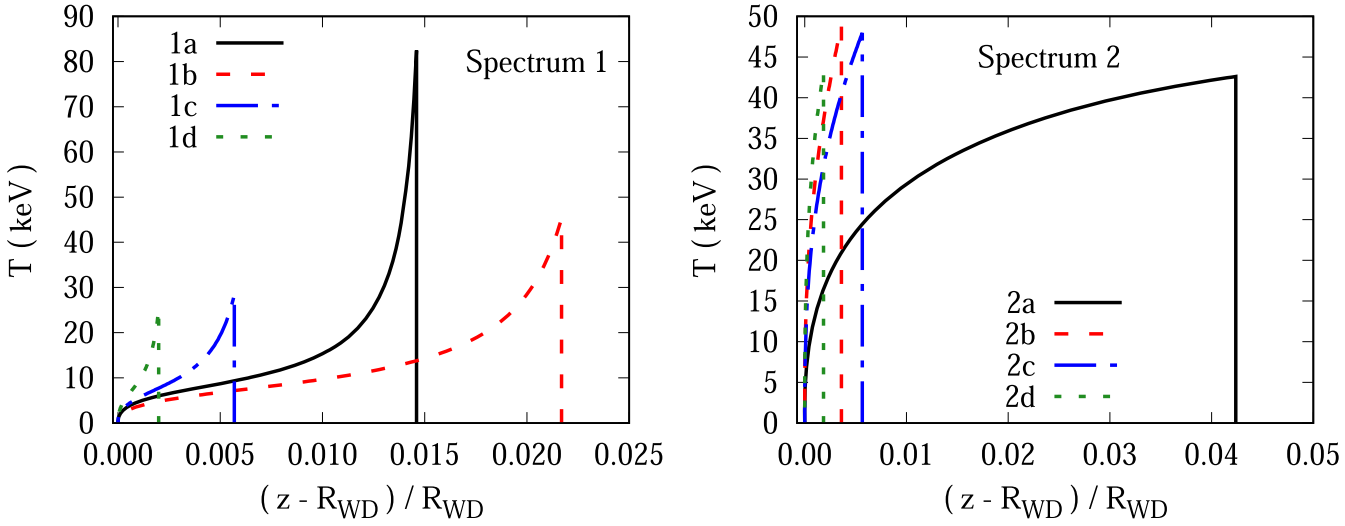

Figure 13. PSR temperature distributions of the models listed in Table 2, the set spectrum 1 being shown in the left panels and the set spectrum 2 in the right panels. We can clearly see that the profiles of the models are different. However, the model average temperatures weighted by the squared density, in each set, are rather similar, which helps to explain why they exhibit the same normalized X-ray spectrum.

instance, could help to distinguish the models in the set spectrum 1 and eventually model 2a from models 2b–d in the set spectrum 2 (see Figure 13).

Therefore, even though incorporating emission lines to the fitting strategy should help, this effect alone seems unable to solve the degeneracy problem. This is especially true if we take into account that line emission also depends on the elemental abundances, which introduce an additional parameter to the fitting scheme. Unfortunately, addressing to what extent emission lines help cannot be currently done with the CYCLOPS code, as it cannot handle emission lines, but it should be verified in future works.

5.2. Breaking the Degeneracy with Consistent Break Frequency Estimate

For some IPs, accurate hard X-ray observations are or will become available (e.g., through the NuSTAR Legacy Survey program; Shaw et al. 2020). A property that can sometimes be extracted from the power spectrum in these cases is the break frequency (e.g., Suleimanov et al. 2016, 2019), which corresponds to the Keplerian frequency at the magnetosphere boundary (e.g., Revnivtsev et al. 2009, 2010, 2011). From that, the magnetosphere radius can be estimated, which decreases the number of free parameters in the fitting scheme.

The main difficulty of this approach is that the break frequency cannot be usually/easily extracted from the data. For instance, Shaw et al. (2020) analyzed a sample of 19 magnetic CVs with NuSTAR and could estimate the break frequency for only one of them. For the remaining systems, these authors assumed either spin equilibrium, in which the magnetosphere radius is the corotation radius, for the other 16 IPs in their sample, or that the magnetosphere radius was $10^3\,R_{\rm WD}$, in the case of the two asynchronous polars they analyzed.

We can then conclude now that estimating the break frequency is not an easy task. Even worse, it might not necessarily provide an accurate estimate of the magnetosphere radius (see Luna et al. 2018 for a discussion related to EX Hya). Therefore, despite the fact that it can be useful, wherever it is possible to apply this method, it is most likely not enough to solve the degeneracy problem, especially considering the multidimensional parameter space involved in magnetic CV modeling, like the one investigated here.

5.3. Breaking the Degeneracy with Consistent Preshock Region Modeling

A spectrum in the CYCLOPS code corresponds to the combination of spectra in different rotational phases. In each phase, the extinction of the preshock region is calculated according to the model accretion geometry and inclination. Therefore, the PSR emission and preshock extinction are consistently calculated for a given model. In particular, CYCLOPS can produce the spectrum resulting of a partial absorption from the preshock region, similar to what is done by the PCFABS model of XSPEC, which is widely used to reproduce magnetic CV spectra. However, CYCLOPS has an approach consistent with the 3D adopted geometry for the entire accretion structure (PSR and preshock region), which is required to properly model the phase-dependent flux modulation of magnetic CVs.

We illustrate in Figure 15 how the spectra shown in Figure 12 can be modified when the preshock region extinction is taken into account. As described in Section 2.2, this region is expected to extinguish the PSR emission by photoelectric absorption and Compton scattering. The spectra, which are normalized to their values at 1 keV, were calculated considering a partially ionized preshock region that has a constant density equals one-fourth of the density at the shock front. Regardless of the model, we can clearly see that the preshock region can produce nonnegligible changes in the spectrum shape, especially for energies below a few keV. This is not surprising and can be explained by the dependence of the photoabsorption cross section on the energy as absorption more strongly affects the soft region of the spectrum. On the other hand, even though Compton scattering, which affects the hard part of the spectrum, does not usually play a significant role in shaping the spectra of the models, it is sufficiently important in models 2b and 2d, reducing, in turn, the flux in these models.

Regarding the models in the set spectrum 1, there are two pairs of models with very similar spectra. While the spectra of models 1 c and 1d are strongly affected by preshock region

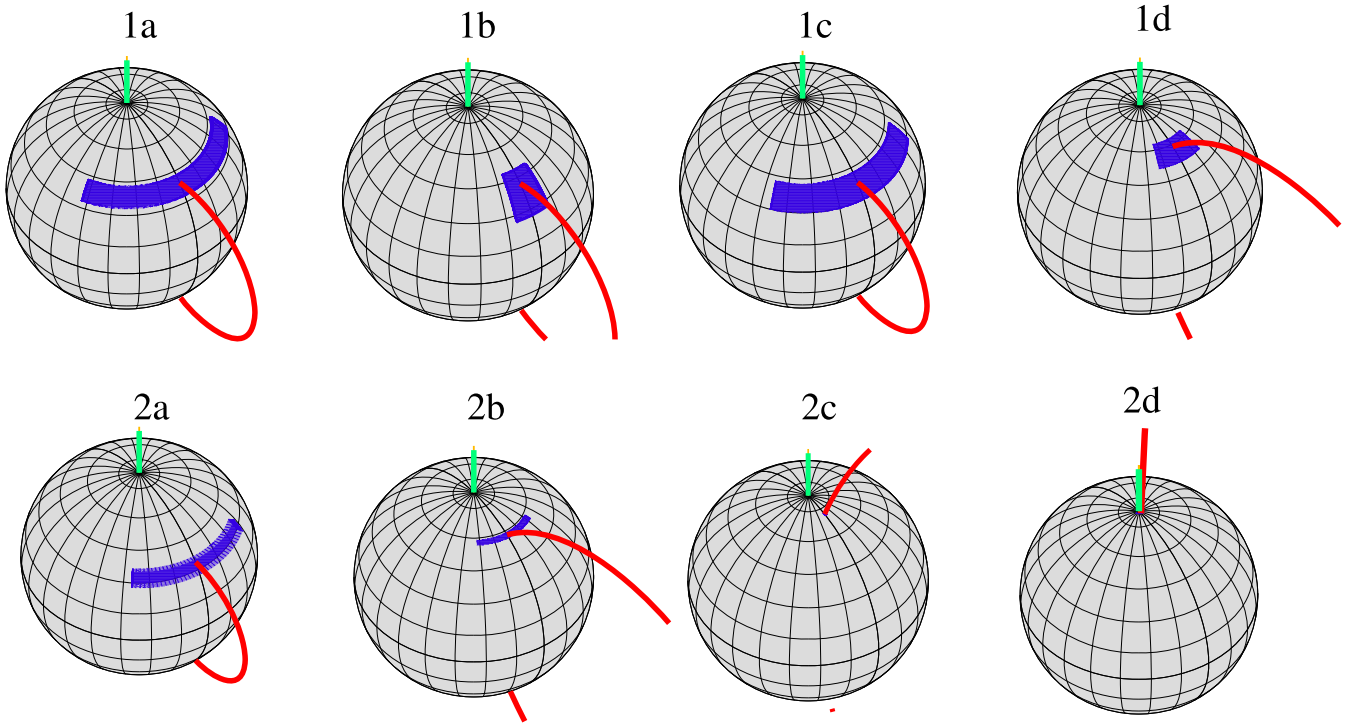

Figure 14. Geometry of the models listed in Table 2, at the WD rotation phase of 0.1, as seen by the observer. The PSR is shown in blue and the WD magnetic field axis, which is coincident with the WD rotation axis in these particular models, in green. The red line indicates the magnetic field line passing through the center of the PSR, which can be thought of as the reference field line for the accretion structure. Notice that the PSR of models 2c and 2d cannot be seen in the figure because their cross sections are very small. In addition, all WDs, which have different masses, have the same size. This does not correctly represent the models, in which the WD radius follows the mass–radius relation. So, this figure is not appropriate to compare the footprint area of the different models.

photoabsorption, models 1a and 1b are only moderately affected by this effect. Most importantly, given the intrinsic uncertainties involved in observational data, it seems very unlikely that the models in each pair could be distinguished, which does not help much in breaking the degeneracy in the set spectrum 1.

The spectra of the models in the set spectrum 2 are very similar, irrespective of the energy range, which means that despite the fact that these models are different, with different accretion geometries, preshock region extinction shapes their spectra in a similar way. In addition, it seems unlikely that, even with high-quality observational data, these models could be unambiguously distinguished. Therefore, even though incorporating this effect makes the fitting more physically appealing, it does not provide a way to solve the degeneracy problem in this set of models.

We finish this discussion about incorporating preshock region extinction in the modeling by emphasizing that it alone most likely cannot break the degeneracy while fitting X-ray continuum spectra. Indeed, from Figure 15, despite the fact that absorption and scattering change the spectrum shapes, we still end up with similar spectra, because the role played by these processes can be similar. For instance, models 1a and 1b have virtually the same spectra, which also happens for models 1 c and 1d, and for all models in the set spectrum 2.

We can conclude by now that adding preshock region extinction as an extra ingredient to a fitting strategy, even though physically required, does not seem enough to solve the degeneracy problem. Therefore, additional constraints are most likely still needed in order to unambiguously distinguish the models.

5.4. Breaking the Degeneracy Using Accurate Distance

Along the PSR, the bremsstrahlung emissivity depends on the electron number density and the temperature. In the optically thin case, which is valid for the X-ray emission of the PSR, the total emission is the integral of the emissivity over the PSR volume. This implies that the "observed" bremsstrahlung flux of a model at a fixed distance depends entirely on its PSR properties (see Equations (C1) and (C2)). This means that, for models having different PSRs, such as the models in the sets spectrum 1 and spectrum 2 (see Figure 13), even though they exhibit virtually identical normalized X-ray spectra, the X-ray fluxes considering the PSR at the same fixed distance could be in principle different. We would like to emphasize that, as shown in Appendix C, the fluxes provided by the CYCLOPS code are in very good agreement with those from XSPEC.

In the context of magnetic CV fitting strategies, by knowing the distance to the investigated system, one can put all analyzed models at the same distance and compare their fluxes. In other words, if an accurate distance estimate for the investigated system exists, e.g., using the accurate parallaxes from the Gaia satellite, the nonnormalized theoretical spectra can be directly compared with the observed one. That said, even though many models can have very similar spectrum shapes, i.e., virtually identical normalized spectra, such spectra could be separated when the distance is incorporated into the fitting scheme.

We shall add to the discussion that, with the accurate distances from the Gaia satellite, deriving X-ray luminosities is possible, which in turn allows us to estimate the accretion rate. for a large fraction of IPs and found that most systems accrete at rates of $\sim 10^{-9}\ M_{\odot}\ \mathrm{yr}^{-1}$, which is consistent with what is expected from CV secular evolution modeling, provided their

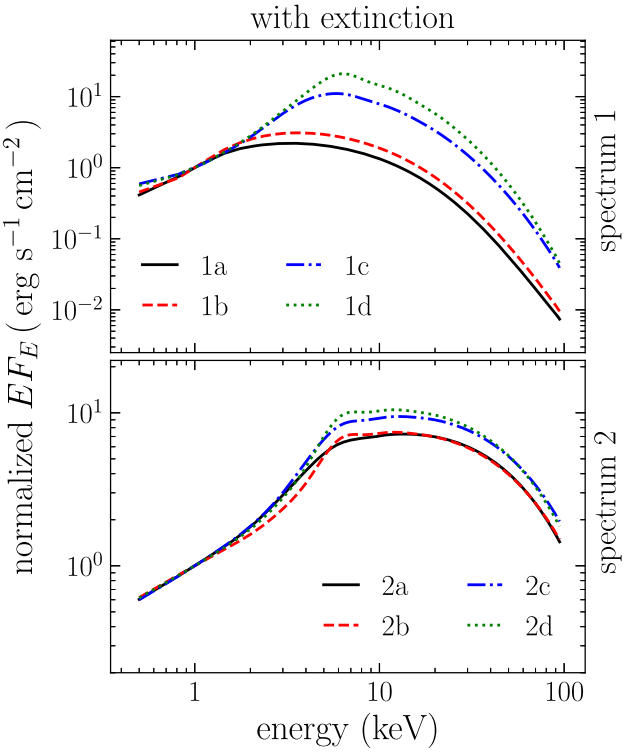

Figure 15. Effect of the preshock region extinction on the X-ray spectra (normalized to their values at 1 keV) of the models in the sets spectrum 1 and spectrum 2, the parameters of which are listed in Table 2. The changes in comparison with Figure 12 are due to photoelectric absorption and Compton scattering of a partially ionized material. The changes in the set spectrum 1 are significant for the pair of models 1c and 1d, in comparison with the pair of models 1a and 1b. However, the changes in all models of the set spectrum 2 are very small. This suggests that even though incorporating only preshock region extinction to a fitting scheme may help, it is unlikely able to solve the degeneracy problem.

orbital periods are usually $\gtrsim$3 hr and their (usually) negligible WD magnetic moments.

We show in Figure 16 the nonnormalized X-ray spectra of the models in the sets spectrum 1 and spectrum 2, assuming a distance of 100 pc for all models, and taking into account or not the preshock region extinction. Regarding the models in the set spectrum 1, irrespective of whether we take into account or not the preshock region extinction, models 1a and 1b as well as models 1c and 1d have virtually identical spectra. This is likely because the accretion rates and the accretion area, and in turn, the specific accretion rate of the models in each of these two sets, are similar (see Table 2). In particular, in models 1a and 1b, $\dot{m}_{\rm b} = 0.20$ and $0.15\,{\rm g\,s^{-1}\,cm^{-2}}$, respectively, while in models 1c and 1d, $\dot{m}_{\rm b} = 1.14$ and $2.47\,{\rm g\,s^{-1}\,cm^{-2}}$, respectively. This implies that models 1c and 1d have denser PSRs than models 1a and 1b. Moreover, the four models have similar volumes, so the different emission levels can be understood only by the different densities because the bremsstrahlung emissivity depends on the squared density.

Comparing now the case in which the preshock region extinction is included with the case in which this effect is ignored, we can clearly see that the hard part of the spectra in this set of models is barely affected. On the other hand, as already stated before, the soft flux is reduced quite a bit, especially for models 1c and 1d, which is likely because these models have denser preshock regions, in comparison with models 1a and 1b.

The models in the set spectrum 2 are more affected when we incorporate not only distance but also preshock region extinction. Starting with the case without preshock region extinction, we can see that, despite the fact that the shape of the spectra of all the models in this set are virtually identical, they can be separated when they are put at the same distance. Unlike the models in the other set, those in this set have very different accretion rates and accretion areas, which implies that they are characterized by different specific accretion rates. Then, their PSRs have different density distributions, although they have similar temperature distributions. This difference in the density distribution combined with very different emitting volumes is likely the reason why they emit in a different way when put at the same distance.

Model 2a is particularly interesting and illustrates another dependence of the luminosity of the PSR. This model has the tallest and sparsest PSR as well as the smallest specific accretion rate in this set of models, and at the same time emits more than models 2c and 2d. This happens because, even though the specific accretion rate might be an important indicator of the X-ray emission intensity, it is not the only parameter affecting the flux. The volume of the emitting region is also relevant and most likely explains why this model emits more than the others, but model 2b.

Regarding the impact of the preshock region extinction on the models of the set spectrum 2, as already stated previously, given the dependence of the photoabsorption cross section on the energy, the soft part of all those models is moderately affected by preshock region absorption. However, unlike for the other set of models, in which the preshock region extinction does not significantly affect the flux in the hard part, the situation for this set is different, the hard flux in models 2b and 2d being strongly reduced due to Compton scattering.

We shall finish this discussion about the distance by emphasizing that by incorporating it alone into the fitting scheme, or even coupled with consistent preshock region modeling, the degeneracy most likely cannot be broken while fitting an X-ray continuum spectrum. We have shown in Figure 16 that, even though we could distinguish the models emitting different flux in some cases, we can still have in the end virtually identical spectra. In the particular set of models investigated here, models 1a and 1b have very similar spectra, as well as models 1 c and 1d, irrespective of whether preshock region extinction is taken into account or not. In addition, when this effect is considered, models 2a and 2b end up with virtually identical spectra.

We can then conclude that including only accurate distance estimates as well as preshock region modeling in a fitting strategy is most likely not enough to undoubtedly solve the degeneracy problem in a general situation. Therefore, similarly to what we have already found, additional constraints other than distance and preshock region extinction are most likely still needed in order to unambiguously distinguish the models. In what follows, we discuss how incorporating X-ray light curves, in different energy ranges, can potentially solve the degeneracy problem, provided consistent preshock region extinction is also included in the modeling.

5.5. Breaking the Degeneracy with X-Ray Light Curves

Given the characteristics of X-ray observations, the same data set can be used to produce spectra and light curves. Hence, the useful constraints provided by light curves do not require

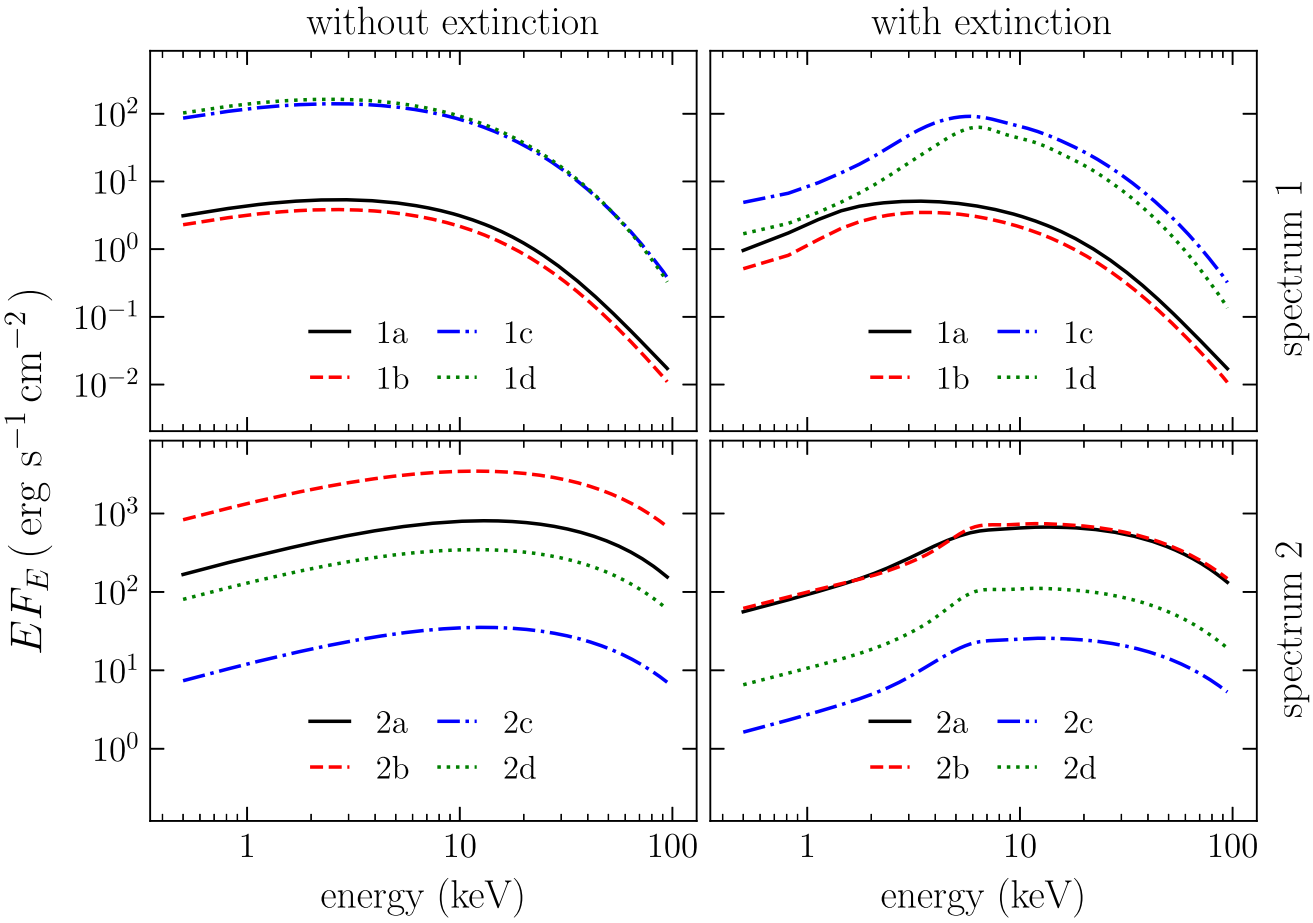

Figure 16. Effect of distance on the X-ray spectra of the models in the set spectrum 1 (top panels) and spectrum 2 (bottom panels). In the spectra, which were obtained using the parameters listed in Table 2 and assuming a distance equal to 100 pc, we considered two cases, namely including preshock region extinction (right panels) and completely ignoring this effect (left panels). We can see that the degeneracy in the set spectrum 1 most likely cannot be broken, as the pair of models 1a and 1b, as well as the pair of models 1c and 1d, still have similar spectra, regardless of whether we incorporate preshock region extinction or not. Regarding the models in the set spectrum 2, the fluxes are different in the case of no preshock region extinction, but when this effect is included, the pair of models 2a and 2b have virtually identical spectra. These examples illustrate that even though incorporating Gaia distances and consistent preshock region modeling to a fitting scheme helps to some extent to break the degeneracy in some cases, they are likely not enough to unambiguously solve the degeneracy problem.

any additional observing time, only additional data reduction. Of course, this is valid if the data set can provide light curves with enough signal-to-noise ratio.

The zero phase of the light curves corresponds to the WD spin phase in which the meridian plane that contains the center of PSR also contains the observer's direction, i.e., the radial vector passing through the center of the PSR and the line of sight define a plane perpendicular to the plane of the sky. In addition, for the sake of simplicity, throughout this section, all light curves have been normalized to their maximum fluxes. Moreover, while discussing the light curves, we adopt the following definition of a pulsed fraction:

$$\mathrm{PF} = \frac{F_{\max} - F_{\min}}{F_{\max}} = 1 - \frac{F_{\min}}{F_{\max}}, \quad (1)$$

where $F_{\max}$ and $F_{\min}$ are the maximum and minimum fluxes of the light curve, respectively.

The modulation of the X-ray flux with the WD rotation in magnetic CVs can have two origins, namely self-eclipse and phase-dependent preshock region extinction. The former might happen for many different geometrical configurations because the PSR can be partially or fully hidden by the WD at several rotation phases, which causes a drop in the observed flux at those phases. Hereafter, we use the term self-eclipse to represent full or partial PSR occultation by the WD. On the other hand, depending on the geometrical properties of the system, the PSR can be partially or fully eclipsed by the preshock region, which in turn may strongly extinguish the flux from the PSR. We start our discussion by focusing on the first effect, i.e., we initially ignore the existence of the preshock region.

5.5.1. Impact of Self-eclipse

From the above-mentioned definition of phase zero adopted in this work, the maximum occultation must occur at phase 0.5. In addition, the shapes and depths of such minima in the light curve are mainly dependent on the system geometrical properties such as the orbital inclination, the PSR colatitude, and the PSR cross section. Finally, the flux must be constant (pulsed fraction $\sim 0\%$) when the PSR can be fully seen by the observer in all rotation phases.

The self-eclipse light curves of the models listed in Table 2 are shown in Figure 17. We present the light curves in five energy intervals, namely 0.5–100 (integrated energy range), 0.5–2, 2–10, 10–20, and 20–40 keV. Models 1a, 1b, and 1c in the set spectrum 1 exhibit strong modulation due to partial self-eclipses (see Figure 14, which illustrates each model

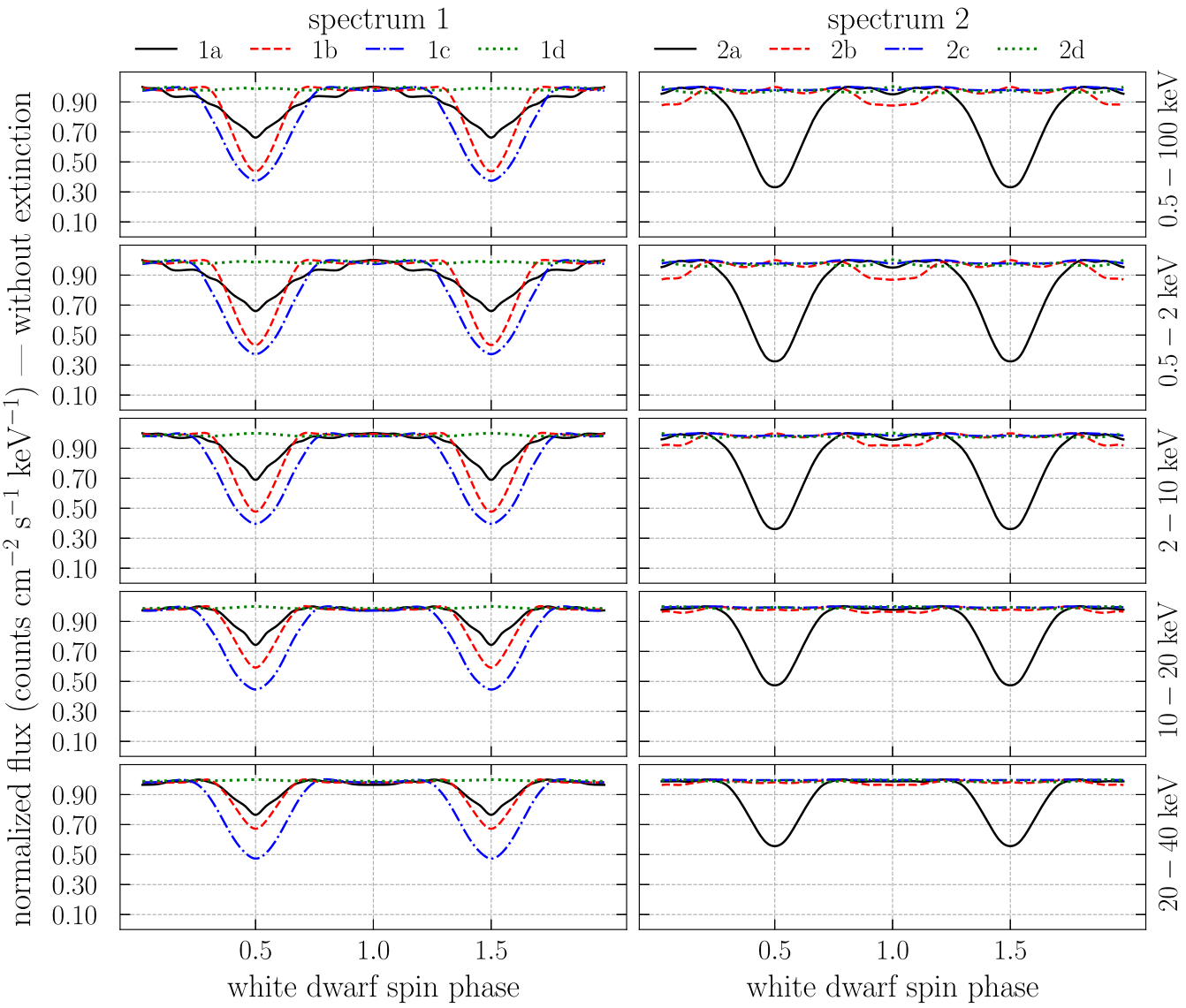

Figure 17. X-ray light curves, normalized to their maximum fluxes, including only the effect of the partial self-eclipse of the PSR by the WD from the two sets of models listed in Table 2, the set spectrum 1 shown in the left column and the set spectrum 2 in the right column, in five energy bands (in keV), namely 0.5–100 (first row), 0.5–2 (second row), 2–10 (third row), 10–20 (fourth row), and 20–40 (fifth row). Despite the fact that no preshock region extinction is considered here, we can see that the light curves of each model in the set spectrum 1 are different from one another, which helps to distinguish them. On the other hand, the light curves of the models in the set spectrum 2 exhibit no modulation, except for model 2a. These different features happen because of the different geometrical characteristics of all eight models, which lead to different modulations due to self-eclipse. Given the absence of modulation in half of the models investigated here, we can then conclude that X-ray light curves, without consistent preshock region modeling, are likely unable to break the degeneracy existing when only the X-ray spectrum is taken into account.

geometry). The pulsed fraction varies from ∼0% (model 1d) to ∼60% (model 1c), which implies that no model in this set presents total self-eclipse. Model 1d is a typical example of systems not undergoing self-eclipse, which have a light curve characterized by a constant flux (pulsed fraction ∼ 0%) irrespective of the rotation phase and energy range.

In the set spectrum 2, only model 2a exhibits partial self-eclipse, while all other models have a pulsed fraction ∼ 0%. This happens because the PSRs of models 2b–2d are located very near the WD rotation pole and the inclination is low enough to avoid occultation of the PSR at any WD spin phase. We would like to draw the reader's attention to the fact that the slight oscillations of the fluxes of models 1a, 1d, and 2b–2d are not real. This happens because the desirable level of precision in the CYCLOPS code is not always readily available, due to the finite spatial resolution of its 3D grid.

5.5.2. Impact of the Preshock Extinction

After discussing how self-eclipse can modulate X-ray light curves, we now investigate the impact of incorporating the preshock region extinction into the X-ray light curves. Before proceeding further, we remind the readers about a couple of important aspects related to the preshock region extinction (see Section 2.2 for more details on how this is treated in CYCLOPS).

First, in the models investigated here, i.e., those described in Table 2, we assume that the material is considered half neutral and half ionized, and the preshock region has a constant density equals to one-fourth of the density at the shock position (see Equation (A14)), which definitely maximizes the effect of the extinction of the preshock region on the observed emission. Second, the preshock region extinction is proportional to the density integrated along the line of sight and can be optically

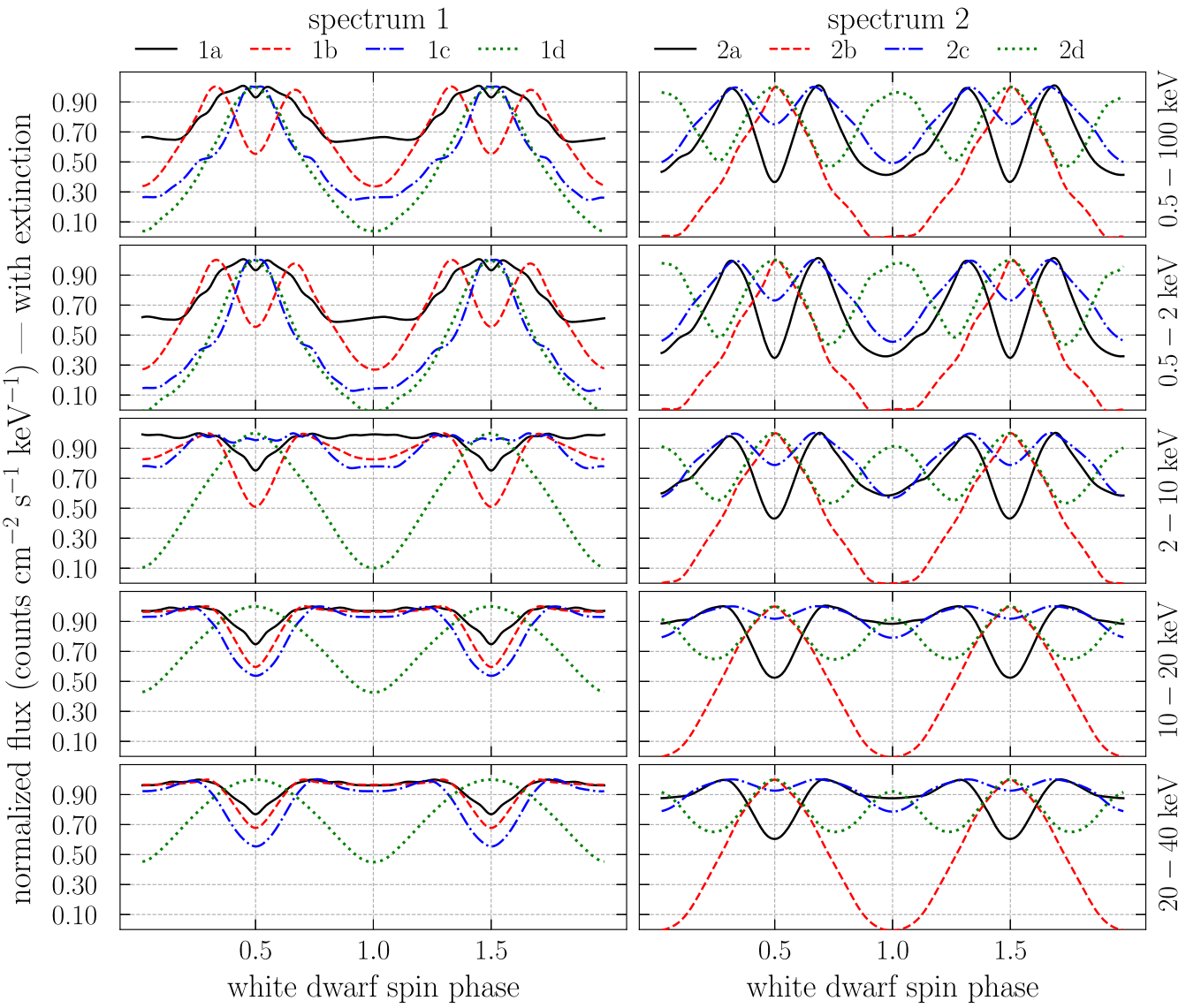

Figure 18. X-ray light curves, normalized to their maximum fluxes, including the partial self-eclipse of the PSR by the WD and the preshock extinction for the two sets of models listed in Table 2, the set spectrum 1 being shown in the left column and spectrum 2 in the right column, in five energy bands (in keV), namely 0.5–100 (first row), 0.5–2 (second row), 2–10 (third row), 10–20 (fourth row), and 20–40 (fifth row). Even though some models have very similar light curves in some energy ranges, clearly, when several energy intervals are considered simultaneously, the light curves of each model investigated here are different from one another. This then allows us to unambiguously distinguish the models and, in turn, solve the degeneracy problem that arises when only the X-ray spectrum is taken into account.

thick for the processes and parameters considered here, unlike the bremsstrahlung emission, which is always optically thin.

We show in Figure 18 how the X-ray light curves shown in Figure 17 change with the inclusion of the preshock region extinction. While the self-eclipse causes minimum fluxes to occur at phase 0.5, the minimum due to the preshock region extinction happens at phase 0.0, except for model 2d. As explained earlier, the self-eclipse minimum is expected at phase 0.5 because at this phase the PSR is just behind the WD, as seen by the observer, which causes the largest possible occultation of the PSR by the WD. On the other hand, the preshock-region-extinction minimum is expected to occur when the preshock region is just in front of the WD at phase 0.0, i.e., between the WD and the observer, because this configuration leads to the largest possible extinction in most cases.

The double-trough feature caused by a combination of self-eclipse and preshock region extinction can be seen in the soft light curves of two models in which partial self-eclipse occurs, namely models 1b and 2a. Interestingly, this feature is very similar to what was found by Hoogerwerf et al. (2006, their Figure 1) in the EX Hya light curve for Mg XI. On the other hand, the self-eclipse minima in the soft light curves of models 1a and 1c cannot be clearly seen in Figure 18. However, in the hard light curves of the four above-mentioned models, we mainly see the minima caused by self-eclipse, as the extinction of their preshock regions is virtually negligible in the hard part. This implies that in these cases there is a change of 0.5 cycles in the light-curve minimum as the energy increases because the minima moved from phase 0.5 to phase 0.0 with the inclusion of the preshock region extinction. Moreover, the light curves of models 1d and 2b are characterized by a single-trough feature, which is caused by the preshock region extinction.

Even though there is no partial self-eclipse in model 2c, because its PSR can in principle be always seen by the observer (see Figure 14), its light curve exhibits a double-trough feature.

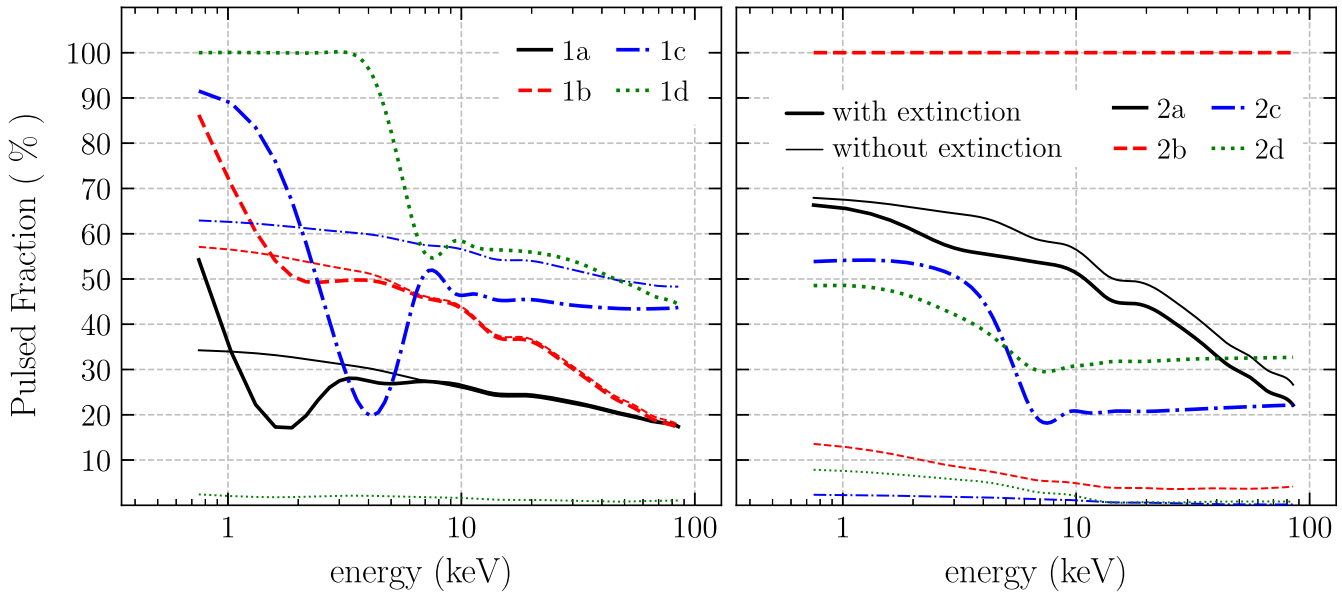

Figure 19. Dependence on energy of the pulsed fraction obtained from the X-ray light curves, for the set of models *s*pectrum 1 (left panel) and spectrum 2 (right panel), which are listed in Table 2, for the case in which the extinction of the preshock region is considered (thick curves) and that in which this effect is ignored (thin curves). Clearly, similarly to what we found while analyzing the X-ray light curves in only five energy intervals, the pulsed fraction in all models varies differently with energy when the entire X-ray range is considered. In addition, when the preshock region is ignored, the pulsed fraction always decreases as the energy increases, because the modulation in the light curves in this case is exclusively due to self-eclipse. However, when this effect is taken into account, irrespective of the energy, the pulsed fraction is always greater than zero, which implies that the X-ray light curves are modulated in the entire X-ray wavelength range. This further strengthens our claim that X-ray light curves, in different energy intervals, are most likely enough to unambiguously solve the degeneracy problem in X-ray spectral modeling, provided the extinction of the preshock region is properly modeled.

This happens because the PSR is seen by the observer behind the preshock region in all phases. That said, the additional trough at phase 0.5 seen in the light curve of model 2c is a direct consequence of the phase-dependent preshock region extinction. In addition, if the extinction is large enough, the self-eclipse modulation can be washed out from the light curves, which is the case for models 1a and 1c. Finally, we shall mention that preshock region extinction can modify the depth of the minima caused by self-eclipse in double-trough light curves, like those of models 1b and 2a.

Regarding the minimum shapes, we first note that the larger the PSR footprint, the larger the geometrical cross section of the entire accretion structure, which also regulates the X-ray flux modulation with the WD rotation phase due to the preshock region extinction. For example, models 1a and 1c have a relatively wider PSR than models 1b and 1d, and consequently, flatter minima. In addition, for model 2a, the minimum exclusively due to the preshock region extinction is flatter than that mainly caused by self-eclipse.

5.5.3. Variation of the Pulsed Fraction with Energy

So far, while discussing the X-ray light curves, we have not considered in detail how they vary with energy. When different energy ranges are taken into account, the flux modulation is expected to be very different in the soft and hard parts. A way of looking at this is by means of how the pulsed fraction varies with energy, considering tens of narrow energy intervals, which is done in Figure 19, for the models in the sets spectrum 1 and spectrum 2. Before proceeding further, we remind the readers that the nonnull pulsed fractions seen in models 1d and 2b–2d for the case in which the preshock region is ignored are not real. This is because the X-ray light curves of these models are not modulated by self-eclipse. Such nonnull pulsed fractions are due to the finite spatial resolution of the 3D grid in the CYCLOPS code.

Starting with the self-eclipse case, we can see in Figures 17 and 19 (thin lines) that there is a decrease in the pulsed fraction as the energy increases. For instance, for model 2a, while the pulsed fraction is ∼65%–70% for energies below 2 keV, it is reduced to ∼30%–40% for energies above 20 keV. This result can seem weird at first glance because self-eclipse is a geometrical effect. However, it is an expected result because the temperature in the PSR is highest at the shock position and drops toward the WD surface (see Figure 13). This implies that the region contributing more to the soft X-ray emission is closer to the WD and therefore can be occulted even in situ ations in which the top of the PSR is visible by the observer. Therefore, for a given geometry in which partial self-eclipse occurs, the lower the energy, the larger the hidden portion of the PSR contributing to that particular energy.

When we incorporate preshock region extinction, the situation can easily become far more complicated, as illustrated in Figures 18 and 19 (thick lines). Even though the above-described dependence on energy is still expected in most models, it is clear from the figures that it can be broken in the presence of preshock region extinction. For instance, model 2b does not exhibit self-eclipse and its extinction is total, i.e., its pulsed fraction is ∼100%, regardless of the energy range, which means that its preshock region is optically thick even at hard energies. In any event, except for this model, we can see in Figure 19 that the pulsed fraction of all other models is clearly larger in the soft part than in the hard part.

Regarding the models in which self-eclipse occurs (i.e., 1a, 1b, 1c, and 2a), the preshock region extinction strongly affects their light curves at energies lower than a few keV. In addition, the pulsed fraction curves of models 1a and 1c exhibit a trough below 10 keV. As the energy increases, after reaching such a

trough, the pulsed fraction increases until it reaches a peak, and finally decreases again. On the other hand, for models 1b and 2a, the pulsed fraction smoothly decreases with energy, without a trough at energies lower than 10 keV.

As previously explained, the preshock region extinction in these models is very large at low energies, which somehow blurs or even erases the self-eclipse modulation. However, when the impact of the extinction becomes much less pronounced (models 1c and 2a) or negligible (models 1a and 1b) at high energies, the self-eclipse modulation dominates, explaining why the pulsed fraction, when extinction is included, is much closer to the pulsed fraction that originated from self-eclipse. For models 1a and 1b, in particular, the extinction of the preshock region is virtually negligible at energies higher than a few keV, which makes their pulsed fractions due to self-eclipse and extinction converge in this energy range. On the other hand, the preshock region extinction of models 1c and 2a is still sufficiently important to affect the light curves in the entire X-ray range, which decreases the pulsed fraction in comparison with the self-eclipse case, irrespective of the energy.

Finally, we note that Figure 18 shows that this energy-dependent behavior of the pulsed fraction is accompanied by a change of 0.5 cycles in the light-curve minimum, for models 1a and 1c. On the other hand, for models 1b and 2a, as the energy increases, the light curves lose the double-trough feature, which is caused by a combination of self-eclipse and preshock region extinction and becomes characterized by a single trough, which is due to self-eclipse.

We now discuss the above results in the context of observations of magnetic CVs. The pulsed fraction in these systems is constant or decreases with energy (e.g., Coti Zelati et al. 2016; Tomsick et al. 2016). The standard explanation for this behavior is the presence (or not) of photoelectric absorption in the mass flow between the stars. Despite not having explored the entire parameter space, the few examples we have shown here are enough to demonstrate that the self-eclipse of the PSR can also produce this behavior. Specifically, the partial self-eclipse of the PSR produces a steady and smooth decrease of the pulsed fraction with energy. More importantly, this effect is intrinsic to a 3D PSR, depending only on the viewing angle of the system, and can be correctly estimated considering the exact same parameters used to calculate the PSR emission itself.

On the other hand, to calculate the preshock extinction, it is necessary to adopt a mass distribution in the preshock region, which is a far less understood subject. This effect also produces a decrease in the pulsed fraction with increasing energy, but with a more complex behavior. In particular, the Chandra and NuSTAR pulsed fraction behavior of EX Hya (Luna et al. 2018) resembles the curves that consider the preshock extinction shown in Figure 19. In summary, both effects (i.e., self-eclipse and preshock region) should be consistently taken into account to correctly understand the amplitude of X-ray light curves of magnetic CVs.

6. Solving the Degeneracy Problem

We have discussed throughout Section 5 the required data and the methods able to help break the degeneracy in the parameter space of magnetic CVs. In particular, we have shown that even though all of them are expected to help solve the degeneracy problem, some of them alone does not seem enough to do the job in a more general situation. For instance, even though incorporating either consistent preshock region modeling or accurate distance estimates helps, several models in the sets spectrum 1 and spectrum 2 still end up with very similar X-ray spectra. In addition, very specific constraints required in any attempt of breaking the degeneracy are not always available, such as the PSR height or the break frequency.

However, X-ray light curves correspond to a very fruitful way out of this problem. We have shown in Figures 18 and 19 that the X-ray light curves of the four models in each set investigated here are substantially different. In particular, their modulations and the location/amplitude of their maxima and minima are substantially different from one another. This implies that X-ray light curves are promising for solving the degeneracy problem. Additionally, we showed in these figures normalized X-ray light curves to better visualization of their shapes. With the Gaia distances, we could disentangle the models even further by comparing their fluxes from the same distance, which is important for models having similar light-curve shapes.

The method we propose that is most likely able to solve the degeneracy problem is based on the utilization of only X-ray data in the fitting scheme. From the same X-ray data, it is not only the continuum spectrum that can be obtained, but also light curves in different energy ranges. More specifically, by incorporating several soft and hard light curves into the fitting scheme, one should be able to disentangle models with similar continuum spectra as well as similar light curves in some energy ranges. In addition to the continuum spectrum and the light curves, the inclusion of emission lines should help even further in solving the degeneracy problem. That said, the information required to break the degeneracy is most likely hidden in the complete X-ray data, which includes the spectrum (continuum plus emission lines) coupled with the light curves in different energy ranges.

However, while comparing Figures 17 and 18, it is quite clear that this method is expected to work only if the preshock region is properly modeled, i.e., if the preshock region extinction is properly taken into account as this region plays a key role in shaping the light curves not only in the soft part but also in the hard part. It is very likely that many models not characterized by self-eclipse could provide X-ray spectra consistent with the observed one. Therefore, those models could not be disentangled as no modulation would show up in their light curves. Another problem is that the signal-to-noise ratio is not always high enough so that light curves could be built from the X-ray data. In those cases, unfortunately, light curves do not help, and additional constraints other than those provided by the X-ray data would be most likely still required (e.g., optical light and polarization curves).

The above-described method we propose here seems the most suitable for a more general approach, provided it is relatively easy to use X-ray light curves in magnetic CV fitting strategies because they could be easily obtained from the same data used to generate the spectrum (i.e., no additional data are required). In addition, none of the other available methods can break the degeneracy in a parameter space composed of more than a few parameters. Therefore, currently, our approach appears the most adequate way out of this issue, given its simplicity and power.

We would like to draw the reader's attention to one important fact. X-ray spectra are mainly related to the physical properties in the PSR, i.e., its temperature and density distributions, which could be combined in many different ways to provide virtually identical spectra. On the other hand, even though the geometrical properties of the PSR are less relevant for determining the emitted X-ray spectrum, they strongly affect the light curves, irrespective of the wavelength. On top of that, the overall magnetic CV emission modeling not only involves the physical and the geometrical properties of the PSR but also the parameters of the system itself, such as the WD mass and the accretion rate.

Therefore, to obtain a correct understanding of a particular magnetic CV, an essential ingredient of any fitting scheme is to properly model the 3D PSR and its impact on the main observables, such as X-ray spectra and light curves. To the best of our knowledge, the CYCLOPS code is the only one currently available that is able to handle this kind of analysis, which makes it a powerful and sophisticated tool to explore magnetic CV emission.

7. Future Developments of the CYCLOPS Code

An updated version of CYCLOPS code (Costa & Rodrigues 2009; Silva et al. 2013) to model X-ray spectra and multiwavelength light curves of magnetic CVs was presented. Despite the power of the CYCLOPS code in fitting magnetic CV observables as well as the many physical processes it takes into account, we would like to stress that some potentially important issues are not included in this version of CYCLOPS, and further developments of the code could address them.

Regarding the PSR model, our current approach assumes one single fluid with equipartition between ions and electrons. Despite this being a reasonable assumption in many cases, there are at least two situations, for massive WDs, in which this assumption is no longer plausible, i.e., in which the electron–ion equipartition timescale is longer than the total cooling timescale. For very low specific accretion rates, the low density within the PSR can easily make energy exchange between electrons and ions inefficient (e.g., Hayashi & Ishida 2014a), which would imply relatively long electron–ion equipartition timescales. In addition, for very strong magnetic fields, the cooling due to cyclotron emission is enhanced, which might cause a strong reduction in the total cooling timescale (e.g., Sarty et al. 2008). Such potentially important cases cannot be properly investigated with the current version of the CYCLOPS code. Therefore, upgrading the code from a one-fluid to a two-fluid approach would make CYCLOPS capable of investigating virtually all types of PSRs, regardless of their parameters.

With respect to the boundary conditions (Equations (A13)–(A16)), our model assumes the standard strong-shock conditions coupled with the flow reaching zero temperature at the WD surface. The latter assumption is most likely not correct and a more realistic approach would be assuming that the flow converges to the photospheric temperature or even to that of a locally heated photosphere (Cropper et al. 1998). This is definitely problematic with respect to the emission line complex originating from regions very close to the WD photosphere, where the temperature is much lower than in the remaining PSR. That said, a way to improve our current model is by relaxing the boundary conditions so that they better match the real physical conditions expected in magnetic CV PSRs.

Regarding the PSR cooling processes (Equation (A17)), we ignore cooling due to Compton scattering and electron conduction as well as cooling from emission lines. Compton scattering is expected to change only very slightly the temperature and density profiles in the PSR (e.g., Suleimanov et al. 2008, their Figure 3). On the other hand, electron conduction may be important at the PSR bottom (e.g., Wu 2000). Finally, cooling due to emission lines is not negligible at the very bottom of the PSR, where the temperature is low ($\lesssim 10^6$ K). For systems with low WD masses, the shock temperature and the postshock gas temperature are low enough that the emission lines can actually contribute to a significant fraction of the total cooling. A fully consistent treatment including all these processes in the hydrodynamic calculation is nontrivial. In addition, the current version of the CYCLOPS code does not handle radiative transfer with either Compton scattering or electron conduction, which makes our choice for the cooling processes consistent within the code. Having said that, future versions of the CYCLOPS code could include these effects, not only in the cooling function but also in the radiative transfer scheme.

Other possible improvements of the CYCLOPS code are related to a better description of the preshock region. For instance, the abundances of the material responsible for the photoelectric absorption should be allowed to vary and, at the same time, be consistent with estimates for the system being studied, which can be obtained from the emission lines. In addition, a more complex upgrade would correspond to estimating the ionization fraction in the accretion structure.

Another ingredient not included in the current version of the CYCLOPS code is the reflection from the WD surface. This process is responsible for the iron Kα line at $\approx$6.4 keV and the Compton hump between $\sim$10 and $\sim$50 keV (George & Fabian 1991). In addition, based on NuSTAR observations, Mukai et al. (2015) and Luna et al. (2018) showed that reflection is an important ingredient to be included in magnetic CV parameter estimation, especially for IPs, which can potentially provide further constraints. A reasonable model for the reflection was developed by Hayashi et al. (2018), who also investigated the influence of the parameters on the iron complex and Compton hump. A model like that could be incorporated in future versions of the CYCLOPS code and complementary analysis be performed (e.g., inferring the influence of the magnetic field vector).

Finally, the thermohydrodynamic differential equations for postshock flows in the CYCLOPS code are not solved simultaneously with the radiative transfer for bremsstrahlung and cyclotron radiations, which is a more realistic approach (e.g., Fischer & Beuermann 2001). Indeed, we first model the PSR based on the 1D approach described in Section A. Then, we perform the 3D phase-dependent and line-of-sight-dependent radiative transfer throughout the PSR as described in Costa & Rodrigues (2009) and Silva et al. (2013).

8. Summary and Conclusions

We have used an updated version of the CYCLOPS code to model X-ray spectra and multiwavelength light curves of magnetic CVs, which includes accurate PSR modeling, by solving the stationary one-dimensional hydrothermodynamic equations describing the accreting plasma, where bremsstrahlung and cyclotron radiative processes play a role in cooling the gas from the shock until the WD surface. We have adopted a

quasi-dipolar geometry, have taken into account the WD gravitational potential and finite size of the magnetosphere radius, and have allowed the magnetic field to decay as the distance from the WD surface increases. While comparing our approach with previous works, we showed that our model agrees reasonably well with previous investigations and showed how the temperature profiles are affected by geometrical and physical parameters. In particular, we discussed a four-dimensional fitting scheme in modeling magnetic CVs, whose parameters are the WD mass, the WD magnetic field, the specific accretion rate, and the threading region radius.

Our main results can be summarized as follows.

(i) We showed that a balance between cyclotron and bremsstrahlung radiative processes always exists in the presence of nonnegligible cyclotron cooling, as expected. In other words, there is always a combination of parameters such that the importance of these emission processes in shaping the PSR profiles are comparable.

(ii) Due to the balance between bremsstrahlung and cyclotron processes, there is always a critical specific accretion rate above which bremsstrahlung radiation governs the cooling and below which cyclotron radiation is the main mechanism driving the cooling. In particular, the greater the WD magnetic field at the PSR bottom, the greater such a critical specific accretion rate, i.e., the influence of cyclotron radiation takes place for a larger range of specific accretion rates.

(iii) Due to the balance between bremsstrahlung and cyclotron processes, the previously found anticorrelation between the shock height and the specific accretion rate is broken in the presence of nonnegligible cyclotron cooling. Additionally, the above-mentioned critical specific accretion rate sets the region in the parameter space where such an anticorrelation is broken.

(iv) We found that, for IPs with extremely low accretion rates (e.g., due to instability in the accretion disk or low state), the cyclotron cooling cannot usually be ignored. This is due to the above-mentioned balance between bremsstrahlung and cyclotron processes, which occurs at low specific accretion rates in systems with weak magnetic fields.

(v) With respect to X-ray spectra, we found that the greater the WD mass and/or the smaller the WD magnetic field and/or the greater the specific accretion rate and/or the greater the threading region radius, the harder the spectrum, as expected. This is intrinsically connected with the role of such parameters in shaping the PSR temperature and density profiles.

(vi) While adopting PSRs with uniform temperature and density distributions, we showed that the CYCLOPS X-ray spectra are in very good agreement with those generated by the XSPEC code, which is a widely used X-ray package to fit X-ray spectra, not only with respect to distance-dependent bremsstrahlung emission but also regarding the impact of the interstellar extinction.

(vii) We showed that there exist thresholds in the parameter space below/above which X-ray spectra become indistinguishable, resulting in a degeneracy among the parameters. In addition, such thresholds strongly depend on the combination of parameters. In other words, due to the balance between bremsstrahlung and cyclotron radiative processes, the interplay between the WD mass, the WD magnetic field, and the specific accretion rate strongly affects the thresholds mentioned above.

(viii) We argued that in our four-dimensional modeling scheme, there is always a degeneracy, regardless of the region of the parameter space one explores, which needs to be addressed in any meaningful fitting scheme.

(ix) We further argued that any attempt to solve the degeneracy problem requires at least more constraints, i.e., having only the X-ray continuum spectrum for a given source is not enough to look for a global minimum used to uniquely estimate the main magnetic CV parameters.

(x) We showed that even though several methods seem to some extent useful to break the degeneracy in the parameter space, some of them alone are most likely not enough to unambiguously solve the degeneracy problem. In particular, despite the fact that incorporating either consistent preshock region modeling or accurate distance estimates may help, most likely in a fitting scheme one would still end up with many different models having very similar X-ray spectra. Moreover, some very specific constraints are not always available, such as the PSR height or the break frequency. However, incorporating light curves into the fitting scheme looks like a promising way out of the degeneracy problem and, based on that, we proposed a method that seems able to solve this problem.

(xi) The method we proposed corresponds to incorporating X-ray light curves in different energy ranges into the fitting scheme, in case there is enough signal-to-noise ratio for that, potentially together with accurate Gaia distance estimates. This is an appealing method because X-ray data already comprise spectra and light curves, and no extra observational effort is required. However, this method is expected to work only if the preshock region is properly modeled as this region plays a key role in shaping X-ray light curves.

(xii) While investigating the energy-dependent pulsed fraction in the X-ray light-curve modeling, we have shown that the partial self-eclipse of the PSR should not be ignored, as it can produce pulsed fractions that smoothly decrease with energy. This implies that the observed decrease of the pulsed fraction with energy in some magnetic CVs is not necessarily due to photoelectric absorption of the preshock region alone and could perhaps be at least partially explained by self-eclipse, depending on the geometrical properties of the system. In addition, this combination of self-eclipse and preshock region absorption could lead to energy-dependent light curves, in the sense that the location or existence of the minima present in the X-ray light curves could depend on the energy.

(xiii) Finally, we showed that the CYCLOPS code, which is a 3D emission modeling code, is a sophisticated tool that can and should be used by the community in future magnetic CV emission modeling, not only with respect to X-ray data but also regarding data in virtually any frequency range, including polarized emission. In addition, to the best of our knowledge, CYCLOPS is the only code available to the community able to consistently model the 3D preshock region, which is an essential ingredient to properly deal with X-ray emission from magnetic CVs.

We would like to thank an anonymous referee for the comments and suggestions that helped to improve this paper. We thank Alfredo N. Iusem for pleasantly explaining many issues associated with the Newton–Raphson root-finding method to solve boundary value problems. We also thank the MCTIC/FINEP (CT-INFRA grant 0112052700) and the Embrace Space Weather Program for the computing facilities at the National Institute for Space Research, Brazil. D.B. was supported by the São Paulo Research Foundation (FAPESP, grant #2017/14289-3) and partially supported by ESO/Gobierno de Chile. C.V.R. thanks grant 303444/2018-5 from CNPq and grant #2017/14289-3 from the São Paulo Research Foundation (FAPESP). M.R.S. acknowledges support from the Millennium Nucleus for Planet Formation (NPF) and Fondecyt (grant 1181404). M.C. thanks grant #2015/25972-0 by FAPESP. G.J.M.L. is a member of the CIC-CONICET (Argentina) and acknowledges support from grant ANPCYT-PICT 0901/2017. A.S.O acknowledges the São Paulo Research Foundation (FAPESP) for financial support under grant #2017/20309-7. S.G.P. acknowledges the support of a Science and Technology Facilities Council (STFC) Ernest Rutherford Fellowship. P.E.S. acknowledges FAPESP for financial support under grant #2017/13551-6. M.Z. acknowledges support from CONICYT PAI (Concurso Nacional de Inserción en la Academia 2017, Folio 79170121) and CONICYT/FONDECYT (Programa de Iniciación, Folio 11170559). I.J.L acknowledges São Paulo Research Foundation (FAPESP) for financial support under grants #2018/05420-1, #2015/24383-7, and #2013/26258-4.

Availability of the CYCLOPS Code

The CYCLOPS code is written in IDL and is freely available by request. In order to obtain a copy of the CYCLOPS code described in this paper, please write to claudia.rodrigues@inpe.br.

Appendix A
Postshock Region

A.1. Basic Assumptions and Geometry

In our modeling, the PSR properties are obtained from the solution of the stationary one-dimensional hydrothermodynamic differential equations describing the accreting plasma. We further assume a dipole-like geometry (i.e., cubic cross-section variation, e.g., Hayashi & Ishida 2014a; Suleimanov et al. 2016) and equipartition between ions and electrons (e.g., Wu et al. 1994; Cropper et al. 1999; Van Box Som et al. 2018). We would like to draw the readers' attention to the fact that, unlike the PSR modeling, a three-dimensional geometry is adopted in the remaining parts of the CYCLOPS code, e.g., the radiative transport and preshock region. Hereafter, we will only discuss the PSR modeling, although in Section 2 we provide more details about the other aspects of the CYCLOPS code.

A stationary model with equipartition is a reasonable assumption provided that the characteristic timescale of energy exchanged between electrons and ions (i.e., the electron–ion equipartition timescale) is much shorter than the cooling timescale. There are two particular situations in which such an assumption does not hold. First, for very low specific accretion rates and massive WDs, the nonequipartition area in the PSR might be well extended ($\gtrsim$80%), which means that the equipartition approach is no longer valid (e.g., Hayashi & Ishida 2014a). This is because of the low density within the PSR, which makes energy exchange between electrons and ions inefficient. However, Hayashi & Ishida (2014b) applied their model considering nonequipartition between ions and electron to the IPs EX Hya and V1223 Sgr and found that even for a relatively small specific accretion rate ($\sim$0.05 g s^{-1} cm^{-2}), equipartition between ions and electrons is quickly achieved close to the shock. Second, for very strong magnetic fields and massive WDs, models assuming nonequipartition predict considerably different shock heights and qualitatively different density and temperature distributions in regions far from the WD surface than models assuming equipartition (e.g., Wu 2000; Saxton et al. 2007; Sarty et al. 2008).

With respect to the cross-section variation, a dipolar geometry is a more realistic approach than standard cylindrical models in which the cross section is assumed to be constant. Indeed, Saxton et al. (2007) showed that the inclusion of a dipolar accretion geometry provides a harder continuum and in turn lowers estimates for WD masses when compared with masses inferred from models excluding this effect. In addition, Hayashi & Ishida (2014a) showed that differences between both approaches become important when the shock height is $\gtrsim$20% of the WD radius (see also Canalle et al. 2005). This is particularly true for accretion columns in IPs, in which the magnetic field is only moderately strong and the shock position might be relatively distant from the WD surface so that changes in the cross section might play a significant role.

In Figure 2 we illustrate the geometrical and physical aspects of our PSR model. In what follows, we describe the differential equations, boundary conditions, and numerical scheme to solve these equations.

A.2. Boundary Value Problem

The steady-state equations presented below are for a plasma that is restricted to flow along the WD magnetic field lines. We assumed here that the plasma is a fully ionized gas respecting the ideal gas law

$$P = n\, k_{\rm B}\, T, \tag{A1}$$

where P is the average pressure, T is the average temperature, $k_{\rm B} = 1.380658 \times 10^{-16}$ erg K^{-1} is the Boltzmann constant, and n is the average number density given by

$$n = \frac{\rho}{\mu\, m_{\rm H}}, \tag{A2}$$

where ρ is the mass density, $\mu = 0.615$ is the mean molecular mass of the fully ionized gas with solar metallicity, and $m_{\rm H} = 1.673525 \times 10^{-24}$ g is the atomic hydrogen mass.

We further assume that the flow is symmetric with respect to the magnetic line passing through the PSR center, variations in the cross section mimic a dipolar geometry (as suggested by Hayashi & Ishida 2014a) and that the hydrothermodynamic quantities are functions of only z (see Figure 2) within the PSR. Under such assumptions, the differential equations related to the mass continuity, momentum conservation, and energy conservation are (e.g., Hayashi & Ishida 2014a):

$$\frac{d}{dz}(S\rho v) = 0, \tag{A3}$$

$$\frac{d}{dz}(\rho v^2 + P) + \frac{\rho v^2}{S}\frac{dS}{dz} + \rho\, g_{\rm WD} = 0, \tag{A4}$$

$$v\frac{dP}{dz} + \gamma P\frac{dv}{dz} + (\gamma - 1)\left(\Lambda - \frac{\rho v^3}{2S}\frac{dS}{dz}\right) = 0, \quad \text{(A5)}$$

where $\gamma = 5/3$ is the adiabatic index, $v(z)$ is the flow velocity, $S(z)$ is the cross section, $\Lambda(z)$ is the cooling function, which is described in Section A.4, and $g_{\rm WD}(z)$ is the WD gravitational field given by

$$g_{\rm WD}(z) = \frac{GM_{\rm WD}}{z^2}, \quad \text{(A6)}$$

where $G = 6.67259 \times 10^{-8}\,{\rm cm^3\,g^{-1}\,s^{-2}}$ is the gravitational constant and $M_{\rm WD}$ is the WD mass.

Note that Equation (A3) contains an integral of the form

$$S(z)\,\rho(z)\,v(z) = S(z)\,\dot{m}(z) = \dot{M}_{\rm WD}, \quad \text{(A7)}$$

where $\dot{M}_{\rm WD}$ is the accretion rate and $\dot{m}(z)$ is the specific accretion rate, i.e., the accretion rate per unit area. Notice that $\dot{M}_{\rm WD}$ is constant but both S and $\dot{m}$ vary throughout the PSR such that their product is constant and equals $\dot{M}_{\rm WD}$. We follow here the formulation by Hayashi & Ishida (2014a) and define the cross section as

$$S(z) = S_{\rm b}\left(\frac{z}{R_{\rm WD}}\right)^n, \quad \text{(A8)}$$

where $S_{\rm b}$ is the accretion area at the bottom of the PSR (see Figure 2), $n = 0$ corresponds to the cylindrical geometry, and $n = 3$ corresponds to the dipolar geometry. The bottom of the PSR corresponds to $z = R_{\rm WD}$ and $S = S_{\rm b}$, the latter coming directly from the adopted magnetic accretion geometry.

The cross-section derivative through the PSR is then given by

$$\frac{dS}{dz} = n\left(\frac{S_{\rm b}}{R_{\rm WD}}\right)\left(\frac{z}{R_{\rm WD}}\right)^{n-1}. \quad \text{(A9)}$$

In order to facilitate the solution of the PSR structure, instead of solving Equations (A3)–(A5) in the variable z, we utilize a different independent variable. The variable z varies from $z = z_{\rm sh} = R_{\rm WD} + H_{\rm sh}$ until $z = R_{\rm WD}$, where $z_{\rm sh}$ is the shock position (i.e., $z_{\rm sh} = R_{\rm WD} + H_{\rm sh}$), $H_{\rm sh}$ is the shock height with respect to the WD surface (see Figure 2), and $R_{\rm WD}$ is the WD radius given by (Nauenberg 1972)

$$\frac{R_{\rm WD}}{\rm cm} = 7.8 \times 10^8 \sqrt{\left(\frac{M_{\rm WD}}{1.44\,M_\odot}\right)^{-2/3} - \left(\frac{M_{\rm WD}}{1.44\,M_\odot}\right)^{2/3}}. \quad \text{(A10)}$$

We define a variable z' such that it goes from 0 to H_s (e.g., Suleimanov et al. 2005), i.e.,

$$z' \;:=\; z_{\rm sh} - z.$$

Equations (A3)–(A5) can be translated into the following two-dimensional system of ordinary differential equations (Hayashi & Ishida 2014a), which has z' as the independent variable:

$$\frac{dP}{dz'} = \frac{(\gamma - 1)\dot{m}\left(\Lambda - \frac{\rho v^3}{2S}\frac{dS}{dz'}\right) + (\dot{m}/v)\gamma P g_{\rm WD}}{\gamma P - \dot{m}v}, \quad \text{(A11)}$$

$$\frac{dv}{dz'} = \frac{g_{\rm WD}}{v} - \frac{1}{\dot{m}}\frac{dP}{dz'}. \quad \text{(A12)}$$

The system variables are the pressure (P) and the velocity (v), and they depend on z', which is the independent variable. The system of ordinary differential equations expressed by Equations (A11) and (A12) is associated with boundary conditions (Appendix A.3), which all together correspond to the boundary value problem defining the PSR.

A.3. Boundary Conditions

The system described by Equations (A11) and (A12) is associated with a boundary value problem, in which the boundary conditions are given at the shock position (i.e., $z' = z_{\rm sh} - z = 0$) and at the WD surface (i.e., $z' = z_{\rm sh} - z = H_{\rm sh}$). At the shock position we assume the Rankine–Hugoniot condition and at the WD surface we impose that the velocity is null.

The pre- and the postshock values of the hydrodynamic variables are related by the Rankine–Hugoniot strong-shock jump conditions. At the shock (just above it), the plasma falls with its freefall velocity ($v_{\rm ff}$). The conditions for the jump are such that, at the shock, the density increases by a factor of 4 and the velocity decreases by a factor of 4, i.e.

$$v_{\rm post} = \frac{v_{\rm pre}}{4} = \frac{v_{\rm ff}}{4} = \frac{1}{4}\sqrt{2GM_{\rm WD}\left(\frac{1}{z_{\rm sh}} - \frac{1}{R_{\rm th}}\right)}, \quad \text{(A13)}$$

$$\rho_{\rm post} = 4\rho_{\rm pre} = 4\frac{\dot{m}}{v_{\rm pre}} = 4\frac{\dot{m}}{v_{\rm ff}} = \frac{\dot{m}}{v_{\rm post}}, \quad \text{(A14)}$$

where $R_{\rm th}$ is the threading region position relative to the WD center (see Figure 1) and corresponds to the point where the magnetic pressure first dominates the gas ram pressure. This position can also be understood as the magnetosphere limit.

As already pointed out by Suleimanov et al. (2016), the assumption of a finite magnetosphere is more accurate than assuming a freefall velocity from infinity. This is rather important for systems with small magnetospheres (a few $R_{\rm WD}$), where matter reaches considerably smaller velocities compared to the case of accretion from infinity (see also Luna et al. 2018).

The boundary conditions at the shock (i.e., $z' = 0$), which are indicated by the subindex "sh," are then given by (e.g., Suleimanov et al. 2005)

$$\begin{cases} v_{\rm sh} = 0.25\sqrt{2GM_{\rm WD}(1/z_{\rm sh} - 1/R_{\rm th})}, \\ \rho_{\rm sh} = \dot{m}_{\rm sh} \,/\, v_{\rm sh}, \\ P_{\rm sh} = 3\,\dot{m}_{\rm sh}\,v_{\rm sh}, \\ T_{\rm sh} = 3\,\mu\,m_{\rm H}\,v_{\rm sh}^2 \,/\, k_B, \end{cases} \quad \text{(A15)}$$

and the condition at the bottom, i.e., at the WD surface is

$$v_{\rm b} = v(z' = H_{\rm sh}) = 0. \quad \text{(A16)}$$

Before describing the numerical scheme to solve the boundary value problem associated with the PSR (Appendix A.5), we discuss the cooling function adopted here.

A.4. Cooling Function

The cooling function (Λ) adopted here includes effects of both bremsstrahlung and the cyclotron processes, i.e.,

$$\Lambda = \Lambda_{\rm brem} + \Lambda_{\rm cyc}. \tag{A17}$$

The optically thin bremsstrahlung cooling is given by (Van Box Som et al. 2018)

$$\frac{\Lambda_{\rm brem}}{\rm erg\ cm^{-3}\ s^{-1}} = 5.01 \times 10^{6}\left(\frac{\rho}{10^{-9}\ \rm g\ cm^{-3}}\right)^{2}\left(\frac{T}{10^{8}\ \rm K}\right)^{1/2}. \tag{A18}$$

To evaluate which of these two radiative processes dominates the cooling, one usually utilizes the cooling ratio ($\epsilon_{\rm sh}$), which is defined as the ratio between the bremsstrahlung and the cyclotron cooling timescales at the shock position, given by (Van Box Som et al. 2018)

$$\epsilon_{\rm sh} = 4.32\left(\frac{B_{\rm sh}}{10\ \rm MG}\right)^{2.85}\left(\frac{\dot{m}_{\rm sh}}{\rm g\ s^{-1}\ cm^{-2}}\right)^{-1.85}\left(\frac{M_{\rm WD}}{0.8\ M_{\odot}}\right)^{2.925} \times \left(\frac{R_{\rm WD}}{7 \times 10^{8}\ \rm cm}\right)^{-2.925}\left(\frac{S_{\rm sh}}{10^{15}\ \rm cm^{2}}\right)^{-0.425}, \tag{A19}$$

where values with the subindex "sh" are quantities at the shock position. Bremsstrahlung dominates in cases where $\epsilon_{\rm sh} < 1$ and cyclotron governs otherwise (see Section 3 for more details).

The optically thick cyclotron cooling is given by (e.g., Canalle et al. 2005; Saxton et al. 2007)

$$\Lambda_{\rm cyc} = \Lambda_{\rm brem}\ \epsilon_{\rm sh}\left(\frac{P}{P_{\rm sh}}\right)^{2}\left(\frac{\rho}{\rho_{\rm sh}}\right)^{-3.85} \times \left(\frac{S}{S_{\rm sh}}\right)^{-0.425}\left(\frac{B}{B_{\rm sh}}\right)^{2.85}, \tag{A20}$$

where the quantities P, ρ, S, and B are not fixed and vary through the PSR, and again quantities with the subindex "sh" are given at the shock position. In particular, the cross-section variation is given by Equation (A8) and the WD magnetic field assumed here is a dipole, which implies that its variation with z is given by

$$B(z) = B_{\rm b}\left(\frac{z}{R_{\rm WD}}\right)^{-3}, \tag{A21}$$

where $B_{\rm b}$ is the magnetic field at the PSR bottom given by

$$B_{\rm b} = \frac{B_{\rm p}}{2}\sqrt{4 - 3\cos^{2}\varrho}, \tag{A22}$$

where $B_{\rm p}$ is the magnetic field intensity at the pole and ϱ is a function of β, $B_{\rm lat}$, and $B_{\rm long}$. We would like to stress that in CYCLOPS code, the parameter is $B_{\rm p}$ (i.e., the magnetic field intensity at the pole), while $B_{\rm b}$ (i.e., the magnetic field intensity at the PSR bottom) is computed accordingly, provided the geometry of the model (i.e., the PSR center colatitude β and the magnetic field axis latitude $B_{\rm lat}$ and longitude $B_{\rm long}$). See Figure 1 for more details on the geometrical aspects of the CYCLOPS code. Finally, for $B_{\rm lat} = 90°$ and $B_{\rm long} = 0°$, i.e., in the case where the magnetic axis coincides with the WD rotation axis, and the PSR and magnetic axis are in the same plane (like in Figure 1), Equation (A22) reduces to an expression consistent with Equation (45) in Canalle et al. (2005).

A.5. Numerical Scheme

The boundary value problem is given by the system of ordinary differential equations defined by Equations (A11) and (A12), coupled with the conditions in Equations (A15) and (A16), where the quantity to be determined is the shock height $H_{\rm sh}$. To solve such a boundary value problem, we iteratively solve the ordinary differential equations. To do so, we guess shock heights and assume the conditions in Equation (A15) as the initial conditions, until we satisfy the condition in Equation (A16), at the WD surface, i.e., null velocity at the PSR bottom.

Because the derivatives of the system tend to be huge as the velocity tends to zero (due to the asymptotic behavior of the solutions while approaching the PSR bottom), we solve the initial value problem with a fourth- to fifth-order Runge–Kutta–Fehlberg integrator with adaptive step-size control in order to reach very small velocities (i.e., with a precision of $\sim 10^{-8}$). Indeed, given the nonsmooth behavior of the system when $v \to 0$, monitoring the local truncation error here is the best way to ensure accuracy by adjusting the step size.

We solve the whole boundary value problem with a simple shooting algorithm based on the Newton–Raphson root-finding method. We start with a trial integration that satisfies the boundary conditions at the shock position, from $v = v_{\rm sh}$ to $v = 10^{-8}$ cm s^{-1}. The final position (i.e., PSR bottom) is then compared with the WD surface position (i.e., $z' = H_{\rm sh}$) and the discrepancy is used to adjust the guessing $H_{\rm sh}$, until the boundary condition at the PSR bottom is eventually satisfied, with a precision of $\sim 10^{-8}$.

Appendix B
Consistency with Previous Works

With the aim of showing that our modeling provides consistent results, we compare in this section our approach with several previous works with similar methods. Starting with our PSR modeling, we show, in the top and middle panels of Figure 20, temperature profiles built with parameters consistent with Cropper et al. (1999, top-left panel), Van Box Som et al. (2018, top-right panel), and Hayashi & Ishida (2014a, middle panels). In the comparisons, a cylindrical model is defined by setting $n = 0$ in Equations (A8) and (A9), while a dipolar model is defined by $n = 3$.

In the comparison with Cropper et al. (1999), we assumed a cylindrical model and set $R_{\rm th} \gg R_{\rm WD}$, $B = 0$, $\dot{m} = 1$ g s^{-1} cm^{-2}, $M_{\rm WD} = 1.0\ M_{\odot}$, and $\mu = 0.615$. In the comparison with Van Box Som et al. (2018), we also assumed a cylindrical model and set $R_{\rm th} \gg R_{\rm WD}$, $B = 10$ MG constant throughout the PSR, $\dot{m} = 1$ g s^{-1} cm^{-2}, $M_{\rm WD} = 0.8\ M_{\odot}$, and $\mu = 0.5$. Finally, in the comparison with Hayashi & Ishida (2014a), we assumed both cylindrical and dipolar models and set $R_{\rm th} \gg R_{\rm WD}$, $B = 0$, $M_{\rm WD} = 0.7\ M_{\odot}$, and $\mu = 0.615$. We then considered two low values for $\dot{m}_{\rm b}$, namely 10^{-4} g s^{-1} cm^{-2} and 10^{-2} g s^{-1} cm^{-2}.

Notice that our profiles are in good agreement with results from the above-mentioned works, and the different shock heights ($\lesssim$10%) are likely due to different cooling prescriptions and numerical methods. For instance, Hayashi & Ishida (2014a) adopted the collisional ionization equilibrium cooling

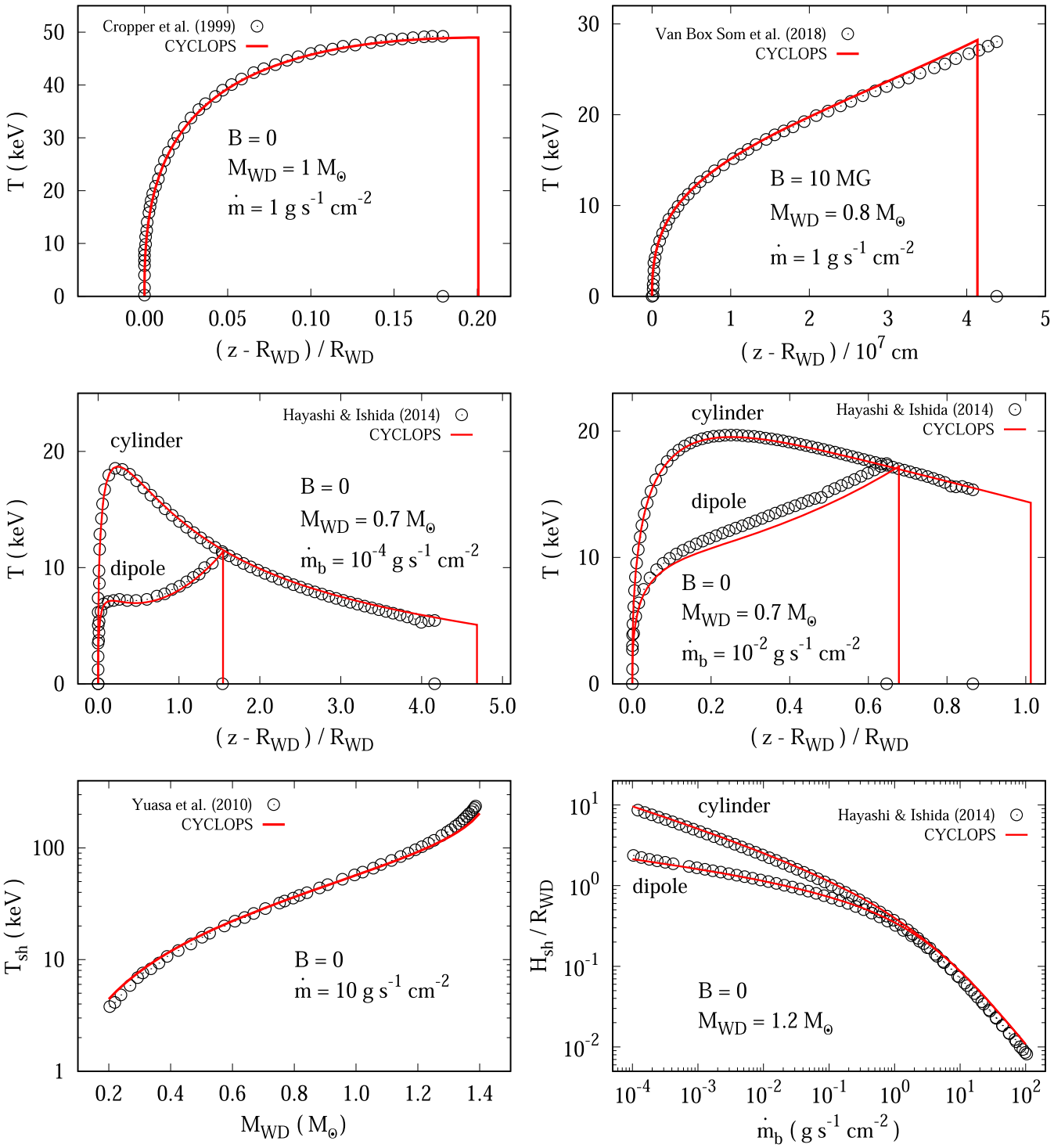

Figure 20. Comparison of different CYCLOPS solutions with previous works. In the top and middle rows, we compare our temperature profiles with Cropper et al. (1999, top-left panel), Van Box Som et al. (2018, top-right panel), and Hayashi & Ishida (2014a, middle-left and -right panels). In the bottom-left panel, we show the temperature at the shock ($T_{\rm sh}$) as a function of the WD mass ($M_{\rm WD}$) and compare with Yuasa et al. (2010). In the bottom-right panel, we provide the shock height in units of the WD radius ($H_{\rm sh}/R_{\rm WD}$) as a function of the specific accretion rate at the WD surface ($\dot{m}_{\rm b}$) and compare with Hayashi & Ishida (2014a). Our profiles are in very good agreement with these previous works, especially the temperature at the shock and the profile shape as a whole. Small differences in the shock height ($\lesssim$10%) are likely due to different cooling prescriptions as well as numerical techniques to solve the system of ordinary differential equations defining the PSR structure.

function calculated with the SPEX package (Schure et al. 2009), in which cooling due to emission lines, which becomes more efficient for temperatures below a few 10^6 K, is included. On the other hand, CYCLOPS does not currently handle line cooling and only bremsstrahlung cooling contributes to the cooling function in the middle panels of Figure 20. This explains why the shock heights in CYCLOPS are slightly greater than those from Hayashi & Ishida (2014a) because the inclusion of line contribution to the cooling function slightly enhances the cooling, resulting in turn in slightly shorter PSRs.

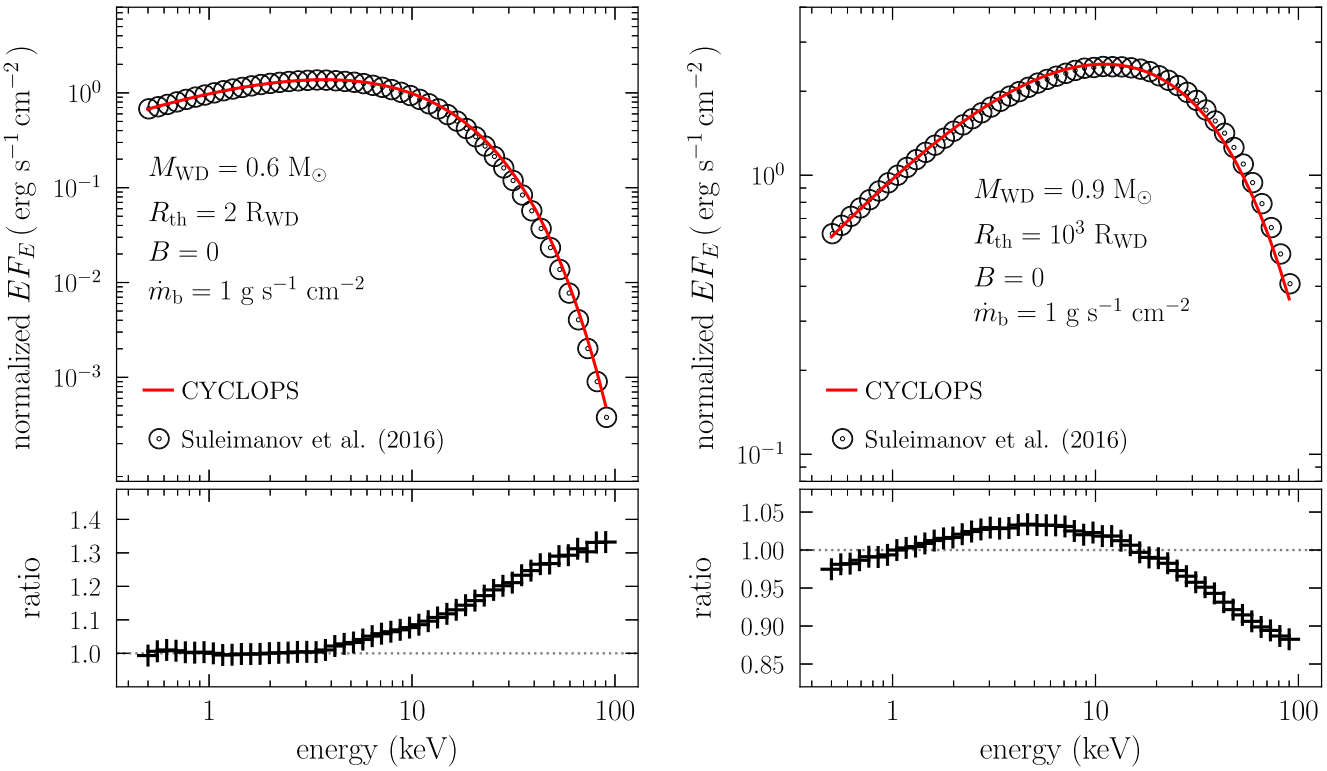

Figure 21. Comparison of two different CYCLOPS X-ray spectra with Suleimanov et al. (2016). In both panels, the spectra are normalized by their values at 1 keV. Our spectra are in very good agreement with Suleimanov et al. (2016) as the differences are very small for energies below ∼20 keV (≲10%) and still small for energies greater than that (≲30%). Such small differences between both works are likely due to slightly different bremsstrahlung prescriptions as well as PSR modeling, which have more impact on the hard part of the spectrum.

Moving forward, we compare our results with Yuasa et al. (2010) and Hayashi & Ishida (2014a) for a set of solutions, in which we assumed parameters consistent with those used by these authors, i.e., $R_{\rm th} \gg R_{\rm WD}$, $B = 0$, and $\mu = 0.615$. In the comparison with Yuasa et al. (2010), we adopted the cylindrical model, fixed $\dot{m} = 10\ {\rm g\ s^{-1}\ cm^{-2}}$, and let $M_{\rm WD}$ vary from 0.2 to 1.4 $M_\odot$. In the comparison with Hayashi & Ishida (2014a), we adopted the cylindrical and dipolar models, fixed $M_{\rm WD} = 1.2\ M_\odot$ and let $\dot{m}_{\rm b}$ vary from 10^{-4} to $10^2\ {\rm g\ s^{-1}\ cm^{-2}}$.

The comparisons are shown in the bottom row of Figure 20, where in the left panel we show the shock temperature $T_{\rm sh}$ against $M_{\rm WD}$ similar to Figure 11 in Yuasa et al. (2010) and in the right panel we show the shock height $H_{\rm sh}$ from the WD surface against $\dot{m}_{\rm b}$ similar to Figure 5 in Hayashi & Ishida (2014a). Notice that we also find a good agreement between our results and theirs. Again, small differences found in these plots are connected with different bremsstrahlung cooling prescriptions and numerical techniques to solve the boundary value problem associated with the PSR structure. In particular, we predict slightly higher (lower) shock temperatures for low-mass (high-mass) WDs, in comparison with Yuasa et al. (2010). Additionally, we predict a slightly larger shock height, especially for high $\dot{m}_{\rm b}$ ($\gtrsim 1\ {\rm g\ s^{-1}\ cm^{-2}}$), in comparison with Hayashi & Ishida (2014a), because line cooling is not included in the CYCLOPS code, which makes the overall cooling less efficient in our case.

The correlation and anticorrelation shown in the bottom row of Figure 20 are interesting and not difficult to understand. With regard to the correlation between the shock temperature ($T_{\rm sh}$) and $M_{\rm WD}$, we notice that $T_{\rm sh}$ strongly depends on the gas velocity at the shock position ($v_{\rm sh}$), which in turn depends on $M_{\rm WD}$, as $v_{\rm sh}$ is a result of the potential energy converted into kinetic energy. In this way, the greater $M_{\rm WD}$, the greater $v_{\rm sh}$, and in turn the greater $T_{\rm sh}$.

Now, the anticorrelation between $H_{\rm sh}$ and $\dot{m}_{\rm b}$ exists for negligible cyclotron cooling cases and is directly related to the bremsstrahlung cooling efficiency in the PSR. Indeed, the greater $\dot{m}_{\rm b}$, the greater the density in the PSR. As the bremsstrahlung cooling rate strongly depends on the density (see Equation (A18)), the greater the density, the greater the cooling rate, and in turn the smaller the PSR height. This implies then that the smaller $\dot{m}_{\rm b}$ is, the greater $H_{\rm sh}$. As discussed in Section 3.2, such an anticorrelation is not always present in the case of nonnegligible cyclotron radiation. In particular, there is a critical specific accretion rate above which there is an anticorrelation and below which there is a correlation. Such a critical specific accretion rate strongly depends on the WD mass and the WD magnetic field.

Now, moving to the X-ray modeling, we show in Figure 21 two X-ray spectra built with parameters consistent with Suleimanov et al. (2016). In both cases, we assumed negligible cyclotron cooling, $\dot{m} = 1\ {\rm g\ s^{-1}\ cm^{-2}}$, and $\mu = 0.615$. In addition, while in the left panel we adopted $R_{\rm th} = 2\ R_{\rm WD}$ and $M_{\rm WD} = 0.6\ M_\odot$, in the right panel we set $R_{\rm th} = 1000\ R_{\rm WD}$ and $M_{\rm WD} = 0.9\ M_\odot$. Notice that our X-ray spectra are in good agreement with the results by Suleimanov et al. (2016). In particular, the spectra agree reasonably well for energies below ∼20 keV because differences are usually smaller than ∼10%. However, for energies greater than that, differences can be a bit higher (∼20%–30%).

This is likely a consequence of the different PSR modeling and bremsstrahlung prescription in both cases (compare our

Section 2 and Appendix A with Section 3 in Suleimanov et al. 2016), which affects the hard part more than the soft one. For instance, the boundary value problem in Suleimanov et al. (2016, see their Equation (21)) is slightly different from ours, which follows Hayashi & Ishida (2014a). In addition, their cooling function is computed by APEC using the AtomDB atomic database, which is different from our approach (see Equations (A17), (A18), and (A20)). Moreover, the calculation of the X-ray spectrum in Suleimanov et al. (2016, see their Equation (29)) is different from what is done in the CYCLOPS code (see Section 2.2 in Silva et al. 2013). Despite the fact that there are differences in the PSR modeling and bremsstrahlung emission in both works, provided that the differences between CYCLOPS and Suleimanov et al. (2016) are small in most portions of the X-ray energy range, we can conclude that both results are consistent with one another.

Appendix C
Comparison with XSPEC

Despite the fact that the PSR modeling in the CYCLOPS code includes the solution of the stationary one-dimensional hydrothermodynamic differential equations describing the accreting plasma as described in Appendix A, it can also handle PSRs with uniform temperature and density distributions, i.e., assuming that the temperature and densities are the same in the entire PSR. This allows us to compare its bremsstrahlung emission modeling with that of the XSPEC code (Arnaud 1996; Dorman & Arnaud 2001). Such a comparison is an essential step in order to demonstrate that the distance-dependent flux in the CYCLOPS code is correctly calculated and the interstellar extinction is properly taken into account.

With the goal of showing that CYCLOPS provides consistent results, throughout this section we compare it with XSPEC for several cases of homogeneous PSRs. Before that, we shall emphasize that CYCLOPS and XSPEC can only be compared in the optically thin regime, because this is the only case currently implemented in the XSPEC code, although for X-rays this assumption is not problematic. The CYCLOPS code, on the other hand, solves the radiative transfer without any approximation in this regard, because it also deals with the usually optically thick cyclotron emission, which happens in optical wavelengths.

In the following comparison, we utilized the model BREMSS (Karzas & Latter 1961) in the XSPEC package. Even though a slightly different bremsstrahlung prescription is adopted in this model with respect to CYCLOPS, it corresponds to the most suitable model to perform such a comparison. Other models such as MEKAL (Mewe et al. 1985, 1986; Kaastra 1992; Liedahl et al. 1995) have bremsstrahlung recipes more similar to that of CYCLOPS and could in principle be better for our purpose. However, these models include emission lines of many elements, which would not result in meaningful comparisons, provided that currently there is no prescription for line emission in the CYCLOPS code. While discussing interstellar extinction, we adopted the PHABS model in XSPEC, which calculates the required photoelectric absorption cross sections. In addition, as our primary goal is to show that not only the shape but also the flux of the CYCLOPS spectra is consistent with those of XSPEC, we assume in all cases a distance of 100 pc. Moreover, we fix the electronic density to $10^{16}\,\mathrm{cm}^{-3}$ and focus here on the impact of the PSR temperature in shaping the X-ray spectra as well as in determining their X-ray flux.

In order to properly compare CYCLOPS with XSPEC, we need first to make sure that the emitting source is the same in both cases. For that we utilize the normalization factor for the BREMSS model adopted in XSPEC given by

$$\mathrm{Norm} = \frac{3.02 \times 10^{-15}}{4\,\pi\,D^2} \int n_e\, n_I\, dV, \tag{C1}$$

where D is the distance to the source, n_e and n_I are the electron and ion number densities, and V is the volume. For our purposes here, we assume that $n_e = n_I$, which implies that Equation (C1) can be expressed as

$$\mathrm{Norm} \simeq 2.524 \times 10^{-53} \left(\frac{D}{\mathrm{cm}}\right)^{-2} \times \left(\frac{n_e}{\mathrm{cm}^{-3}}\right)^2 \left(\frac{S_\mathrm{b}}{\mathrm{cm}^2}\right) \left(\frac{H_\mathrm{sh}}{\mathrm{cm}}\right), \tag{C2}$$

where S_b is the accretion area at the PSR bottom and H_sh is the PSR height (see Figure 2). This normalization factor directly implies that the "observed" bremsstrahlung flux coming out of a model depends not only on the distance but also on the PSR properties.

In order to compare the spectra from CYCLOPS and XSPEC, we first calculated the PSR of a generic model with the formalism described in Appendix A. That procedure provides a nonhomogeneous PSR, i.e., the temperature and density vary along the PSR. However, as mentioned before in this section, we assume here that the temperature and density are constant throughout the PSR. To achieve that, we kept the PSR geometrical properties and simply forced the temperature and density to be constant. Thus, having the PSR cross section and height from this generic model and fixing the distance, we can compute the normalization factor with Equation (C2). This normalization factor is then used to make sure we have the same emitting region properties, i.e., volume and distance, in CYCLOPS and XSPEC, guaranteeing in turn that we can compare the fluxes. Finally, the XSPEC spectra have been calculated using the standard procedure for the BREMSS model.

We show in Figure 22 the X-ray spectra from CYCLOPS and XSPEC, considering four different temperatures, namely 1, 10, 50, and 100 keV. We can clearly see from the figure that the differences between the BREMSS model in XSPEC and CYCLOPS are usually smaller than 10%, irrespective of the energy and assumed temperature. Given that CYCLOPS and XSPEC are different codes, it is not surprising that their spectra are not identical. However, they are very similar, being consistent with one another. We can then conclude that the CYCLOPS code provides X-ray spectra in excellent agreement with the widely used XSPEC code. Moreover, the precision of the analytical expressions of the free–free Gaunt factor adopted in XSPEC and CYCLOPS is around 10% (see, e.g., Mewe et al. 1986). So, the differences between the two codes are within the precision we have in the bremsstrahlung emissivities.

We would like to draw the reader's attention to the fact that CYCLOPS X-ray flux is independent of the assumed spatial resolution in the plane of the sky, which implies that the area of each and every cell in the 3D grid is correctly calculated. This is because such a resolution defines the size of each cell in the grid and therefore its solid angle, which also depends on the distance. In addition, to obtain the flux in each line of sight that represents the PSR, the emerging intensity from the cell closer

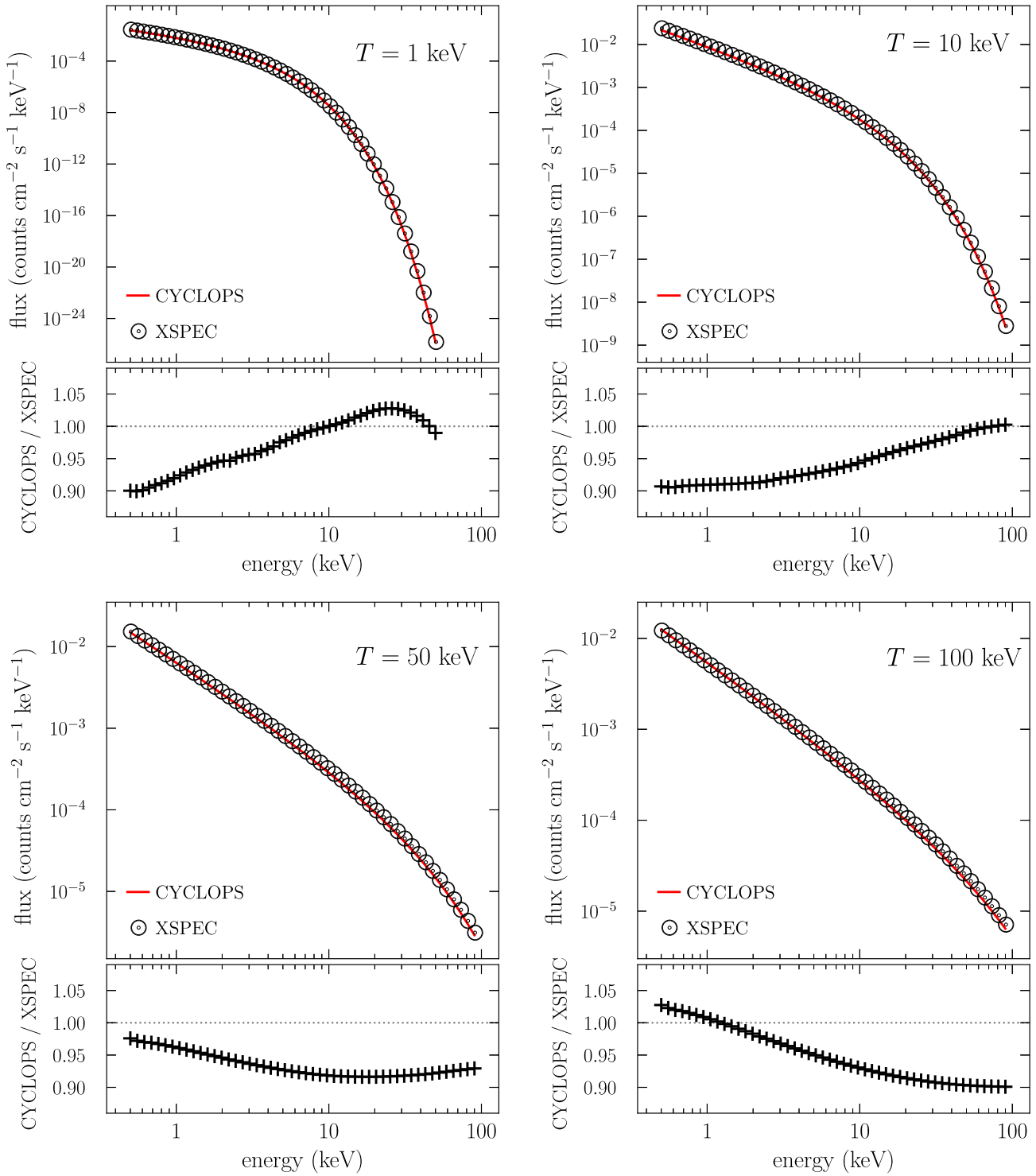

Figure 22. Comparison between X-ray spectra from CYCLOPS and XSPEC (model BREMSS) for four different values of the temperature, namely 1 (top-left panel), 10 (top-right panel), 50 (bottom-left panel), and 100 keV (bottom-right panel). In all models, the electronic density is 10^{16} cm^{-3} and the distance is 100 pc. Clearly, the spectra from CYCLOPS are in excellent agreement with those from XSPEC, provided that the differences are usually smaller than 10%, irrespective of the energy. We can then conclude that the CYCLOPS code properly deals with nonnormalized spectra, i.e., it can take into account the distance while fitting an object.

to the observer, which results from the radiative transport along the entire line of sight, is multiplied by the cell area (in steradians). Therefore, because the flux is not affected by variations in the spatial resolution, we can conclude that the angular areas of the cells are correctly calculated in CYCLOPS.

The last aspect of X-ray modeling we compare with XSPEC is the interstellar extinction. We show in Figure 23 how the photoelectric absorption affects the spectra by assuming a temperature of 20 keV and three different values of hydrogen column density $N_{\rm H}$, namely 10^{20}, 10^{21}, and 10^{22} cm^{-2}. We can clearly see that the impact of absorption in both codes is rather similar, irrespective of $N_{\rm H}$. On the other hand, for energies below 1 keV, models in the CYCLOPS code are clearly much more absorbed in comparison with what the combination of

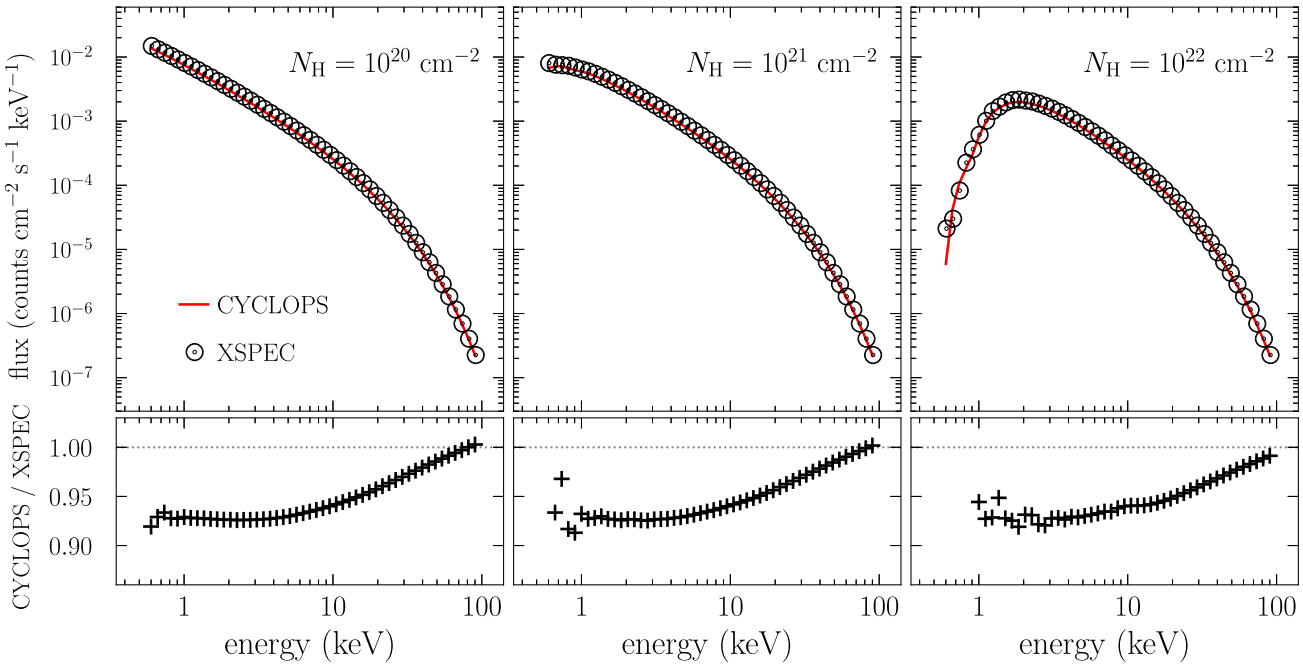

Figure 23. Comparison between X-ray spectra from CYCLOPS and XSPEC (combination of models BREMSS and PHABS), taking into account photoelectric absorption, for three different values of the hydrogen column density N_H, namely 10^{20} (left panel), 10^{21} (middle panel), and 10^{22} cm^{-2} (right panel). In all models, the temperature is 20 keV, the electronic density is 10^{16} cm^{-3}, and the distance is 100 pc. As expected, absorption is negligible for low values of N_H, but becomes relevant for $N_H > 10^{20}$ cm^{-2}, at energies below a few keV. Most importantly, the impact of absorption in CYCLOPS and XSPEC is very similar (differences are smaller than 10%), except for energies below 1 keV. We can then conclude that both codes are consistent with one another.

PHABS and BREMSS models provides. In any event, like in the previous case in which we varied the temperature, the differences between both codes are smaller than 10%, except for the above-mentioned discrepancy at the softer part. Therefore, as before, we can conclude that spectra in CYCLOPS and XSPEC are in excellent agreement.

ORCID iDs

Diogo Belloni https://orcid.org/0000-0003-1535-0866
Claudia V. Rodrigues https://orcid.org/0000-0002-9459-043X
Matthias R. Schreiber https://orcid.org/0000-0003-3903-8009
Manuel Castro https://orcid.org/0000-0003-2162-8393
Joaquim E. R. Costa https://orcid.org/0000-0002-0703-4735
Isabel J. Lima https://orcid.org/0000-0001-6013-1772
Gerardo J. M. Luna https://orcid.org/0000-0002-2647-4373
Murilo Martins https://orcid.org/0000-0003-3014-7989
Alexandre S. Oliveira https://orcid.org/0000-0001-6422-9486
Steven G. Parsons https://orcid.org/0000-0002-2695-2654
Karleyne M. G. Silva https://orcid.org/0000-0003-1949-4621
Paulo E. Stecchini https://orcid.org/0000-0002-2503-2434
Teresa J. Stuchi https://orcid.org/0000-0003-0700-6205
Monica Zorotovic https://orcid.org/0000-0002-4526-0469

References

Aizu, K. 1973, PThPh, 49, 1184
Arnaud, K. A. 1996, in ASP Conf. Ser. 101, Astronomical Data Analysis Software and Systems V, ed. G. H. Jacoby & J. Barnes (San Francisco, CA: ASP), 17
Balucinska-Church, M., & McCammon, D. 1992, ApJ, 400, 699
Belloni, D., Schreiber, M. R., Salaris, M., Maccarone, T. J., & Zorotovic, M. 2021, MNRAS, 505, L74
Bernardini, F., de Martino, D., Mukai, K., et al. 2017, MNRAS, 470, 4815
Canalle, J. B. G., Saxton, C. J., Wu, K., Cropper, M., & Ramsay, G. 2005, A&A, 440, 185
Cardelli, J. A., Clayton, G. C., & Mathis, J. S. 1989, ApJ, 345, 245
Costa, J. E. R., & Rodrigues, C. V. 2009, MNRAS, 398, 240
Coti Zelati, F., Rea, N., Campana, S., et al. 2016, MNRAS, 456, 1913
Cropper, M. 1990, SSRv, 54, 195
Cropper, M., Ramsay, G., & Wu, K. 1998, MNRAS, 293, 222
Cropper, M., Wu, K., Ramsay, G., & Kocabiyik, A. 1999, MNRAS, 306, 684
Dorman, B., & Arnaud, K. A. 2001, in ASP Conf. Ser. 238, Astronomical Data Analysis Software and Systems X, ed. F. R. Harnden, Jr., F. A. Primini, & H. E. Payne (San Francisco, CA: ASP), 415
Ezuka, H., & Ishida, M. 1999, ApJS, 120, 277
Ferrario, L., de Martino, D., & Gänsicke, B. T. 2015, SSRv, 191, 111
Ferrario, L., Wickramasinghe, D., & Kawka, A. 2020, AdSpR, 66, 1025
Ferrario, L., Wickramasinghe, D. T., & Tuohy, I. R. 1989, ApJ, 341, 327
Fischer, A., & Beuermann, K. 2001, A&A, 373, 211
Fujimoto, R., & Ishida, M. 1997, ApJ, 474, 774
George, I. M., & Fabian, A. C. 1991, MNRAS, 249, 352
Gronenschild, E. H. B. M., & Mewe, R. 1978, A&AS, 32, 283
Hameury, J. M., King, A. R., Lasota, J. P., & Ritter, H. 1987, ApJ, 316, 275
Hayashi, T., & Ishida, M. 2014a, MNRAS, 438, 2267
Hayashi, T., & Ishida, M. 2014b, MNRAS, 441, 3718
Hayashi, T., Ishida, M., Terada, Y., Bamba, A., & Shionome, T. 2011, PASJ, 63, S739
Hayashi, T., Kitaguchi, T., & Ishida, M. 2018, MNRAS, 474, 1810
Hellier, C. 2001, Cataclysmic Variable Stars (Berlin: Springer)
Hoogerwerf, R., Brickhouse, N. S., & Mauche, C. W. 2006, ApJL, 643, L45
Hōshi, R. 1973, PThPh, 49, 776
Imamura, J. N., Durisen, R. H., Lamb, D. Q., & Weast, G. J. 1987, ApJ, 313, 298
Ishida, M., & Ezuk, H. 1999, in ASP Conf. Ser. 157, Annapolis Workshop on Magnetic Cataclysmic Variables, ed. C. Hellier & K. Mukai (San Francisco, CA: ASP), 333
Kaastra, J. 1992, An X-ray Spectral Code for Optically Thin Plasmas, Internal SRON-Leiden Report v2.0
Karzas, W. J., & Latter, R. 1961, ApJS, 6, 167
Kashyap, V., & Drake, J. J. 2000, BASI, 28, 475
Liedahl, D. A., Osterheld, A. L., & Goldstein, W. H. 1995, ApJL, 438, L115

Luna, G. J. M., Mukai, K., Orio, M., & Zemko, P. 2018, ApJL, 852, L8
Luna, G. J. M., Raymond, J. C., Brickhouse, N. S., et al. 2010, ApJ, 711, 1333
Luna, G. J. M., Raymond, J. C., Brickhouse, N. S., Mauche, C. W., & Suleimanov, V. 2015, A&A, 578, A15
Meggitt, S. M. A., & Wickramasinghe, D. T. 1982, MNRAS, 198, 71
Mewe, R., Gronenschild, E. H. B. M., & van den Oord, G. H. J. 1985, A&AS, 62, 197
Mewe, R., Lemen, J. R., & van den Oord, G. H. J. 1986, A&AS, 65, 511
Mhlahlo, N., Buckley, D. A. H., Dhillon, V. S., et al. 2007, MNRAS, 378, 211
Mukai, K. 2017, PASP, 129, 062001
Mukai, K., Rana, V., Bernardini, F., & de Martino, D. 2015, ApJL, 807, L30
Nauenberg, M. 1972, ApJ, 175, 417
Norton, A. J., Butters, O. W., Parker, T. L., & Wynn, G. A. 2008, ApJ, 672, 524
Oliveira, A. S., Rodrigues, C. V., Palhares, M. S., et al. 2019, MNRAS, 489, 4032
Pacholczyk, A. G., & Swihart, T. L. 1975, ApJ, 196, 125
Patterson, J. 1994, PASP, 106, 209
Ramsay, G. 2000, MNRAS, 314, 403
Ramsay, G., & Cropper, M. 2004, MNRAS, 347, 497
Revnivtsev, M., Burenin, R., Bikmaev, I., et al. 2010, A&A, 513, A63
Revnivtsev, M., Churazov, E., Postnov, K., & Tsygankov, S. 2009, A&A, 507, 1211
Revnivtsev, M., Potter, S., Kniazev, A., et al. 2011, MNRAS, 411, 1317
Rybicki, G. B., & Lightman, A. P. 1986, Radiative Processes in Astrophysics (New York: Wiley-VCH)
Sarty, G. E., Saxton, C. J., & Wu, K. 2008, Ap&SS, 317, 239
Saxton, C. J., Wu, K., Canalle, J. B. G., Cropper, M., & Ramsay, G. 2007, MNRAS, 379, 779
Schreiber, M. R., Belloni, D., Gänsicke, B. T., Parsons, S. G., & Zorotovic, M. 2021, NatAs, 5, 648
Schure, K. M., Kosenko, D., Kaastra, J. S., Keppens, R., & Vink, J. 2009, A&A, 508, 751
Semena, A. N., Revnivtsev, M. G., Buckley, D. A. H., et al. 2014, MNRAS, 442, 1123
Shaw, A. W., Heinke, C. O., Mukai, K., et al. 2020, MNRAS, 498, 3457
Silva, K. M. G., Rodrigues, C. V., Costa, J. E. R., et al. 2013, MNRAS, 432, 1587
Suleimanov, V., Doroshenko, V., Ducci, L., Zhukov, G. V., & Werner, K. 2016, A&A, 591, A35
Suleimanov, V., Poutanen, J., Falanga, M., & Werner, K. 2008, A&A, 491, 525
Suleimanov, V., Revnivtsev, M., & Ritter, H. 2005, A&A, 435, 191
Suleimanov, V. F., Doroshenko, V., & Werner, K. 2019, MNRAS, 482, 3622
Tomsick, J. A., Rahoui, F., Krivonos, R., et al. 2016, MNRAS, 460, 513
Van Box Som, L., Falize, É., Bonnet-Bidaud, J.-M., et al. 2018, MNRAS, 473, 3158
Warner, B. 1995, Cataclysmic Variable Stars (Cambridge: Cambridge Univ. Press)
Wickramasinghe, D. T., & Ferrario, L. 2000, PASP, 112, 873
Wu, K. 2000, SSRv, 93, 611
Wu, K., Chanmugam, G., & Shaviv, G. 1994, ApJ, 426, 664
Yuasa, T., Nakazawa, K., Makishima, K., et al. 2010, A&A, 520, A25
Zhu, H., Tian, W., Li, A., & Zhang, M. 2017, MNRAS, 471, 3494